The University of Strathclyde

Investigation of the interaction of high current relativistic electron beams with electromagnetic fields

Terence Garvey

Department of Natural Philosophy

Thesis submitted for the degree of Ph.D.

1983

Acknowledgements

Warm thanks are due to my supervisor, Dr Alan Phelps, whose counsel and constant encouragement during the period of this research were of immeasurable value. I should also like to thank the technical staff of the Department of Natural Philosophy for their assistance, in particular, the efforts of Kenny McKenzie and Jim Richmond are acknowledged.

I am indebted to Kate for converting the original manuscript into a legible document and to Mrs Sue Hill for typing the latter. The financial assistance of the SERC is gratefully acknowledged.

Finally, I should like to express my appreciation to a number of parties who have, in their own way, contributed to my writing this thesis.

ABSTRACT

The results obtained in the investigation of high current relativistic electron beams produced by explosive electron emission from the flare cathode plasma of a high voltage, cold-cathode, field-emission diode are reported. In addition, the production of high power ($\sim$100kW) microwave radiation through the interaction of such beams with the natural modes of a resonant cavity is reported.

A Marx bank generator was used to excite a hollow cylindrical cathode stalk producing diode currents of the order of 1kA. A fraction ($\lesssim$ 5%) of the diode current was transmitted through a thin anode mesh to produce a relativistic electron beam drifting in a low pressure (2 μ torr) region. Diode voltage pulse widths of typically one microsecond were observed with anode-cathode (A-K) gap spacings of 7.5mm to 50mm being employed.

The thermal expansion of the cathode plasma resulted in a time dependent diode impedance and measurements of this impedance for varying initial A-K gap settings illustrated a space-charge limited current-voltage characteristic.

A quasi-static magnetic field, produced by a pulsed solenoidal coil, was used to magnetise the vacuum drift space in which the beam propagated. The interaction of the relativistic beam with the magnetic field produced high power microwave radiation at X-band and Q-band frequencies. The

most prominent feature of this interaction was the existence of sharp "resonant" field values where radiation ocurred. This self-excited radiation is thought to be due to an interaction between the Doppler-shifted electron cyclotron frequency (ECF) of the electron beam and the natural modes of oscillation of the cavity in which the beam drifts. Observation of radiation at Q-band frequencies would indicate that harmonics of the ECF are also present, albeit at weaker intensities.

The magnitude of the collected electron beam current was observed to be dependent upon the strength of the applied magnetic field in which the beam drifted.

CONTENTS

SYMBOLS LIST

The following is a list of the most frequently used symbols in the text.

Symbols not included in the list but which appear in the text are defined where they appear.

V_m	Marx voltage
Z_D	REB diode impedance
V_D	REB diode voltage
R_s	Marx bank series resistance
g	initial anode-cathode gap spacing
I_B	electron beam current
I_D	REB diode current
K	generalised perveance, wave number
β	ratio of electron speed to the speed of light
γ	electron energy in units of rest energy
ν	Budker parameter
B_z	axial value of external magnetic field
B_o	value of external magnetic field at coil centre
l	magnetic field coil length
d	magnetic field coil diameter, damping factor
τ	time interval between switching of Marx bank and magnetic field circuit
ω_{ce}	electron cyclotron frequency
P_μ	peak microwave power
I_C	Rogowski coil current
L	Rogowski coil inductance, magnetic field circuit inductance
N	Rogowski coil number of turns, number of turns on magnetic field coil
C	magnetic field circuit capacitance, passive integrator capacitance
I	current in magnetic field coil

PHYSICAL CONSTANTS

K	Boltzman constant
E_o	electron rest energy
r_o	classical electron radius
c	speed of light
e	charge on the electron
$\hbar$	Planck's constant divided by 2π
η	charge to mass ratio of the electron
ε_o	permittivity of free space
μ_o	permeability of free space
m_o	rest mass of the electron

Notation

Q band $\equiv$ Ka-band (26.5 - 40) GHz

1 perv = 1 $A/V^{3/2}$

CHAPTER ONE GENERAL INTRODUCTION

1.1 Introduction

Charged particle beams, and particularly electron beams, have been studied and utilised by physicists for a great number of years. Electron beam devices have been constructed with an enormous array of differing requirements varying from the relatively small triode valves for radio equipment, operating at a few hundred volts, to the enormous linear and orbital accelerators of high energy nuclear particle physics with their ultra-relativistic ($\sim$GeV) electron energies. However, a feature which is common to most electron gun devices such as those in klystrons, cathode ray oscilloscopes or electron microscopes, in which the current is normally produced in a c.w. mode from thermonic emission, is the characteristically low current values of these devices.

The limitations on total beam power imposed by space charge forces for uniform flow in these instruments can be understood from the analysis carried out by Lawson in which he classifies various non-neutral stream configurations in terms of a number of dimensionless parameters appropriate to the stream.[1,2,3] Lawson extended the idea of beam perveance to relativistic, non-neutral beams, with no external acceleration in the direction of motion, to discuss radial beam stability for different conditions of current and voltage. He found the equation of motion of an electron at the edge of a cylindrical beam of

initially uniform cross section to be,

$$r_b \frac{d^2 r_b}{dz^2} = \frac{2\nu}{\beta^2 \gamma} (1 - \beta^2 - f) \qquad (1.1)$$

where,

r_b = beam radius

γ is the ratio of electron energy to rest mass energy,

f is the fractional neutralisation of the stream,

z is the axial distance along the stream,

β is the ratio of electron axial speed to the speed of light,

and ν, the so-called Budker parameter[4], is the product of the line density of the particle stream and the classical electron radius.

Harrison[5] has given solutions to equation (1.1) for small values of z from which Lawson concludes that the beam will be stable against space-charge spreading if

$$K = \left[\frac{2\nu}{\beta^2 \gamma}\right] \times (1 - \beta^2 - f) < 1 \qquad (1.2)$$

and K is defined as the beam's generalised perveance.

In the last two decades research carried out on an international scale has resulted in rapid development in advances in high-voltage, pulse power technology and subsequently to the development of new types of electron accelerators with multi-kiloamp beam currents which overcome post acceleration problems by virtue of their large self-fields.[6]

1.2 High-Current Relativistic Electron Beams (REBs)

These relativistic electron beam (REB) accelerators generally consist of a capacitively stored energy source which feeds a high voltage pulse (0.3 MeV - 1 MeV) through a fast closing switch to an evacuated diode region. The large diode currents which result in these devices (typically 1kA-100kA depending on the diode characteristic impedance) are obtained from acceleration of electrons from a plasma which is formed over the cold cathode surface due to the rise of the voltage pulse. This phenomena of "explosive electron emission" has been investigated by Mesyats [7] and experimental evidence of the cathode plasma has been observed by a number of workers [8,9]. Early REB accelerators were capable of producing pulsed electron beams with total power in the range (10^{10} - 10^{12}) watts [10]. The pulse duration of such devices was limited by the thermal expansion of the cathode plasma which resulted in electrical shorting of the diode. For sufficiently large electron beam currents an anode plasma contributed to this anode-cathode (A-K) gap closure.

Early experiments with REBs were concerned with the beam propagation and focussing. The earliest measurements were made with side-on open shutter photography to measure the self-luminosity of a beam injected through a thin anode foil, into a drift region with varying background pressures [10]. The transport behaviour of the beams in the differing neutral gas pressures were explained in terms of the analysis carried out by Lawson before the advent of these devices. Ionisation

effects of the electron beam on the gas and the subsequent changes in the self-fields of the propagating beam permitted an explanation of the degree of electron beam focussing. Link added a "magnetic neutralisation" term to Lawson's analysis to successfully explain the experimental results. The origin of the magnetic neutralisation is due to the fast changing magnetic field at the beam front creating an electric field which inductively drives a counter streaming current to that of the beam so reducing the overall azimuthal magnetic compression. The existence of this neutralising current also explained the large currents observed in REB experiments with complete charge neutrality.

Alfvén, while discussing the motion of cosmic rays, realised that charge neutral electron streams would be limited to current values corresponding to ν/γ being of the order of unity, resulting in the familiar current limit [11,12].

$$I_A = \frac{(ec)}{(r_o)} \beta\gamma = 17 \beta\gamma \text{ kA} \qquad (1.3),$$

where r_o is the classical electron radius = 2.82×10^{-15} m, and I_A is known as the Alfvén-Lawson limiting current.

The condition $\nu/\gamma \simeq 1$ implies that the self-magnetic field of the beam is such as to make the Larmor radius of an electron at the beam edge equal to half the beam radius resulting in a magnetic deflection of the electron through 180°, thus resulting in back streaming of the electron motion.

Magnetic neutralisation produces a reduction of these self azimuthal fields resulting in more efficient propagation of electron beams.

The considerations which first led Alfvén, and subsequently Lawson, to place an upper limit to the amount of current which may be carried by a charge neutral beam were based on paraxial streaming motion of the individual electrons, with the transverse velocities being small in comparison with the longitudinal velocities.

Bennett [13], who had earlier considered the problem of constricted current flow, made a similar assumption when he assigned a two dimensional temperature to counter streaming electron and ion currents with the streaming velocities large in comparison with the radial speeds. He arrived at his now well known result for the "Bennett Pinch" current, I_B, given by,

$$I_B^2 = \frac{8\pi N}{\mu_o}(T_e + T_i)K \qquad (1.4),$$

where N = electron line density,

T_e = the electron temperature,

T_i = the ion temperature,

K = Boltzmann's constant,

and μ_o = the permeability of free space.

It is clear from equation (1.4) that the maximum permissible current is, in fact, limited by the energy content transverse to the direction of propagation. Lawson [2], in fact, has shown that Bennett's relation is intimately related to his generalised perveance equation for $f = 1$ and $\beta \simeq 1$. With those values for f and β Lawson's equation becomes,

$$-\frac{K}{2} = \frac{\nu}{\gamma} \simeq \frac{(\beta_t^2)}{\beta^2} \qquad (1.5),$$

where β_t is the ratio of transverse velocity to speed of light. It is seen, therefore, that if the transverse energy per particle (KT_e) is large in comparison with the drift kinetic energy ($\simeq \gamma m_o \beta^2 c^2$)current limitation in the sense of Alfven-Lawson can be overcome, i.e.,

$$\frac{\nu}{\gamma} \simeq {}^{I}/_{I_A} > 1 \qquad (1.6)$$

The transition of ${}^{\nu}/_{\gamma}$ from being less than unity to being greater than unity is regarded as a transition from the beam being a paraxial stream to being a drifting plasma.

Many intense beam experiments have consisted of hollow, annular beams initiated from hollow cylindrical cathodes. This arrangement may also be beneficial in overcoming the effects of current limitation due to the self magnetic fields of the beam. Self consistent equilibria for such beam profiles have been discussed by Davidson [14], Hammer and Rostoker [15], Auer [16] and Benford [17]. Their radial beam distributions are calculated from self consistent, time independent Vlasov and Maxwell equations. In essence, the electron beams are deflected by the self-fields into the hollow section of the beam which is free of magnetic forces and, therefore, the beam electrons spend most of their time outside the large azimuthal field region resulting in a decrease in beam deflection. The analysis resulting from these self consistent

models once again shows that the transverse energy of a beam particle must exceed its streaming energy for hollow beam currents to exceed the Alfvén-Lawson limitation.

A second, equivalent, condition which arises from this analysis is that the beam radius, r_b, must exceed the collisionless skin depth, δ, of the non-neutral plasma, i.e.,

$$r_b / \delta > 1 \qquad (1.7),$$

where,

$$\delta = \frac{c}{\omega_{pe}} \qquad (1.8)$$

and ω_{pe} is the electron beam plasma frequency in the beam frame of reference.

The unique characteristics of these REB diodes has resulted in their application in a wide range of topics such as intense X-ray production, pumping of gas and chemical lasers, return current plasma heating, inertial confinement fusion, collective ion acceleration, field reversing electron rings for "minimum-B" geometries in magnetic confinement fusion and, most pertinent to this work, the production of pulsed bursts of high power microwave radiation.[18]

1.3 Electron Beam-Magnetic Field Interactions

It is now well known that the interaction of electron beams with magnetic fields can result in the production of electromagnetic radiation. This radiation production is not limited to low current devices such as low power microwave

valves, in which beam-wave instabilities produce microwave amplification, or the dipole-type radiation which is emitted by electrons in synchrotron devices.

Interactions between intense REBs and various magnetic field configurations have resulted in powerful bursts of microwave radiation. The first measurements of powerful microwave emission from an intense beam drifting through a magnetic field were reported by Nation [19]. In his experiment the drift tube was loaded with a slow wave structure and induced Cerenkov radiation of 10MW was observed. Later, though, experiments were carried out in which the slow wave structure was removed and, instead, a periodically rippled magnetic field, followed by a region of uniform axial magnetic field was employed to interact with the beam and, again, microwave emission was observed.[20]

Further experiments on similar apparatus carried out by Nation and Carmel led these authors to conclude that the radiation production mechanism was a resonant interaction between a cyclotron wave on the beam and a natural waveguide mode.[21] The free energy for microwave production was obtained from the transverse velocities of the orbiting electrons and the importance of the rippled field structure was that this was responsible for converting streaming electron energy into motion perpendicular to the external magnetic field.

It should be noted that the aforementioned experiments

on periodically rippled magnetic fields are not related to Undulators or Free Electron Lasers. These devices employ a "twister" or "wiggler" magnetic field which is a sinusoidal or helically varying magnetic field transverse to the direction of electron propagation. The periodically rippled fields of Friedman and Herndon are axially directed fields with a small sinusoidal variation in axial field strength along the direction of beam propagation, although, of course, there will be some transverse field variations. The configuration of Friedman and Herndon is more closely related to the Ubitron [22].

After the work of Nation and Carmel a host of publications reported multi-megawatt microwave emission from beam-field interactions. Friedman and Herndon investigated the importance of the transverse energy content of the beam in producing microwave power enhanced over that which would be expected from a single particle process.[23] In a separate paper they reported total r.f. radiated power greater than 30MW equivalent to 1% efficiency of conversion of beam kinetic energy to radiation energy, in a device whose frequency and bandwidth were tunable over a wide range and whose emitted power at harmonics of the fundamental frequency was comparable to the magnitude at the fundamental.[24]

Later Granatstein et al built a novel device which produced 50MW at X-band with narrow linewidth.[25] Their drift region arrangement allowed them to prove conclusively

that radiation production was due to the transverse energy of the electrons, $\gtrsim$ 80% of total energy in this case, and they carried out a theoretical analysis to support their contention that the radiation production mechanism was a resonant process between the positive energy TE_{01} waveguide mode and the fast beam cyclotron wave mode. In later work the same authors achieved amplification of an externally applied microwave signal injected into the beam drift tube.[26] In addition, again using a rippled field structure, they produced radiation at a wider range of frequencies including strong submillimetre radiation although there were doubts about whether these frequencies (0.39 mm - 0.54 mm) originated from higher harmonics of the same instability as the other frequencies.[27] An experiment with a multi-megawatt electron beam diode carried the emitted X-band power from these devices into the gigawatt power regime.[28]

1.4.1 The Electron Cyclotron Maser Instability

The microwave emission from the interaction of electron currents with magnetic fields can be understood in terms of the work of the astrophysicist, Twiss [29]. In an effort to explain radio emission from solar disturbances Twiss considered the possibility that a group of electrons gyrating in a magnetic field might exhibit negative absorption, or amplification, of electromagnetic radiation. He arrived at the conclusion that two conditions had to be simultaneously satisfied in order to produce negative absorption. The two conditions which have to be satisfied over some common energy interval are:

$$\text{(i)} \quad \frac{\partial F}{\partial E} > 0 \qquad (1.9a),$$

and

$$\text{(ii)} \quad \frac{\partial Q}{\partial E} < 0 \qquad (1.9b),$$

where F(E) is the distribution of the electron ensemble over energy, and Q(E) is the effective probability for stimulated emission.

The first of the above conditions is the requirement for a sufficient excess in the population of higher classical magnetic moments, while the second condition implies an energy dependent level separation with the level separations becoming smaller as we go up in energy

level. The first of these conditions is satisfied in the experiments discussed earlier where perturbations in the magnetic field structure were responsible for producing beams of electrons whose transverse energy was sharply peaked about some non-zero value.

The second condition is also found to be true in these devices by considering the theoretical analysis carried out by Schneider [30] and independently by Gaponov [31]. Schneider considered the problem of electrons orbiting perpendicularly to, but not along, a magnetic field from a quantum mechanical viewpoint. By solving the relativistic Schrodinger equation, neglecting spin, he found the kinetic energy levels to be,

$$W_i = m_o c^2 \left[\left[1 + 2 \left(i + \tfrac{1}{2} \right) \frac{\hbar \omega_o}{m_o c^2} \right]^{\frac{1}{2}} - 1 \right] \quad (1.10)$$

where, i = the i^{th} energy level,

W_i = the kinetic energy of an electron appropriate to the level i,

$\hbar$ = Planck's constant divided by 2π ,

m_o is the rest mass of the electron,

and ω_o is the non-relativistic cyclotron angular frequency, where,

$$\omega_o = \frac{eB}{m_o} \quad (1.11),$$

and B is the magnitude of the magnetic field about which the electrons orbit.

Transitions between the two states i + 1 and i will result in an emission at a frequency $\omega_{i+1,i}$ where,

$$\omega_{i+1,i} = \omega_o \left[1 - \frac{i\hbar\omega_o}{m_o c^2} \right] \qquad (1.12)$$

and second order terms in $\left[\frac{\hbar \omega_o}{m_o c^2} \right]$ have been neglected, i.e., we are only considering $i\hbar \omega_o \ll m_o c^2$, a condition which prevailed in all the experiments mentioned above. It is clear from equation (1.12) that the energy level spacings are energy dependent with the spacing decreasing as we go up in energy, as is required by (1.9b). If condition (1.9a) is met by arranging a system of electrons with a population inversion existing between levels i and i + 1, then photons incident on the ensemble with angular frequency $\omega_{i+1,i}$ will induce a greater number of downward transitions, i + 1 → i, than upward transitions, i → i + 1. It is the unequal energy dependent level spacing which favours stimulated emission over absorption so leading to an increase in the number of photons, that is, to amplification of the incident radiation.

It is easily shown that equation (1.10) is equivalent to,[32]

$$W_i = \frac{2(i + \frac{1}{2})\hbar\omega_o}{\gamma(i) + 1} \qquad (1.13)$$

where $\gamma(i) = \frac{W_i + m_o c^2}{m_o c^2}$ is the usual relativistic factor. Equation (1.13) serves to elucidate the decreased energy level spacing with increasing energy. In the limit of very large i the spacing between energy levels becomes $\omega_{ce} = \omega_o / \gamma$.

These energy levels, the so called Landau levels, act as a multi-level maser with very high quantum numbers and a large transition probability. Flyagin (33) notes that such an arrangement will operate as a high efficiency maser if many levels contribute to the emission process.

1.4.2 The Physical Mechanism of the ECM

A qualatative picture of the cyclotron maser gain mechanism can be obtained by considering an ensemble of electrons orbiting a magnetic field with an initial random variation in phase. Normally, electrons orbiting magnetic fields will emit magneto-bremsstrahlung radiation as a result of their centrifugal acceleration (34). For the cyclotron maser process one must look for a phase bunching mechanism that will result in a more powerful collective emission from the electron ensemble. If an azimuthal sinusoidally varying electric field interacts with the oscillating electrons, for example the TE_{01} field of a cylindrical cavity, then electrons absorbing energy from the TE_{01} wave, as a result of their phase relative to the wave,

will become more massive and, due to the relativistic dependence on electron gyrofrequency, will start to slip back in phase. Meanwhile those electrons whose phase initially favours a deceleration by the electric field will lose energy and move forward in phase. If the angular frequency, ω, of the electric field is initially chosen to be slightly larger than the relativistic electron cyclotron frequency, or its harmonics, (i.e., $\omega \gtrsim n\,\omega_{ce}$, $n = 1,2,3$ .....) then the electrons which lose energy to the field will move closer to the resonant frequency of the cavity, and therefore will lose energy to the wave for a longer time than the electrons with unfavourable phases will absorb energy from the wave. The initially random phase bunch will then become azimuthally bunched such as to favour emission over absorption of radiation. It is clear from this phenomenological description of the ECM instability that its gain mechanism depends on the relativistic dependence of the electron gyrofrequency for its existence.

Electron tubes designed to operate on the principle of the electron cyclotron maser instability offer the possibility of obtaining powerful coherent emission at wavelengths at which other devices fail to function efficiently. Far infra-red and optical radiation may be generated powerfully by molecular

lasers, however, in these quantum electronic devices each lasing transition may contribute only one photon to the amplifying signal and therefore at longer wavelengths, millimetre and sub-millimetre, the energy per photon of a molecular laser decreases.

Classical microwave valves, on the other hand, contribute many photons per electron with little change in energy, however, the operating wavelength of these microwave valves is determined by some resonant structure, for example, a wire helix in the case of the travelling wave tube. As the internal dimensions of these devices has to be of the order of the operating wavelength problems associated with heat dissipation and electrical breakdown limit their power handling capability at wavelengths below the centimetre region.(35) In addition problems regarding mechanical tolerances make these devices difficult to manufacture as the operating frequency is increased.

ECM devices operate at a wavelength which is characteristic of the particle, the electron gyrofrequency, and is therefore determined by the value of an applied magnetic field and not by any resonant structure. Therefore large operating volumes can be employed leading to high power compatibility with low wavelength operation. These large interaction volumes are analagous to the active gain volume of a laser cavity. In addition,

each electron in an ECM tube may contribute many photons to the amplifying signal. The ECM, then, may be considered as a hybrid device and it is natural that it should operate efficiently at wavelengths intermediate to the operating wavelengths of lasers and of classical microwave devices.

As a result of the considerations above, ECMs have been found to emit the highest peak and average powers achieved over wavelengths ranging from 0.92mm to 4mm.[36] They have exceeded competing devices by orders of magnitude in power production at millimetre and sub-millimetre levels.

The earliest experimental work involving fast wave cyclotron resonance interactions were with output power levels no greater than 1 watt. Chow and Pantell[37] observed radiation at frequencies between 2.5 GHz and 4.00 GHz from a 1kV, 3 μA beam interacting with a magnetic field. They explained their results in terms of an axial bunching mechanism rather than the azimuthal mechanism mentioned above.[38,39] In 1964 I.B. Bott at the Royal Radar Establishment, Malvern reported radiation between 2.2mm and 0.95mm from a 50 mA, 10kV beam traversing a converging pulsed magnetic field of peak value 10T. Bott's radiation propagated through a glass tube with silvered walls and was coupled out through a quartz end window. He postulated that this arrangement would act as a cavity and mentioned that the

radiation mechanism might be an incoherent interaction at the cyclotron frequency in the resonant cavity.

The first experiment which unequivocally determined the existence of cyclotron maser action was reported in 1964. Hirshfield and Wachtel (40) propagated 5 keV electrons through first, a static transverse magnetic "corkscrew" field, and then a spatially converging magnetic field. Their corkscrew field arrangement functioned in the same way as the rippled field structures of the high power experiments, channeling energy into transverse motion at the expense of longitudinal motion. They demonstrated a negative absorption profile which matched the profile of the existing theory with amplification occuring at a B field 1% higher than the rest mass frequency corresponding to the 1% change in γ appropriate to 5 keV electrons. These authors, in fact, coined the expression, "the Electron Cyclotron Maser".

1.4.3 The Gyrotron

In contrast to the ECM devices which employ high current pulsed power technology, producing high peak powers at low efficiencies, researchers in the Soviet Union have developed an ECM which operates at more modest power levels but with much higher efficiencies [41,42]. This device, known as a Gyrotron, employs a more conventional thermionic cathode to facilitate c.w. and long pulse operation. Gyrotrons are now being developed in several countries for fusion plasma heating experiments [43,44].

The electron beam in a Gyrotron is produced from a triode magnetron injection gun (MIG) with two electrodes to control the beam. The MIG produces an annular electron beam and then accelerates it through a rising magnetic field. This gun produces a beam with a high ratio ($\simeq 1.5:1$) of transverse electron velocity to longitudinal electron velocity. The spread in the value of this parameter is a limiting factor in the device efficiency and excessive space-charge is known to be deleterious to the value of the velocity spread [45].

Theoretical studies of Gyrotrons include, for example, suggestions for enhancement of efficiency (notably through magnetic field contouring) [46] and the prediction of two separate modes of instability saturation, dependent upon the value of the initial transverse electron energy [36]. Gyrotron development has been extensively reviewed in a number of publications [33,47,48]. In contrast to these c.w. and long pulse devices this thesis will be concerned with pulsed high current investigations.

2.1 Introduction

This chapter describes the basic components which were used in producing the relativistic electron beam, and subsequently the microwave radiation, with the exception of the circuitry for the external pulsed magnetic field which will be discussed in the following chapter. The main parts of the project for which the author was responsible were the interaction of the e-beam with the magnetic field and consequently the design of the relevant parts of the apparatus were the the author's contribution. The author was responsible for designing and using the magnetic field coil and circuitry (chapter 3). The author's work involved the design, construction, calibration and use of the diagnostics (chapter 4). The pulse generating system and the diode were not originated by the author but since the author used the REB generator in his research this apparatus is briefly described in this chapter.

2.2.1 The Marx Bank

As the large beam currents required for high power microwave emission cannot be produced from small thermionic cathodes a field emission diode was used which was supplied by a conventional Marx generator. Such generators consist of a number, n, of capacitors charged in parallel to a voltage, V, and then rapidly switched into a series configuration to give the output magnitude of the Marx bank equal to nV[49].

In the generator used in the experiments with which this thesis is concerned there were ten 0.5μF capacitors of working voltage 100kV but which were never charged above 35kV each, resulting in a maximum stored electrical energy of 3kJ. The Marx capacitors were charged using a (0-60) kV EHT unit with a "variac" control allowing the charging voltage to be set

to within 3% of that desired. A schematic diagram of the Marx bank is shown in Fig. (2.1). The interconnecting resistors were of a copper-sulphate solution in distilled water and were contained in plastic tubes. These "water-resistors" were chosen for their large thermal capacity and their absence of electrical breakdown problems. The capacitors were charged utilising the "plus-minus" charging scheme leaving all condenser casings grounded and reducing insulation problems with the charging leads. In addition this arrangement requires the use of only half as many spark gaps as there are capacitors. Connections from the EHT unit to the Marx condensers were closed safely and remotely using pneumatic controls. Typical charging times for the Marx bank were approximately thirty seconds.

2.2.2 Marx Triggering

Switching the Marx into the cold-cathode could be achieved in any of the three following fashions:-

(i) use of a pneumatic piston to electrically short the trigger electrode and one electrode of the main gap on the Marx bank, Fig. (2.1);

(ii) simultaneously depressurising all the Marx bank spark gaps;

(iii) an electrical trigger pulse to the main gap of the Marx bank.

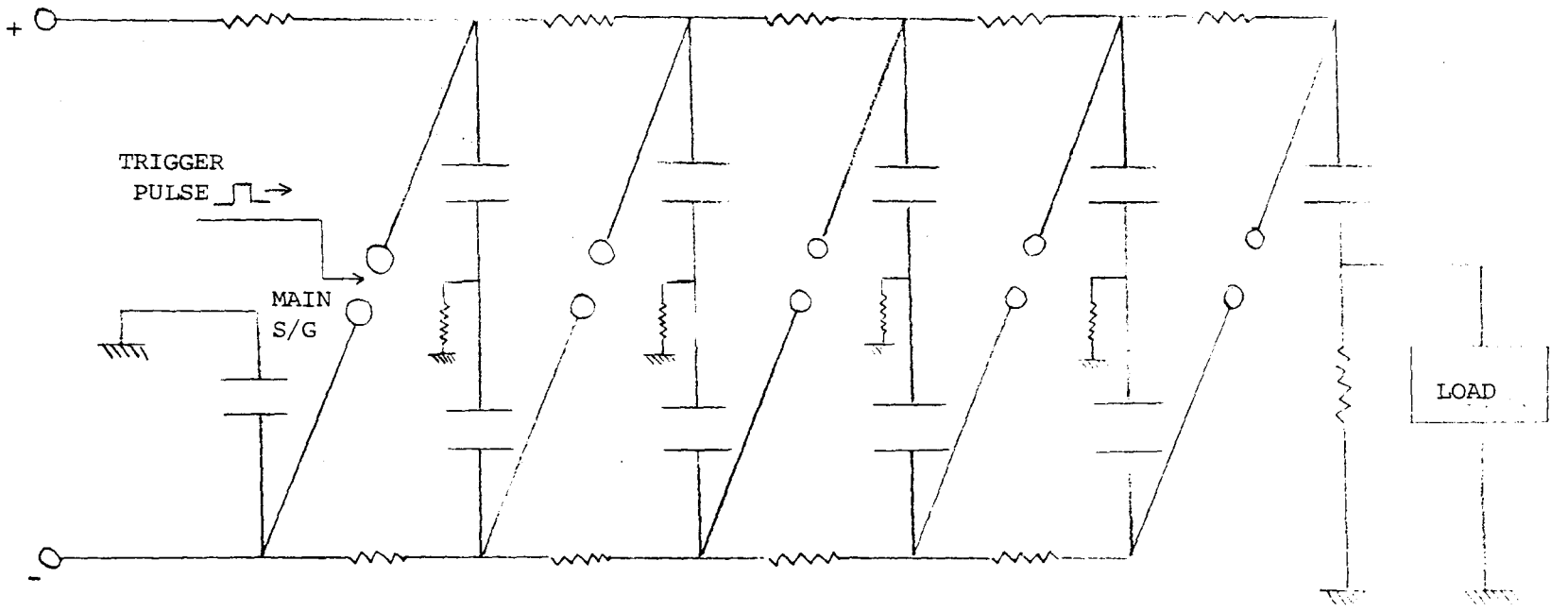

Fig. 2.1

SCHEMATIC DIAGRAM OF MARX CIRCUIT

Most of the work was carried out using either method (ii) or (iii) above with method (i) being used only rarely.

The spark gaps connecting the bank condensers were pressurised using nitrogen gas (or sometimes dry air) at sufficient pressure to hold off the high voltage (30kV-70kV) between the gap electrodes. Method (ii) consisted of removing the spark gap pressure at the desired moment by "flushing out" the gas in the gaps resulting in electrical shorting of the gaps. This pneumatic switching provided the additional bonus of removing electrode debris, cooling the electrodes, supplying fresh uncontaminated gas and thus improving the switch lifetime.

Method (iii) was the most frequently used method of switching the Marx. This was achieved by a field-distortion pulse applied between the electrodes of the main gap (the first of five gaps) on the Marx circuit. As a result of closing the first gap subsequent "overvolting" of the other gaps resulted in a rapid cascade process which switched the Marx into the external load. In order to prevent damage to the pulse transformer which provided the trigger pulse a capacitive block was placed between the main gap trigger electrode and the pulse transformer in case the main switch current passed through the trigger electrode circuit. Switching of the Marx on electrical trigger command was almost 100%

successful although sometimes the cascade process involved some time interval ($\lesssim 1\mu s$) between switching of the main gap and the successive overvolting of the other four gaps and very occasionally the first gap shorted with the other four gaps failing to close at all.

Similar Marx banks have frequently employed electrical triggering of more than one (perhaps of all) gaps, or some form of ultra-violet coupling (50) between the gaps to improve the reliability of Marx bank erection.

The first few shots of each new firing day tended to close before the bank reached full charging voltage despite spark gap pressure being unaltered. This premature switching was overcome by increasing the gap pressure a little initially until after a few shots when it had to be reduced again to achieve reliable switching. Pneumatic triggering of the Marx bank was carried out from the control box, Fig. (2.2), and electrical triggering was initiated from the screened room area, Fig. (2.2). To avoid introducing electrical noise into the screened room the electrical triggering circuit was located outside the screened room and was itself initiated by a pneumatic pulse from within the screened room.

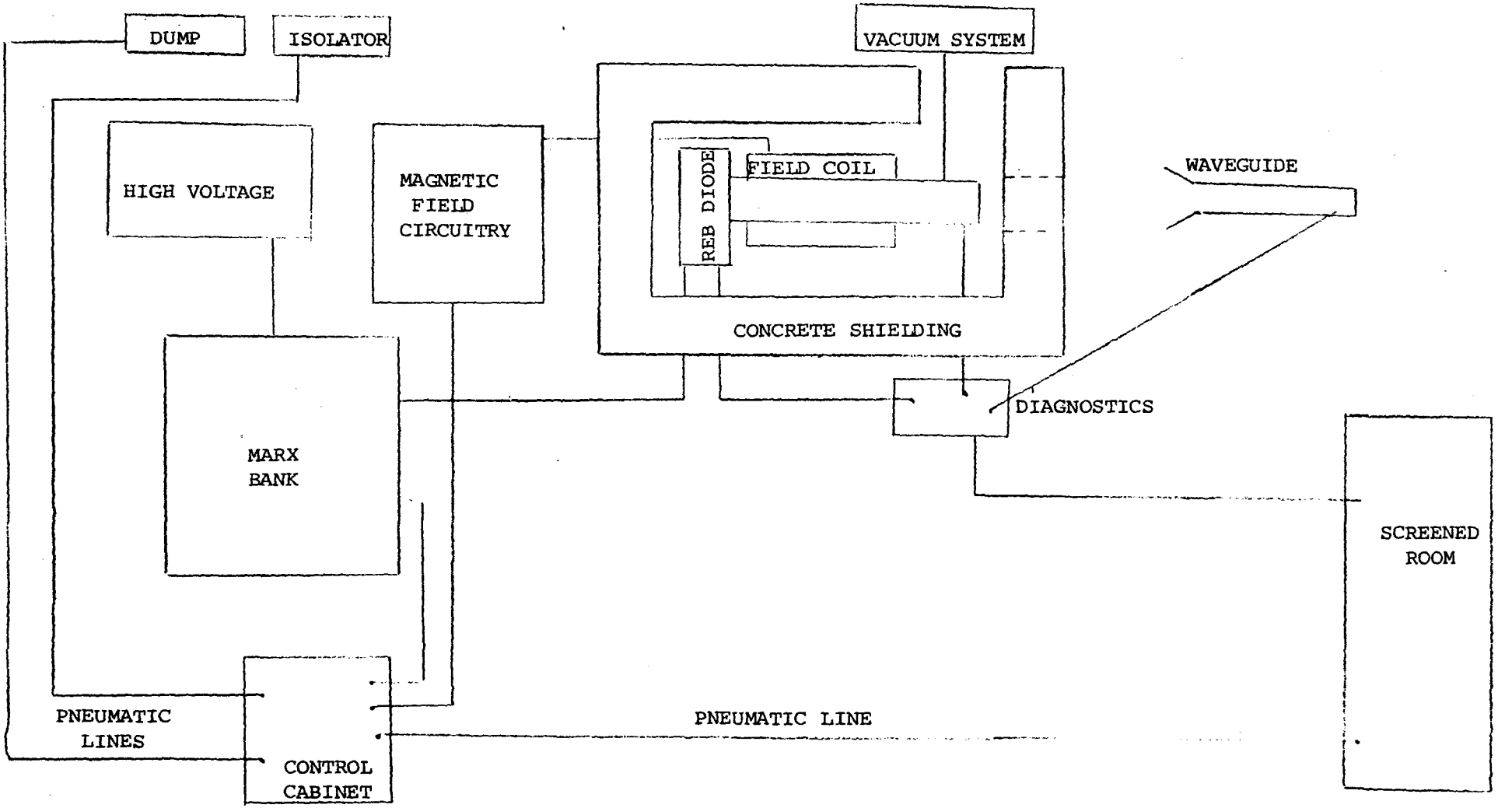
DUMP
ISOLATOR
VACUUM SYSTEM
HIGH VOLTAGE
MAGNETIC
FIELD
CIRCUITRY
REB DIODE
FIELD COIL
WAVEGUIDE
CONCRETE SHIELDING
DIAGNOSTICS
MARX
BANK
SCREENED
ROOM
PNEUMATIC
LINES
CONTROL
CABINET
PNEUMATIC LINE

Fig. 2.2

2.2.3 Marx Commissioning

Early tests of the Marx generator were carried out by firing the bank into a dummy resistive load (681Ω). This then was simply an RC discharge and a typical trace is shown in Plate (2.1). The short rise-time ($\lesssim$200ns) of the voltage across the load is as expected from the low-inductance Marx circuit (1.4 μH), and the measured Marx currents of $\lesssim$ 1kA were measured with the Marx voltage at a nominal 250kV.

The oscillograms were recorded in the screened room area, Fig. (2.2), and the oscilloscopes were normally self-triggered. An attempt was made to trigger the CROs from the light pulse given off by the Marx bank spark gap after it was demonstrated that a chopped helium-neon laser pulse after passing down a length of optical fibre and through a photo-diode and amplfier gave an output of several Volts. The optical signal from the gap proved large enough to trigger the oscilloscope, but the frequency response of the photo-diode amplifier was not fast enough to give a sufficiently short rise-time for the trigger pulse. Although the rise-time of the photo-diode itself was ≃ 250ns the full power bandwidth of the amplifier was 60kHz, however, as reliable triggering of the CRO did not appear to be a major problem this form of triggering was not pursued and a faster amplfier was

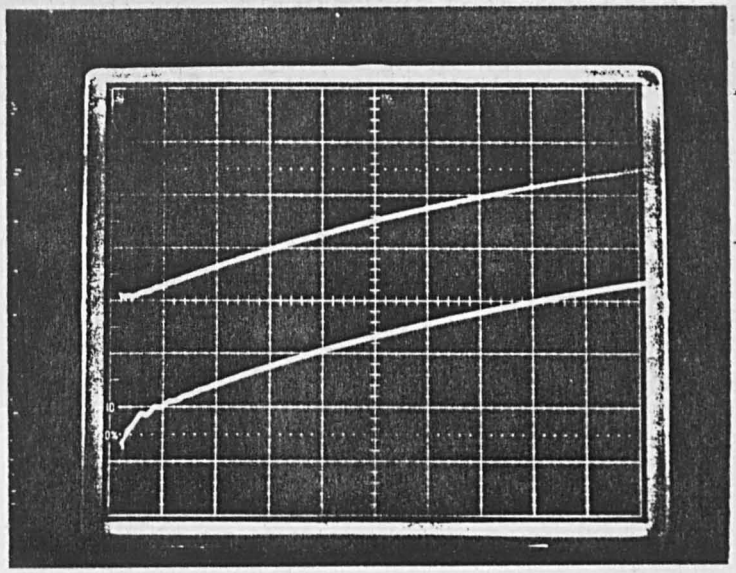

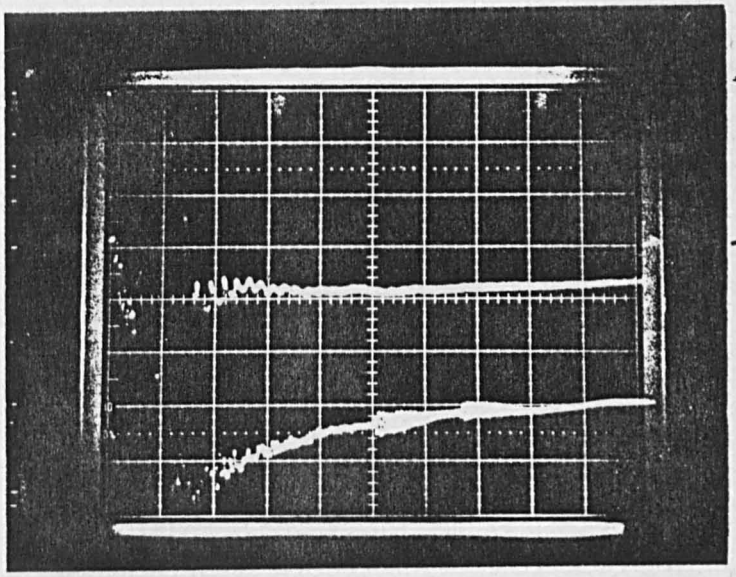

Plate 2.1. Discharge of Marx bank through a dummy load of 68Ω.

Marx charging voltage was 150kV.

Top: Top trace is diode voltage (23.2kV/div), bottom trace is Marx current (63A/div). Time-base - 2μs/div.

Bottom: As top but t.b. at 200ns/div.

not obtained for this purpose.

When firing the Marx bank into the diode, external resistances were connected between the Marx bank and the cathode. After diode gap closure the Marx current was determined by this impedance. In order to limit the magnitude of the low voltage diode-current and so prevent the diode from damage this series connected impedance was large. Typical equivalent circuits are shown in Fig. (2.3) and Fig. (2.4). The most common values of series resistance, R_s, were 247 Ω and 102.5Ω.

2.3 Marx-Magnetic Field Timing

To obtain the desired time-interval, τ, between the application of the external magnetic field and the injection of the electron beam the electrical trigger pulses to the separate capacitor banks were delayed with respect to one another using a dual pulse signal generator (FARNELL PG5222). The arrangement is shown schematically in Fig. (2.5.). Two pulse units (HML 350) were employed to provide trigger voltages for the trigger gaps of the magnetic field and Marx banks respectively. The units provided 300V pulses which were transformed up to ≃35kV through "HML" pulse transformers.

The first pulse unit was switched by a pneumatic signal from the screened room and sent simultaneous trigger signals to the magnetic field circuit and, from the "SYNC" output,

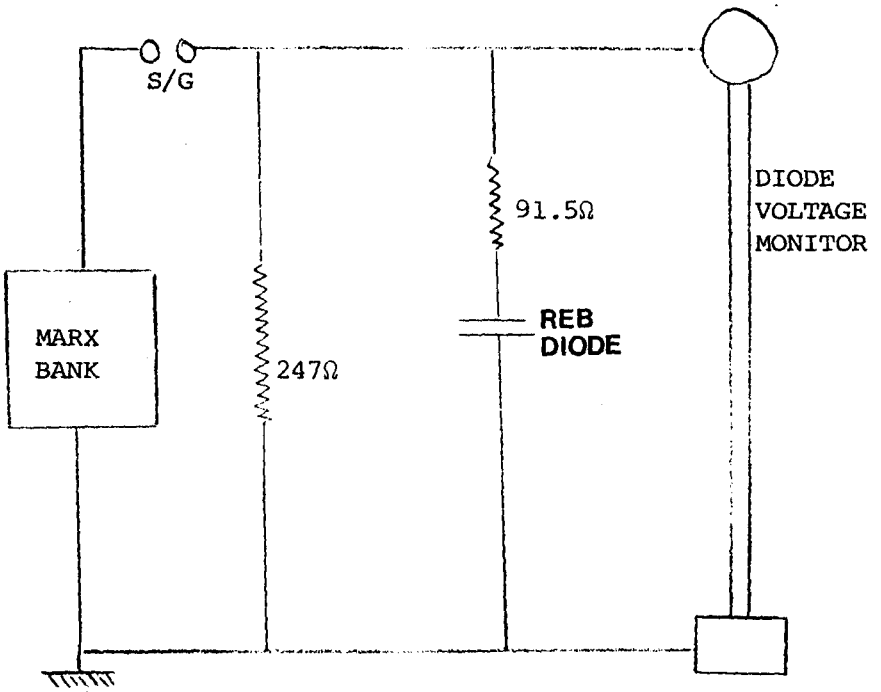

Fig. 2.3

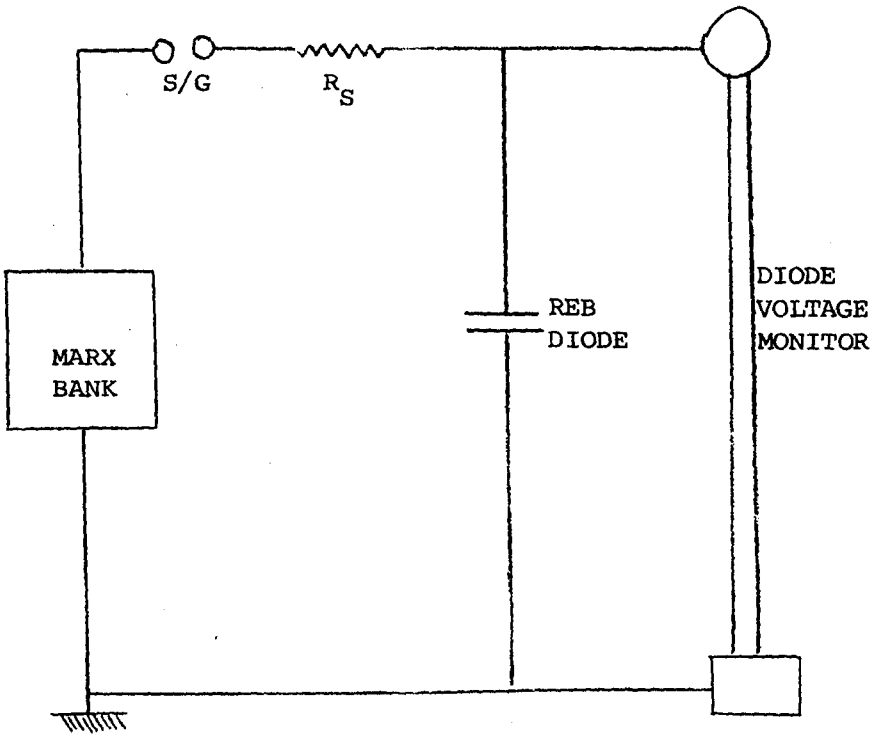

Fig. 2.4

TYPICAL EQUIVALENT CIRCUITS FOR REB DIODE EXPERIMENTS

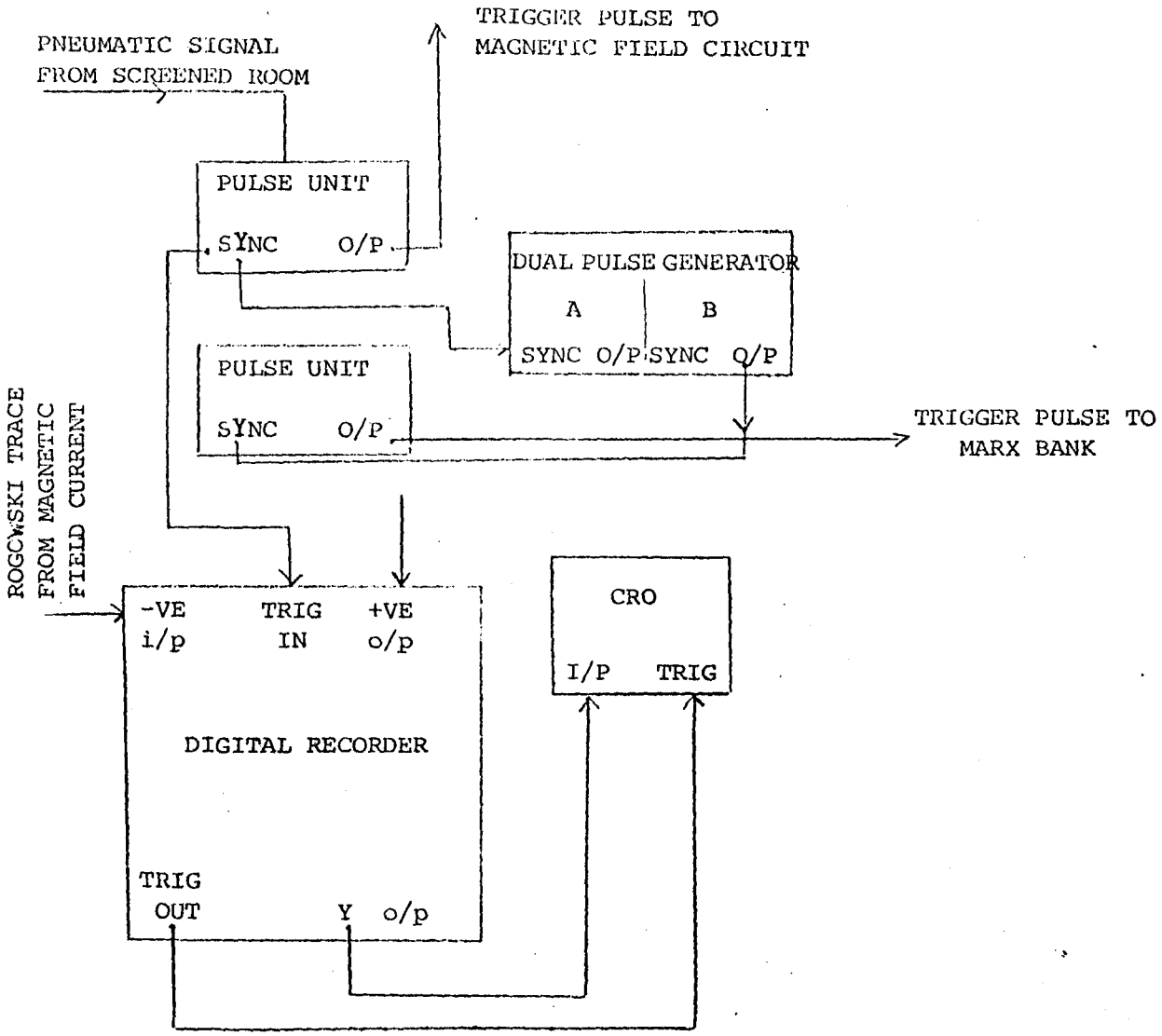

Fig. 2.5

Schematic Arrangement for obtaining desired Time-Interval between switching of magnetic field current and Marx Bank. Also arrangement for recording time interval.

to the 'A' channel of the dual pulse signal generator which, in turn, initiated a delayed pulse from the 'B' channel of the signal generator to the other pulse unit which provided the trigger pulse for the Marx circuit. The delay between the 'A' and 'B' channels of the signal generator was variable allowing the electron beam to be injected into differing values of external magnetic field. Accurate, stable and reproducible setting of the relative timing of the two circuits could be made by employing a digital frequency meter (Schlumberger Automatic Counter Model FB2602), used as a time interval meter, with a rough setting of τ being made by observing the displacement of the "FARNELL" generator outputs displayed on an oscilloscope time-base. As will be seen in Chapter Six typical values of τ were in the range 1.5ms to 4ms.

Successful timing was initially observed by monitoring the Marx current and magnetic field coil current traces obtained from a Rogowski loop and current shunt respectively (Chapter Four). An attempt to trigger the CRO t.b. from the 'SYNC' pulse of one of the pulse units resulted in inductive pick-up which drove the current shunt signal trace off the screen. This problem was overcome by triggering the CRO from the current shunt signal itself.

The pulse unit which provided the 'SYNC' trigger to the 'A' channel of the signal generator simultaneously triggered a digital storage oscilloscope which displayed a

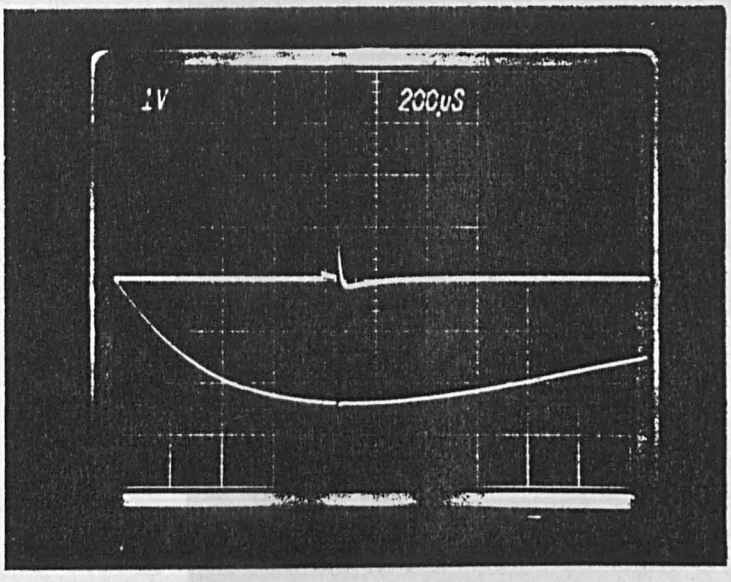

Plate 2.2. (a) Demonstration of time-interval between triggering of Marx bank and magnetic field circuit.

Top trace is Marx current. Bottom trace is magnetic field.

Time-base at 200μs/div.

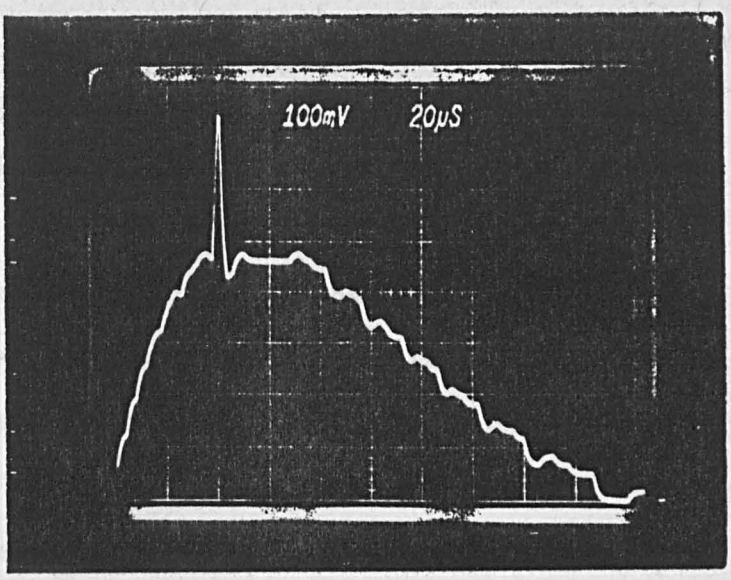

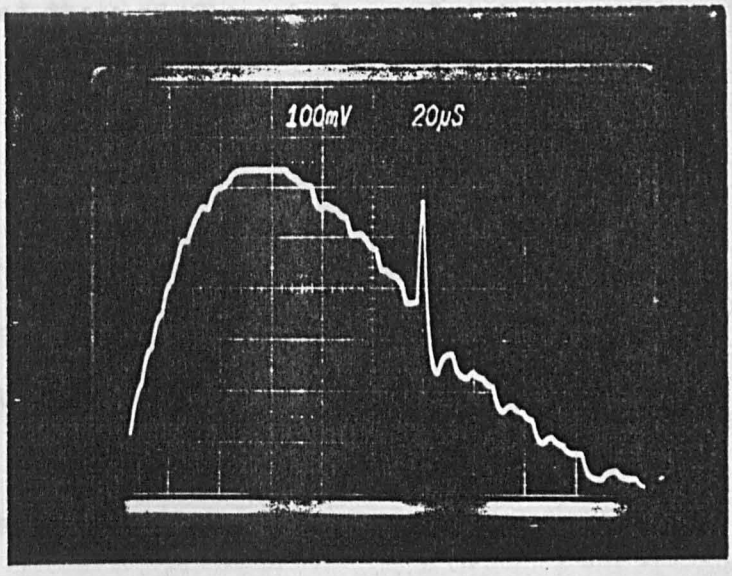

Plate 2.2. (b) Storage oscilloscope traces of magnetic field signal and Marx current signal for recording delay between switching of respective circuits.

Time delay was 0.5ms/div.

The sharp spike is the Marx current "riding" on top of the magnetic field trace.

Rogowski signal from both the Marx and magnetic field circuits providing a stored record of the timing between the switching of the two banks. These stored traces illustrated the presence of the occasional Marx bank misfire where electromagnetic pick-up switched the Marx simultaneously with the magnetic field bank or where the Marx bank failed to switch at all resulting in the electron beam"seeing"zero magnetic field and thus no microwave trace being present. The monitoring of the timing between the firing of the two circuits enabled these misfires to be excluded from the data analysis.

2.4 The Diode

The field-emission diode consisted of two conducting flanges, to one of which a circular mesh insert could be screwed to provide a transmission guide to the evacuated drift region. The other flange held a stainless steel hollow cathode stalk which acted as the emitter surface for the electron beam. The cathode stalk and the anode grid were co-axially aligned and a simple diagram is shown in Fig. (2.6.).

The cathode and anode flanges were separated by a distance of 10 inches (25.4 cm). Between the two flanges were ten one inch thick insulating perspex blocks with holes through the centre to allow the cathode stalk to protrude through. In order to try and improve the uniformity of the electric field between the anode mesh and the cathode stalk field grading rings were inserted between each perspex insulator. These annular rings were

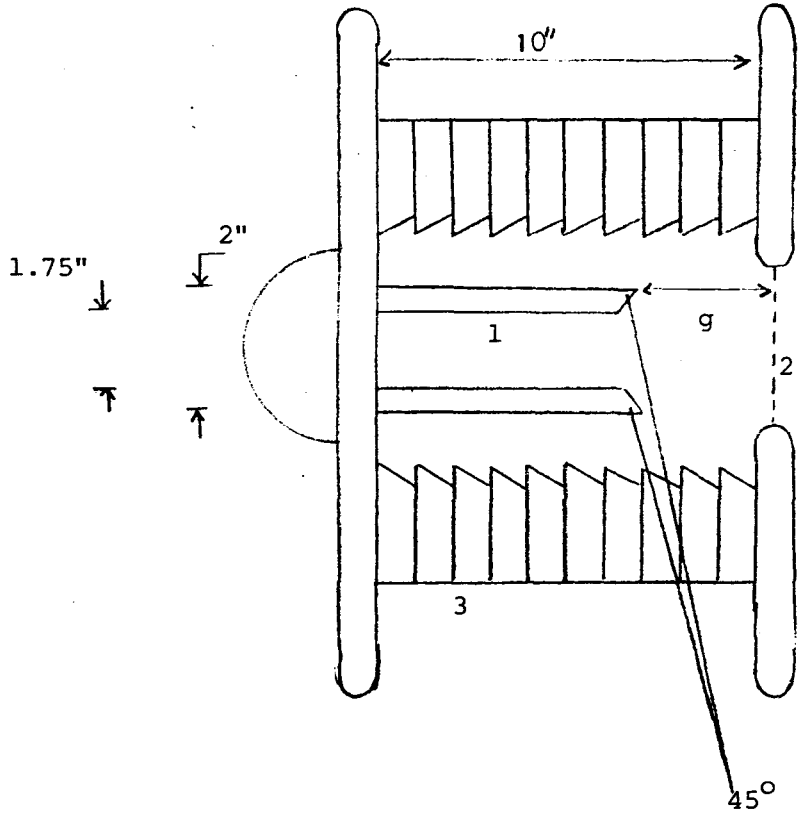

1. CATHODE
2. ANODE MESH
3. INSULATORS

Fig. 2.6

SCHEMATIC OF REB DIODE

made from duralumin and were contained between each of the insulators. In order to provide a good vacuum seal rubber 'O' rings were placed in grooves between each of the perspex insulators. The insulators were compressed tightly together by four threaded nylon tie rods passing through clearance holes at the corners of the perspex slabs and diode flanges.

In order to encourage hollow beam formation the cathode was made of a stainless steel annulus nominally three millimetres thick and of nominal outside diameter two inches (fifty millimetres). To enhance field emission the tip of the cathode was sharpened to have a forty-five degree tip angle, Fig. (2.6).

The anode mesh, held in the 2.5cm thick duralumin anode flange, had 2.36 wires per millimetre and each wire was 0.172mm in diameter giving a geometrical transparency factor of 35.2%.

The beam transmission element was chosen to be a grid rather than a thin foil as foil damage due to beam impingement would have necessitated frequent operation of the vacuum system. In addition, the mesh insert was expected to produce less of a scatter in the value of transmitted electron energy than would a thin foil.

In order to set the gap spacing the cathode-anode distance was set to zero and then the cathode stalk was pulled back through a required distance to within ± 0.5 millimetres, the

anode, of course, being in a fixed position. The zero A-K position was determined by an audio-signal from an ohmmeter with leads connected to both the cathode and the grounded anode. The diode was ultimately operated at gap settings varying from 3mm to 50mm.

2.5 Drift Region

Behind the anode flange was an evacuated four inch (10cm) QVF tube in which the beam drifted after having passed through the anode mesh. The background pressure was typically $\lesssim 2 \times 10^{-6}$ mbar. For the early diode impedance collapse work (Chapter Five) the electron beam was collected on a grounded stainless steel lamina placed about five centimetres behind the mesh insert. However, for the electron beam-microwave radiation experiments the beam was collected in the hollow cavity tube, of $(9.7 \pm .2)$cm dia., fitted on the inside of the glass tube. The cavity collector was made of 0.003 inches thick (76 microns) stainless steel sheet folded into a hollow cylinder and spot welded along its length, the length being 60cm or 104cm, the longer length being a soldered extension of the original. The grounded stainless steel cylindrical collector and stainless steel lamina provided a means of measuring the electron beam current by placing Rogowski belts around the return current cable.

The pulsed magnetic field coil was positioned at various points along the drift tube and for the microwave work was placed as closely as possible to the anode flange, this distance being limited by the insulating ring over the anode

flange. The field coil was of a larger diameter than the QVF tube (in order to fit over the flared ends) and was located concentrically with the tube by filling the distance between the tube and the coil former with a cushion of foam. This cushion allowed the coil some elasticity to move a very small amount axially under the repulsive force between the coil magnetic field and the eddy currents induced in the anode flange by the fast rising magnetic field without damaging the vacuum seal between the drift tube and the flange. The opposite end of the glass tube was terminated in a glass window whose transmission for X-band microwave radiation was measured at 70%.

The entire diode and vacuum region was surrounded by an 18 inch thick concrete wall to provide shielding from any X-rays produced by high energy electrons striking metal components of the diode or vacuum flanges. No concrete roofing was required as the distance between the drift region and any object above this region was so large as to have made any X-ray flux negligible at this distance.

2.6 The Vacuum System

The arrangement used to obtain the vacuum in the diode and drift tube spaces is shown schematically in Fig. (2.7.). The high vacuum was achieved using a commercially available "Edwards Diffstak", a water cooled oil vapour diffusion pump.

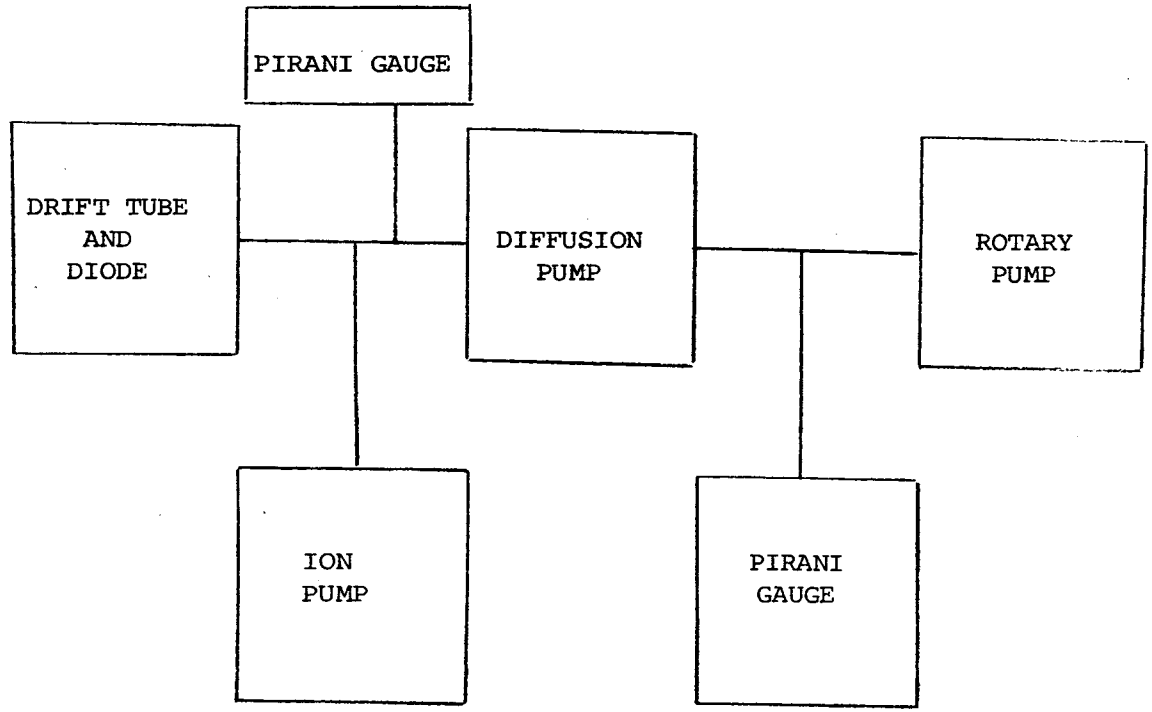

Fig. 2.7

SCHEMATIC OF VACUUM ARRANGEMENT

The pump had a 100mm inlet bore and a pumping speed of 280 litres/second. The oil employed in the diffusion pump was "Santovac 5" which exhibits low back streaming effects thus circumventing the need for a liquid nitrogen cold trap. Partial pressures due to contaminants were kept down using a water cooled baffle. The high vacuum pressure achieved was typically 2×10^{-6} millibar, measured using an ionisation gauge.

The roughing pressure was obtained using an "Edwards ED100" rotary pump. The backing pressure was measured using a Pirani gauge.

2.7 Noise Elimination

In order to reduce electromagnetic pick-up great care was taken to avoid any kind of coupling between different parts of the charging units, trigger units and monitoring equipment. All earth connections were made to a common earth to avoid earth loops and the accompanying inductive signals. Filters were employed between the mains power and the EHT charging unit for the Marx bank and the screened room where the signals were recorded and where electrical switching of the Marx bank was initiated. Proper arrangement of earth connections was necessary both for proper signal recording and to effectively isolate the different triggering circuits ensuring that the correct sequence of switching could be achieved.

3.1 Introduction

The attraction of microwave production via the process of electron cyclotron maser action is that it offers the possibility of high power operation at millimetre and submillimetre wavelengths.[51] However, in order to achieve such small wavelengths it has been seen that one has to employ very large magnetic fields or obtain emission at high harmonics of the fundamental cyclotron frequency. Although gyrotrons will still emit high radiation levels at harmonics of the cyclotron frequency the efficiency of operation is inherently lower and, in fact, excessive energy spreading of the electron beam will put a fundamental limit on the available magnitude of harmonic at which cyclotron maser action can occur.[52] An important parameter, therefore, in any ECM device is the magnitude of the magnetic field with which the machine is operated.

The electron cyclotron frequency for relativistic electrons spiralling in a magnetic field, B, is given by the expression,

$$\omega_{ce} = \frac{\eta B}{\gamma} \qquad (3.1)$$

where γ is the usual relativistic factor and η is the charge to mass ratio of the electron. Equation (3.1) reduces, in the non-relativistic limit, to,

$$f = \frac{\omega_{ce}}{2\pi} = 28 \text{ GHz} \left[\frac{B}{\text{Tesla}}\right] \qquad (3.2)$$

For magnetic confinement fusion devices, in which the plasma is typically contained by fields of (1-10) T, centimetre and millimetre wavelengths are, therefore, of interest for electron cyclotron resonance heating experiments.

The required high magnetic fields for such studies have been produced in a number of experiments with the aid of superconducting magnets thus allowing both pulsed and c.w. modes of operation to be investigated.[53]

The alternative to superconducting techniques for applications requiring large volume high magnetic fields is the use of pulsed discharge stored energy sources and, indeed, the experiments with which this thesis is concerned involved the discharge of capacitively stored energy through a wire wound solenoid. Economics and practical constraints regarding the availability of large energy storing capacitors limited peak magnetic field values to $\simeq 0.6$ Tesla. The pulsed field circuit which was built served the dual purpose of providing an interaction region for the electron beam and providing a pulsed current source for the purpose of calibrating the various Rogowski belts which were eventually employed to measure the Marx bank and electron beam currents (Chapter 4).

3.2 Magnetic Field Capacitor Bank

The choice of energy storage to supply the solenoid current for magnetic field production lay between a set

of eleven 0.5 μF, 20kV working capacitors and four 300μF capacitors capable of being charged to 4kV. The obvious energy storing capability of the 300 μF capacitors was offset by their limited lifetime if allowed to undergo any appreciable degree of voltage reversal. In order to protect these capacitors, therefore, it was found necessary to have sufficiently high resistance in the discharge circuit to limit the current variation and, hence, magnetic field variation with time to be close to the critical damping condition, [54]

$$\frac{R^2C}{4L} = 1 \quad (3.3)$$

where R,C and L are the circuit resistance, capacitance and inductance respectively. Fortunately, the required external resistance necessary to meet the above condition was not much greater than the resistance of the wire used in winding the magnetic field coil. Both sets of capacitors had practical advantages apart from their energy storage capability. In order to acquire data rapidly itwas desirable to be able to charge the capacitors quickly. The 0.5 μF, 20kV capacitors charged quickly, holding smaller charge, however, this was partially offset by the fact that, of the available E.H.T. units, those able to charge to 20kV could provide no more than 5mA charging current. The 300 μF capacitors on the other hand, could be charged simultaneously by two E.H.T. units each capable of providing 10mA but only capable of charging to approximately 3.5kV. The 0.5 μF capacitors could be operated in an underdamped discharge circuit thus

allowing more efficient use of the stored electrical energy. However, the high frequency oscillations of current associated with such a device proved inferior for use with the electron beam pulse in comparison with the slower rising, longer decay time profile of the near critical discharge appropriate to the 300 μF capacitors. As will be discussed later, the coil dimensions used in the electron beam experiments resulted in a spatially non-uniform magnetic field distribution. Naturally, in order to best interpret any microwave emission from the electron beam it would be undesirable to have both a spatially and temporally varying field for the REB to interact with. The slow discharge associated with the high C of the 300 μF capacitors proved ideal in providing an effectively magnetostatic field for the electron beam. The fast "ringing" discharge of the small capacitance circuit, on the other hand, meant that the magnetic field would appear constant to the electron beam only if the Marx bank was fired at a turning point in the current profile with time, thus making the electrical timing between the beam circuit triggering and magnetic field triggering much more critical, and limiting the various magnetic fields at which the beam could be fired to those associated with the current maxima and minima of the exponentially decaying sinusoidal trace.

In addition to the slow decay time the larger capacitors were advantageous from the point of view of the long

rise-time ($\simeq$ 1ms) associated with the critical damping trace. This long rise-time allowed the solenoidal field flux to leak through into the evacuated drift region through the stainless steel collector upon which the beam electrons impinged after having travelled through the diode. The thin, 0.003" (76.2 microns), cylindrical collector would have been collapsed by the large magnetic pressure due to the current carrying coil if the magnetic flux had not been able to leak through to the interior on a time scale short in comparison with the circuit rise-time, thus balancing the external field pressure. An estimate of the time required for the flux to diffuse through the steel collector was made from the characteristic diffusion time, τ_D, for the field through the metal.

$$\tau_D \simeq \mu_o \mu_r \sigma L^2 \qquad (3.4)$$

where L is the thickness of the stainless steel, σ is its conductivity, μ_o is the permeability of free space and μ_r is the permeability of the stainless steel, equal to unity. With σ approximately $1.04 \times 10^6\ \Omega^{-1}\ m^{-1}$, τ is seen to be the order of 10ns. This fast flux leakage time, negligible in comparison with the circuit rise-time, was verified experimentally by observing the time-integrated signal from a small pick-up probe inserted inside the coil region both with and without the presence of the collector. No observable difference was seen in signal size for the two conditions and visual inspection of the steel collector showed no signs of

buckling as a result of the pulsed magnetic field.

For a given circuit configuration it is obvious that the size of field obtained will be limited by the volume over which one wishes to generate this field. The diameter of the coil finally employed could not be smaller than the evacuated QVF tubing in which the electron beam drifted, therefore the smaller the length of the coil the higher the magnetic field obtained at the centre. However, as was stated above, the microwave spectrum from the magnetic field region is more readily understood if the field is uniform, for which a long coil is necessary. To this end the length of the coil was chosen to be such as to give 10% spatial uniformity in the axial magnetic field for a distance of a few wavelengths of the anticipated electromagnetic radiation. This criteria, nevertheless, is short of what one would really like but was the result of a trade-off between the magnitude of the magnetic field attained and the degree of spatial variation.

3.3 Field Coil Design

The expression for the maximum current achieved in either an underdamped or overdamped RCL discharge circuit is a sensitive transcendental function of the variables R, L and C. Therefore, in order to calculate an estimate of the peak current to be expected from any configuration an accurate measurement of the values of resistance, inductance and capacitance is necessary. The resistance of the discharge circuit was easily measured with a

digital multimeter across the spark gap terminals with the capacitor connections shorted out. Similarly, the circuit capacitors could be measured with a digital capacitance meter and due to the values involved were assumed to swamp any other capacitance involved.

The stray inductance of the circuit, however, could not, in the first instance, be considered negligible or easily calculable. In order to obtain an estimate of this inductance an obviously underdamped discharge was arranged as measurements of oscilloscope traces in this condition allowed the inductance L to be calculated from, independently, the circuit period and the ratio of the first maxima to the first minima. Indeed the underdamped condition provides the only equations in R, C and L from which L can be completely factored. As was done for the flux leakage experiment a small search coil was inserted inside the solenoid and an integrated signal was recorded on the oscillogram. The search coil did not need to be accurately aligned or situated inside the magnetic field coil as one measurement involved the ratio of two signal voltages and the other involved a measurement of the signal period. The expression for the circuit inductance, L, in terms of the ratio of the first maxima to the first minima is given by,

$$L = \frac{R^2 C}{4} \left[1 + \left[\frac{\pi}{\ln \Delta} \right]^2 \right] \qquad (3.5)$$

where Δ is the ratio of first maxima to first minimum. The inducance, L, is given in terms of the angular frequency, ω , of the pulsed discharge by the expression,

$$L = \frac{1}{2\omega^2 C}\left[1 + \sqrt{1 - (\omega RC)^2}\right] \qquad (3.6)$$

The resultant value of L had the calculated value of the inductance of the test coil subtracted from it to provide a reasonable estimate of the stray circuit inductance (10 μH). This stray inductance was negligible compared with the inductance of the coils used to provide the magnetic field. The calculated inductances of the solenoidal coils were carried out using the expression (55)

$$L = FN^2\left[\frac{d}{2.54}\right] \mu H \qquad (3.7)$$

where d is the diameter of the coil in centimetres and N is the number of turns in the coil. The quantity F is a factor dependent upon the ratio of the coil's diameter to length and its value for different ratios is tabulated in Terman (55). The values of F pertinent to the coils in these experiments were obtained by linear interpolation of the tabulated data. The resulting values of L for the various field coils are given in table (3.1). The calculated values agree, within experimental error, with those obtained by measurement of the inductances on an a.c. bridge.

The calculated estimates of peak current expected from the various R, L and C's employed made it possible to

Coil	Calculated inductance mH
1	0.336 ± 0.005
2	2.55 ± 0.03
3	2.65 ± 0.03

Table 3.1

CALCULATED INDUCTANCES OF COILS USED IN PRODUCING PULSED MAGNETIC FIELDS

design small pick-up probes with suitable geometries to give sufficiently sensitive measurements of the longitudinal magnetic field distribution through the coil (Chapter 4).

The important consideration in the design of the magnetic field coil was to construct a coil which would provide as large a magnetic field as possible while simultaneously satisfying certain practical and physical constraints. In addition to the constraints concerning the length and diameter of the coil mentioned above it was necessary to have a coil which, undergoing a current pulse, would avoid the following occurences:-

(i) heat up to any large extent;

(ii) have a frequency dependent resistance for the type of current rise-time experienced;

(iii) experience an increase in resistance due to heat dissipation;

(iv) burst apart as a result of magnetic pressure.

Pulsed magnetic field coils generally fail to heat up as a result of thermal inertia (54) . However, it is reasonable that if one wishes to limit temperature rises it can be done by limiting the current flowing through the solenoid turns. For any type of discharge the magnetic field achieved is, in fact, insensitive to the number of turns in the coil. (B, of course, is proportional to NI_{max} however, $I_{max} \propto L^{-\frac{1}{2}}$ and therefore to N^{-1}).

Hence, if one wishes to achieve a large field, a small current flowing through a large number of turns is equally effective as a larger current flowing through a small number of turns (for a given coil length). A small current, apart from helping the coil not to melt, is advantageous from the point of view of the spark gap switch whose damage, and therefore life-time, is dependent on the currents which it is required to switch. Calculations on the field coils employed indicate that if all the stored energy was dissipated in the coil the peak expected temperature rise would be less than $10^{o}C$.

Changes in resistance with temperature are undesirable as they complicate the understanding of the temporal development of the circuit current, as well as acting to reduce the maximum current achieved. Obviously solving the problem of a large temperature change solves the problem of resistance change. The above upper estimate of the expected temperature change indicates changes in resistance due to Joule heating will be absent.

Similarly, if the current pulse is suitably short then skin effects in the current carrying wires will act to make the resistance in the coil, and the rest of the discharge circuitry, frequency dependent. Again, such behaviour would serve to make analysis and predictions regarding the circuit difficult as well as to make the resistance greater and the achievable field smaller.

The above problem was alleviated by using the larger capacitors with the longer rise-time, hence this was another argument in their favour.

While making preliminary measurements with a test field coil (coil # 1 below) the solenoid turns at the end of the coil were observed to have moved apart after receiving a pulse of current. As each turn of the coil carries current in the same direction one would expect the turns to pull together during a current pulse and so the separation of the end turns after each pulse is assumed to be a combination of the elasticity of the solenoid wire insulation and due to the interaction of the end turns with the fringing fields of the coil. Gradual increase in the current passed through the coil resulted in excessive disturbance of the coil windings.

In order to prevent a similar disturbance to the final coil design subsequently wound coils were treated to fix the positions of the coil windings. The coils were braced with insulating rods such as to prevent radial movement of the windings and dowels were placed at the end of the solenoid to prevent axial motion of the end turns. Finally, the entire coil was smeared with an epoxy resin.

The variation of current with time in any RLC discharge is given by the following equation,

$$I(t) = \frac{V_o}{L} \; e^{-\mu t} \; \frac{\sin \omega t}{\omega} \qquad (3.8),$$

where,

$$\omega^2 = (1-d)/LC,$$

$$d = \frac{R^2 C}{4L},$$

$$\mu = \frac{R}{2L},$$

and V_o is the voltage to which the capacitors are charged. From equation (3.8) it can be shown that the peak current expected from a given discharge will be given by,

$$I_{max} = \frac{V_o}{\omega L} \; k(d) \sin \omega t_o, \; (d<1), \qquad (3.9a),$$

$$I_{max} = \frac{V_o}{\omega L} \; k(d) \sinh \lambda t_o, \; (d>1), \qquad (3.9b),$$

where $\lambda^2 = -\omega^2$, t_o is the time to peak current and $k(d)$ is a monotonically decreasing function of d given by,

$$k(d) = \begin{cases} \exp\left[-\left[\frac{d}{1-d}\right]^{\frac{1}{2}} \tan^{-1}\left[\frac{1-d}{d}\right]^{\frac{1}{2}}\right], & d<1, \quad (3.10a) \\ \exp\left[-\left[\frac{d}{d-1}\right]^{\frac{1}{2}} \tanh^{-1}\left[\frac{d-1}{d}\right]^{\frac{1}{2}}\right], & d>1, \quad (3.10b) \end{cases}$$

The function $k(d)$ is plotted in Appendix 2 and is after de Klerk (75). The values of $k(d)$ for $d<1$ and $d>1$ where calculated from equation (3.10b) rather than the erroneous relation given by Montgomery (54) in which he assumes that

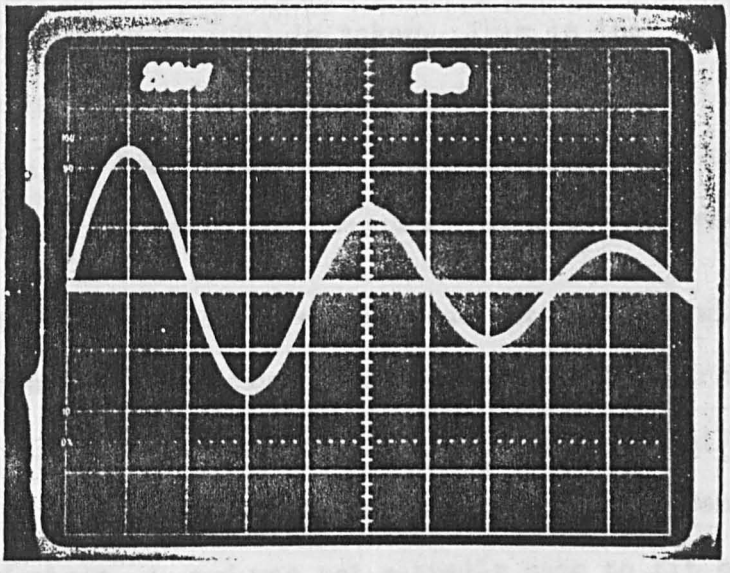

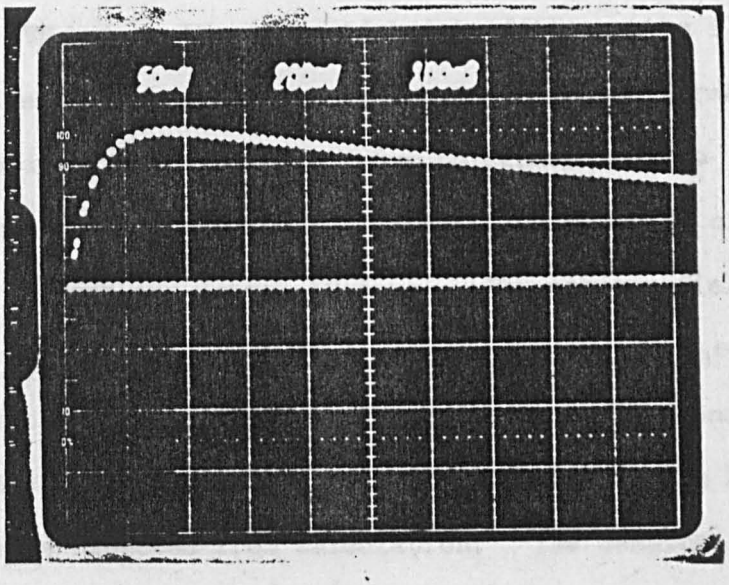

Plate 3.1. Top: Typical underdamped magnetic field circuit trace (d = 0.006). 50μs/div.

Bottom: Typical overdamped magnetic field circuit trace (d = 34). 100μs/div.

equation (3.10a) will be correct for d<1 and d>1 if the modulus of $(^{1-d}/_{d})$ is taken. This is the first occasion, to the author's knowledge, that this correction has been reported. Equations (3.9) were used to estimate peak currents for the coils employed in these experiments.

In all, the magnetic field circuit was investigated with three different coils whose constructions are illustrated in table (3.2). Coil # 1 was used only to give familiarity with the actual behaviour of the discharge at different damping factors, d, and was not actually made to fit over the QVF tubing. This tubing was standard four inch diameter QVF but as the solenoid had to fit over the flared ends of the QVF the turns were wound on a plastic former of inside diameter 16.2 cms and 6mm thickness to give the former some strength. As a result the diameter of coil # 2 was 16.9cms and length 19.6cms. The maximum field achieved with coil # 2 with all four 300μF capacitors employed and circuit resistance being only that of the coil and connections was 0.33 Tesla. This value was within 2% of the value expected from calculation. The damping factor for this arrangement was 4.24.

Pulsed magnetic fields are more efficient the smaller the damping factor is, as less of the stored energy is dissipated in resistive elements. However, coil # 2 as used above could not have any more resistance removed from the discharge circuit without actually reducing the number of turns and, hence, length of the coil, already smaller than one would

Coil	Length cm	Diameter cm	Number of turns
1	13.2	12.3	65
2	19.6	16.9	157
3*	19.6	16.9	160

* Double layered coil

Table 3.2

GEOMETRIES OF COILS USED IN PRODUCING MAGNETIC FIELDS

ideally wish. The alternative way to make the coil less resistive without decreasing the length of wire used to wind it is to use wire of greater diameter. However, for a given length of solenoid this would result in a decrease in the number of turns and, hence, field value. The effective area of a current carrying loop can be made larger, however, not by increasing the diameter, but by having two turns, one on top of the other, i.e. a double layer coil with the layers connected in parallel. The effect of this arrangement is to halve the d.c. resistance of the coil while leaving the inductance essentially the same and, hence, reducing the damping factor by a factor of four (N.B. normally two lumped parameter inductors of equal value connected in parallel will result in an effective inductance of half of either. For the above arrangement though the inductance must be considered as a distributive element and consideration of energy from first principles shows that the inductance remains the same for any number of parallel connected layers as long as the thickness of the resulting coil is small in comparison with the diameter.) Coil # 1 was re-arranged to have a double layer arrangement but with the layers being connected in series. This resulted in about 40% increase in the field over the single layer but this increase was due to the coil being halved in length rather than the increase in line density of turns for the solenoid. In winding this double layer coil, at the end of

the first layer the wire was taken back along the direction of the cylindrical axis of the coil to reduce the potential difference between the two layers.

Although a series connected double layer coil has twice as many turns per unit length the accompanying increase in circuit resistance results in no change in achieved field although the current in the external circuit is reduced (assuming V_o is fixed).

With these considerations in mind coil # 3 was wound with a parallel connected double layer and dimensions similar to coil # 2. Coil # 3 achieved the highest magnetic fields over the desired volume and thus most of the work on beam-field interaction was carried out using coil # 3.

3.4 Field Coil Current Measurements

Solenoid currents were measured by the potential drop across a fixed resistance in the RLC circuit. The resistor employed was a cylindrical stainless steel current shunt. The shunt consisted of an annulus 0.003 inches thick, 5cms long and of radius 9.5mm (nominal) soldered to hemispherical brass end connections into which external connections could be made and fixed. The current shunt was of the "four-terminal" variety to ensure reliable measurement of the circuit current (attempts at measuring the p.d. across known resistances inserted into the circuit proved futile as the implied currents were clearly erroneous, probably due to poor and varying contact resistance). The D.C. resistance

of the current shunt was measured in a simple ohmic circuit in a similar fashion to the shunt discussed in Chapter IV. The value obtained was in good agreement with that calculated from the dimensions and resistivity of the stainless steel shunt. Currents of the order of 700A were recorded flowing through coil #3, indicating peak magnetic fields of $\simeq 0.6$T.

A typical magnetic field circuit arrangement is shown in Figure (3.1) with the equivalent circuit shown in Figure (3.2). The two E.H.T. units charged the capacitors through R_{C1} and R_{C2}, the charge current limiting resistors. R_B is a "bleeder" resistor through which the capacitors, if charged, may discharge in the event of a fault in the switch or the triggering apparatus. The solenoidal coil was connected to the circuit via a five metre long co-axial cable with o.d. = 13.44mm and i.d. = 2.85mm, with polyethylene insulation between outer and inner. This cable added a small (1.5 μH) inductance to the circuit but allowed the field coil to be mounted in the vacuum diode area remotely from the capacitor and E.H.T. location. A, is a modified milliammeter to measure the charging current (0-20mA) from the E.H.T. units.

3.5 Magnetic Field Triggering

The magnetic field circuit could be triggered off in either of two ways. Firstly, a "gravitational dump" which consisted of a length of insulating string which could be held manually so preventing the gap from sparking over until the string was released as required.

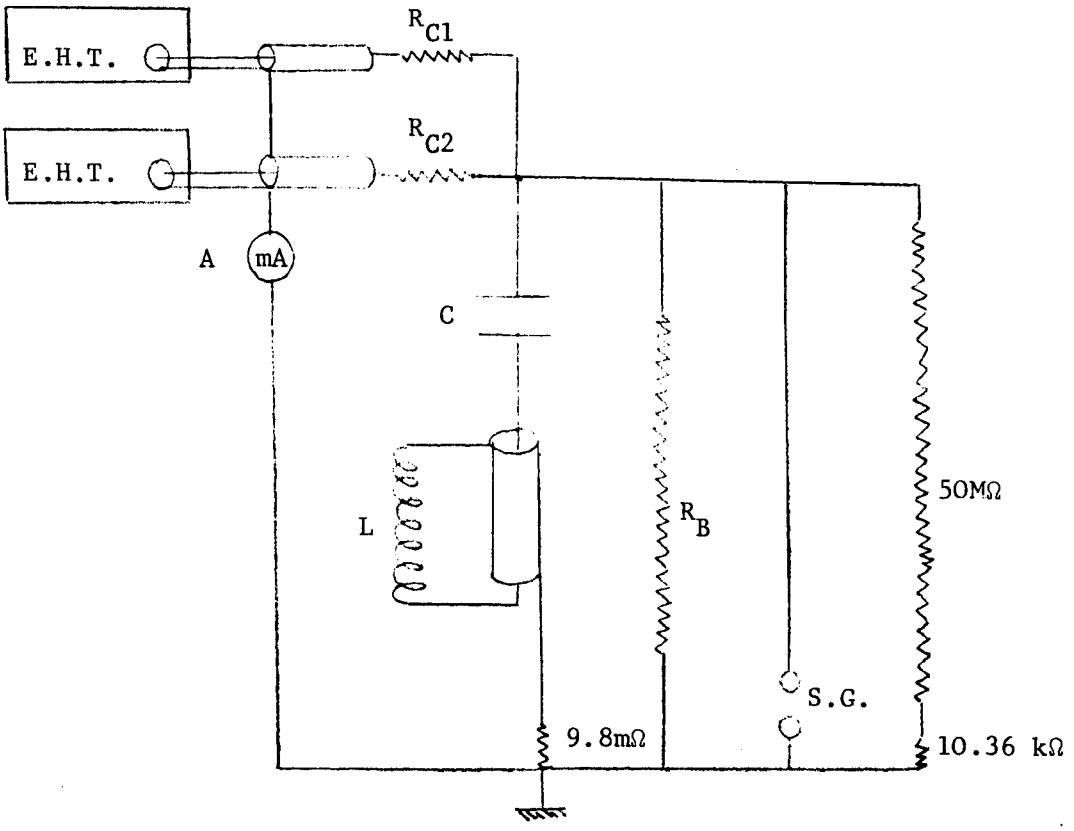

C - capacitors for energy storage

L - magnetic field coil

R_B - bleeder resistor

R_{c1}, R_{c2} - charge current limiting resistors

Fig. 3.1

ARRANGEMENT FOR CHARGING MAGNETIC FIELD CAPACITOR BANK

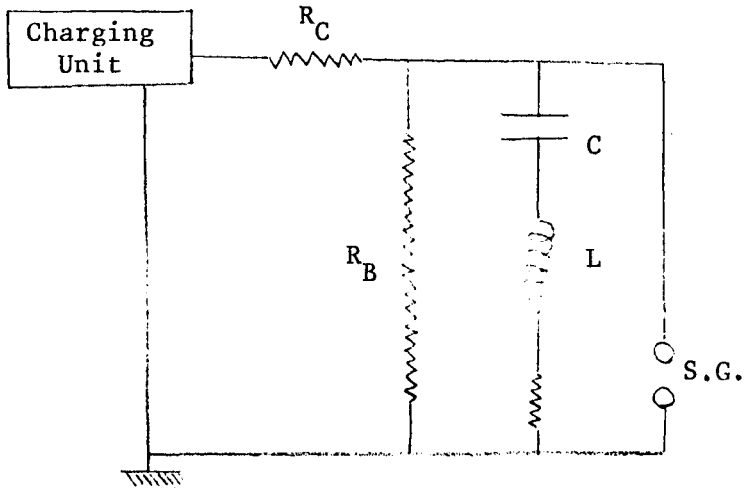

C - capacitors for energy storage

L - magnetic field coil

R_C - charge current limiting resistor

R_B - bleeder resistor

Fig. 3.2

EQUIVALENT CIRCUIT FOR CHARGING MAGNETIC FIELD CAPACITOR BANK

Secondly, an electrical trigger circuit was built which closed the spark gap electrically at the instant required. Obviously for controlling the time interval between the magnetic field pulse and the electron beam pulse an electrical spark gap is necessary, as well as being desirable, for safe and remote switching of the circuit at high voltage. These two switching methods were connected in parallel across the discharge circuit and the electrical trigger unit is shown in Figure (3.3). The mechanical triggering proved useful, nevertheless, for early tests of the magnetic field behaviour with the high voltage, low capacitance condensers, but the slow short circuiting time associated with this method made them useless for work at lower voltages. For example, when charging with a power unit which operated at 300V the magnetic field traces recorded using a small search coil had strange features such as an oscillatory discharge where the first maxima was smaller than the second maxima and the traces had sharp discontinuities in them rather than the smooth, damped sinusoidal trace expected. Evidently the coil current in these conditions was being determined by the time variations in the spark gap impedance during discharge as well as the RLC parameters inserted in the discharge circuit.

The spark gap consisted of a small brass trigger pin, machined from a 2B.A. bolt,between two hemispherical brass electrodes, one of which was earthed and the other

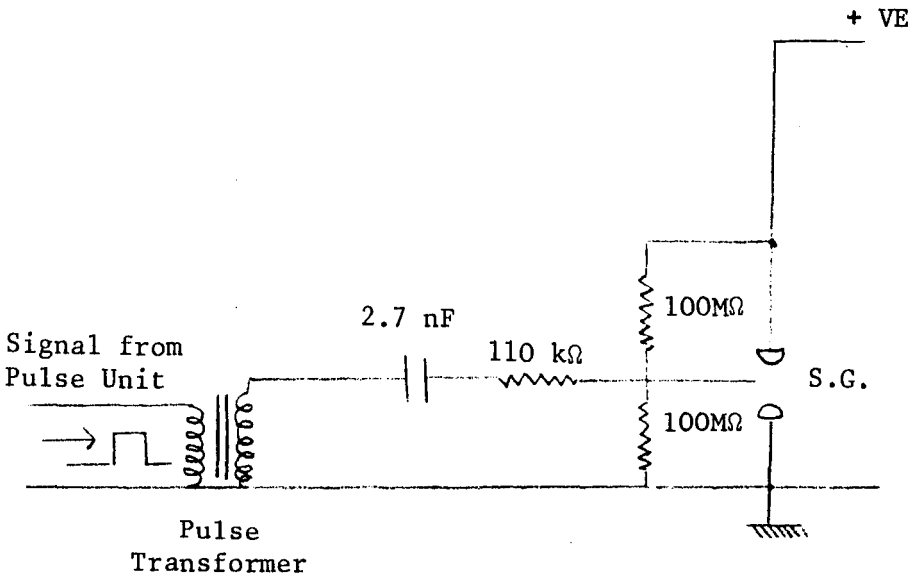

Fig. 3.3

TRIGGER ARRANGEMENT FOR MAGNETIC FIELD CIRCUIT

of which was connected to the positive high tension end of the capacitors. The brass electrodes were adjustable in separation allowing the gap to operate at different ranges of voltages and allowing operation of the gap after the electrodes had been worn or damaged by the discharge by simply changing the electrode spacing.

A voltage pulse from a pulse unit was applied to the primary of a pulse transformer and the pulse from the secondary of the transformer was fed to the trigger pin which was responsible for closing the gap. The voltage pulse to the pin was +35kV.

The electrodes and trigger pin were contained in a cylindrical perspex tube. Operation was in air at normal atmospheric pressure and so from time to time the gap required cleaning and machining of the electrodes due to the damage by the discharge currents of several hundred amps. The connections from the pulse unit to the input terminals of the transformer were such as to cause the trigger spark to go to the earthed electrode initially and then to flash across to the positive electrode. Operation of the trigger pin at negative voltage resulted in sparking across to the upper electrode but less reliable switching of the whole gap. The sign of the voltage (w.r.t. earth) on the trigger pin was determined by applying a small voltage pulse to the transformer input and observing the resulting small signal ($\simeq$ 10 Volts) between pin and earth.

CHAPTER 4 DIAGNOSTICS

4.1 Introduction

This chapter deals with the various diagnostics developed to measure the Marx bank voltage setting, external magnetic field value, large-scale electron beam properties, and the diagnostic arrangement used to obtain some estimate of the total emitted microwave radiation power.

4.2.1 Voltage Measurements

Two voltage measurements were of prime importance for the diode impedance experiments (Chapter 5),

(a) the d.c. voltage to which the Marx bank was charged;

(b) the transient beam diode voltage after the discharge of the Marx generator.

The measurements of signals of the latter type are generally accomplished using resistive or capacitive divider techniques [56] and for this series of experiments the former method was employed. Diode voltage has been observed to be an important parameter in other pulsed microwave experiments [57] and is generally important as this voltage determines the electron energy.

The pulsed nature of the diode voltage signal requires any resistive divider monitor to have, for the frequencies of interest, a negligible inductive reactance in comparison with the divider resistance for proper interpretation of the diode voltage signals. In addition, the monitor resistance should be chosen sufficiently large as to make the Joule heating below the rated power dissipation of the resistive column employed. This criteria is emphasised by the desire not to load the circuit being measured so providing larger diode and hence electron beam currents. The use of a resistive divider is illustrated in Fig. (4.1). In this figure V is the unknown voltage to be measured and R_2 is the "tapping" resistor across which the output voltage, V_2, is obtained.

In order to meet the above mentioned requirements a divider was constructed having a total resistance of 5.8 $M\Omega$, with the resistive tap being 50Ω, providing a voltage division ratio of approximately $1:10^5$. This arrangement was built to provide a conveniently manageable signal of $\lesssim 1$ volt from a diode voltage of 100 kV. However, in practice the high resistance of the monitor combined with the capacitance of the various connections extending back towards the

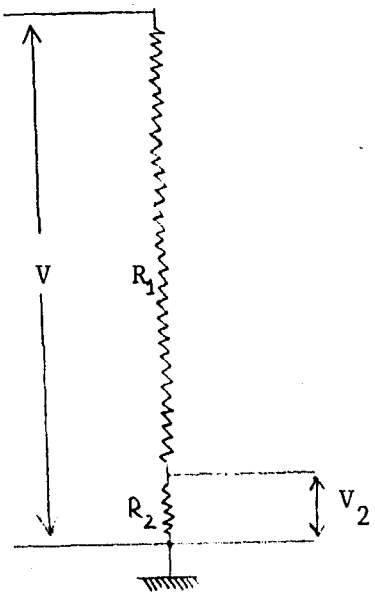

$$V_2 = V \frac{R_2}{R_1 + R_2} \quad ; \quad R_1 >> R_2$$

Fig. 4.1

PRINCIPLE OF HIGH VOLTAGE MEASUREMENT USING A RESISTIVE DIVIDER

Marx bank resulted in unacceptably long rise-times ($\gtrsim 30\,\mu s$) of the signals during tests of the monitor. In an attempt to resolve this problem the monitor resistance was reduced to 100.9 $k\Omega$, however, this still resulted in a rise-time of $\gtrsim 1\,\mu s$ for a 0.2 μs rise-time pulse. Nevertheless, this divider proved useful in calibrating current measuring Rogowski coils (see below) and its construction will, therefore, be described.

4.2.2 Pulsed Voltage Monitor

The high resistance column was made up of seventeen "Welwyn" resistors marked at 5.6 $k\Omega$ and rated at $\gtrsim 1$ watt each. Before constructing the column tests were made on the resistors to check their suitability for,

(i) high voltage handling capability,

(ii) low inductance.

In order to check for their high voltage handling a fast rising ($<2\,\mu s$) 35 kV pulse of 10 μs FWHM was applied to one of the resistors from the secondary terminals of the previously mentioned HML pulse transformer. The input to the transformer was gradually increased by decreasing the value of attenuation, provided by a variable attenuator, between the HML pulse

unit and the primary connections of the transformer, from one shot to the next until there was no remaining attenuation. The resistor survived the test without suffering electrical breakdown or overheating.

The importance of the resistor's inductance to the voltage division ratio was checked by applying a square-wave pulse to one of the Welwyn resistors connected in series with 50 Ω The square-wave pulse rise-time was less than 50 ns and the voltage division between the 50Ω and the monitor resistor was that expected from their d.c. resistance values, within the limits of experimental error (<5%). The voltage across the 50 Ω was measured with an oscilloscope with a 1MΩinput impedance.

The construction of the voltage monitor is shown in Fig. (4.2). The series of resistors were contained in a 7mm i.d. perspex tube whose upper end was threaded to mate to an 18cm diameter hollow copper sphere providing an anti-coronal shield. Although each of the resistors were marked with the same nominal value of resistance some proved to be of higher resistance than others on measurement with a digital ohmmeter and these resistors were inserted at the upper

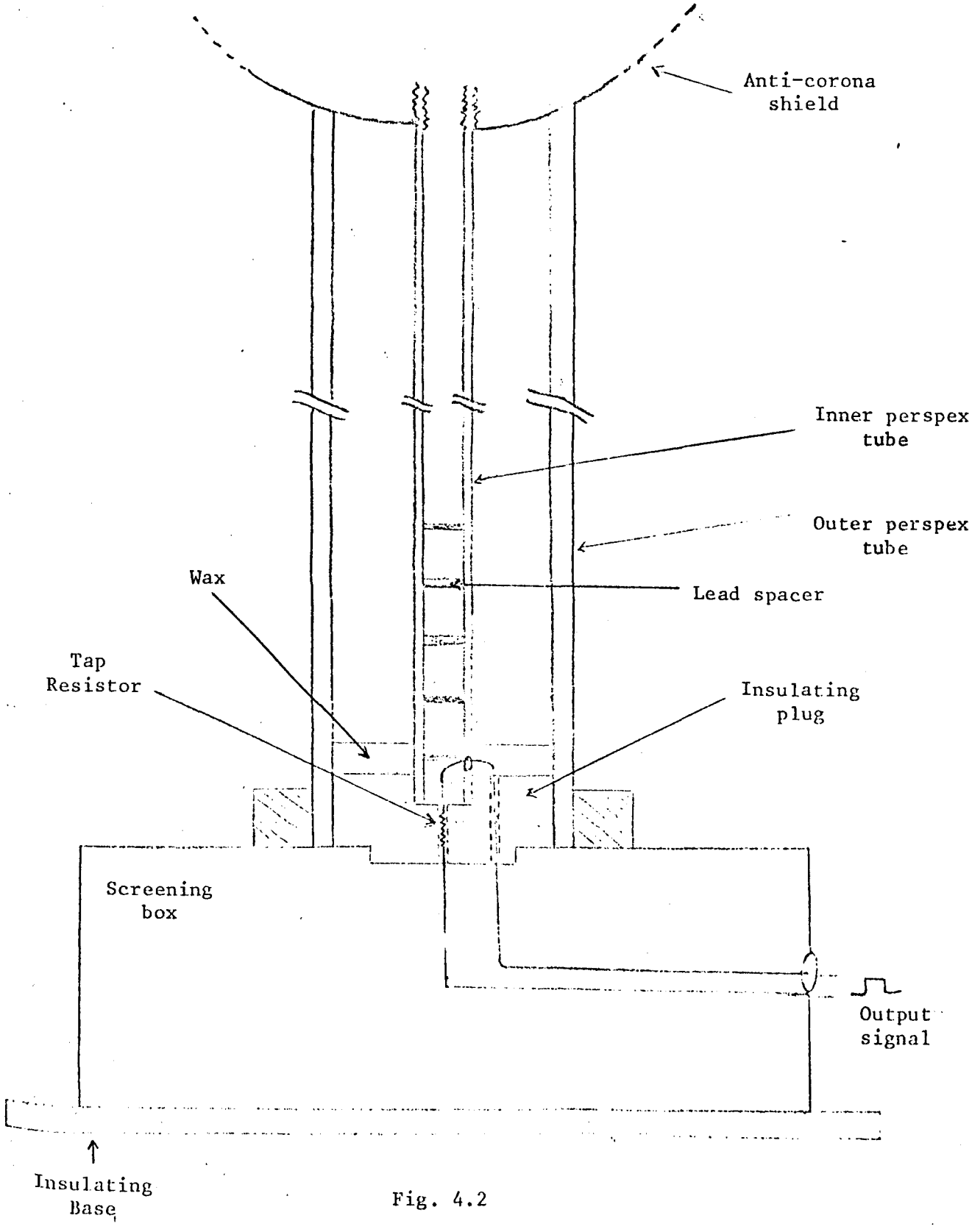

Fig. 4.2

SCHEMATIC OF PULSED VOLTAGE MONITOR

end (high negative voltage) of the column to provide improved voltage grading. The lower end of the resistance chain was terminated with a tap resistor of 51.1Ω , chosen to minimise reflections along the co-axial signal cable and mounted to reduce capacitive effects. The 51.1Ω tapping resistor had its leads taken down into a metal screening box to which was attached a BNC bulkhead socket. The resistor leads were connected to the outer and inner of the BNC connection providing a connection to which a signal cable could be attached and taken back to wherever one wished to record the signal.

It can be seen from Fig. (4.2) that the small diameter lead of the tap resistor protrudes through the inner perspex sheath. This lead represented a sharp point and caused flashover problems with the high voltage end of the monitor. However, this problem was circumvented by pouring molten wax between the two perspex columns and allowing it to harden so forming some insulation around the tap resistor and thus reducing the possibility of electrical breakdown. The outer perspex column was used to support the anti-coronal shield. The individual resistors employed in the column had their wire leads removed and were machined to have flat ends which were interspaced

with small discs of lead metal to provide good contact and to reduce the possibility of arcing between resistors.

The resistive divider had its division ratio checked by applying a d.c. voltage (4kV) across the monitor and observing the expected signal across the tap resistor with a digital multimeter. (In fact the initially observed voltage was lower than that expected but this was merely due to poor contact between the anti-coronal shield and the resistive column.)

A pulsed calibration of the voltage monitor was carried out by applying a 20 volt pulse of rise-time less than 50ns to the monitor whose output was recorded on an oscilloscope with a 50 Ω terminating resistor at the amplifier. The observed signal was roughly half that expected but this was due to the monitor "seeing" the CRO termination as being in parallel with the divider tap resistor, this being checked by removing the 50 Ω termination and observing a signal twice as large (but noisier). Subsequently, the divider was always used with the signal cable terminated in 50 Ω and the calibration of the meter being taken as (0.24 volts/kV $\pm$ 9%). The error is calculated from the error in reading the oscillograms

and from the CRO amplifier errors.

The rise-time of the voltage monitor during the pulsed calibration was less than 0.8 μs. A slight "ringing" on the output signal leading edge was removed by passing the signal through a 0.1 μs RC filter before going into the oscilloscope. This filter produced negligible attenuation of the output signal and only slightly increased the rise-time of the output pulse (plate 4.1). The less serious ringing in the falling edge of the output signal was due to poor earthing arrangements and was removed by disconnecting the earth lead from the CRO mains plug. When in use this monitor was always spatially isolated from nearby objects to prevent breakdown.

Because of the limited frequency response of the above monitor most of the high voltage diode studies were made with a divider of 440Ω resistance and so the tap resistance had to be reduced to 0.477Ω (measured with a high accuracy digital meter) to give safe manageable signals. The resistor chain was made of heavy duty "Morganite" resistors in order to handle the high power. Fortunately, the low resistance of the tap resistor did not result in unacceptable levels of distortion of the cable signals. The resulting voltage

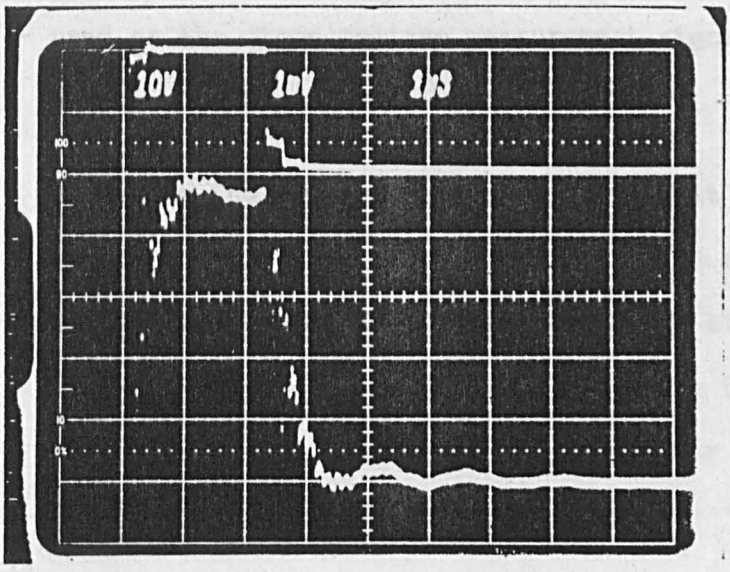

Plate 4.1. Calibration of high resistance voltage monitor.

Top: Pulse from signal generator (10V/div).

Bottom: Signal from tapping resistor (1mV/div).

Time-base at 1µs/div.

division ratio (1.08×10^{-3}) meant that a number of "Tektronix" attenuators had to be used on the diode voltage measurement signal cable.

From the manufacturer's data sheet it was known that the "Morganite" resistors used had a voltage resistance coefficient of 3% per kV/inch and as the resistance column was nominally 55 inches high this gave a potential error of 5% per 100 kV in the resistance division ratio.

4.2.3 Marx Voltage Meter

Measurement of the Marx charging voltage was made by monitoring the voltage of the capacitor nearest earth potential. After this voltage reached a peak level on the meter the bank was left to charge a little longer to ensure that all the capacitors were charged to the same voltage.

Monitoring of the voltage on the one capacitor was frequently made with a commercially available high voltage meter which had a range of (0-30)kV, positive or negative polarity. For higher Marx bank settings a d.c. resistive divider was built which had a range of -100kV to +100kV. Again, the divider was constructed using Welwyn resistors but as the high voltage was d.c. rather than pulsed problems of heat dissipation and voltage breakdown

meant that the resistors had to be of the type that were threaded so that they could be screwed flush against one another and were of sufficiently high resistance (200 M Ω each) to operate within their rated power limit. The overall resistance of the column was then 2 GΩ and its construction was similar to the pulsed divider but had a smaller (10 cm diameter) anti-coronal sphere and was terminated with a (50-0-50) μA movement d.c. current meter of resistance 1370 Ω.

A number of d.c. voltages were applied to the divider and the signal developed across the micro-ammeter was observed on a digital voltmeter. A calibration table of output signal against the applied voltage was plotted. The maximum applied input voltage from the E.H.T. unit was 30kV but the response was linear as expected and was assumed to have the same gradient for higher applied voltages. In addition to observing the output voltage with the digital meter the analogue current meter could be used as a measurement of the applied voltage but this could not be accurately observed from a safe remote standpoint.

4.3.1 Diode Current Diagnostic

As the diode currents were expected to be large ($\geq$ 1kA) a resistive shunt was built of resistance sufficiently low to provide manageably low voltage signals for observation on a CRO. As in the case

of the diode voltage monitor the pulsed nature of the diode current meant that proper interpretation of the shunt signals required a shunt whose inductive reactance, at the signal frequencies of interest, would be negligibly small in comparison to the shunt resistance.

4.3.2 Diode Shunt Construction

In an attempt to satisfy the above mentioned requirements a current shunt was built to the design of figure (4.3). A thin lamina of stainless steel, 0.003 inches (76.2 microns) thick and 2 inches by 12 inches (5cm by 30cm) in area, was soldered between two 12 inch (30 cm) long, $\frac{1}{2}$ inch by 1 inch (1.27 cm by 2.54 cm) brass rods. The stainless steel sheet provided the low resistance (desired to be $\lesssim 2$ m Ω) with the brass end pieces keeping the resistor taut and providing a fixture onto which connections were made. The edges of the brass rods were rounded off to prevent corona discharge problems.

In general, current measurements obtained by taking the ratio of the voltage developed across such low resistance shunts to the resistance of the diagnostic can be in error if the contacts to the shunt are made such that they are likely to be variable (as a result of contamination or wear). To overcome this possibility the shunt resistance was

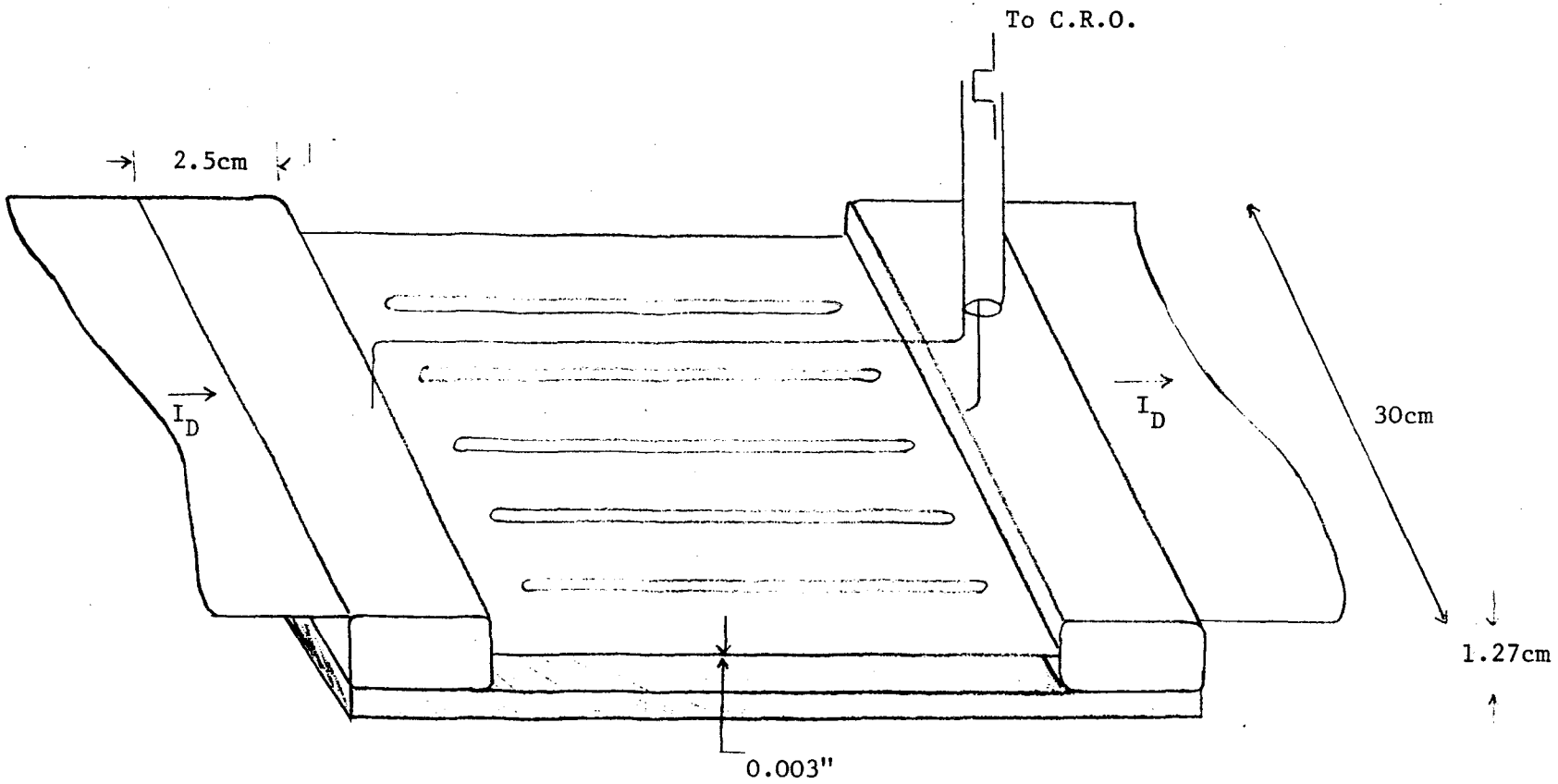

Fig. 4.3

SCHEMATIC OF DIODE CURRENT SHUNT

constructed so as to be of the "four-terminal resistor" variety. A small piece of co-axial cable had its outer conductor bared and soldered to the middle of one of the brass rods and its inner conductor soldered to the middle of the other rod, the connections being made such as to minimise the area of the loop formed by the co-axial cable and the shunt, and therefore the associated inductance. These connections were then expected to provide a constant resistance for the soldered co-ax to brass connections and the shunt resistance could be defined as the ratio of the voltage between the inner and outer of the co-axial cable to the value of the current flowing through the stainless steel lamina.

4.3.3 Operating Frequency Considerations

If the calibration of a current shunt, such as the one discussed above, is to have a value insensitive to frequency it is necessary that the skin depth of the shunt should be large in comparison with the thickness of the shunt for the range of operating frequencies of the current source. Assuming the electrical resistivity , ρ , of the stainless steel to be $1.0 \times 10^{-6}\ \Omega m$ then the skin depth, δ , of the diode current shunt was calculated, using the relation,

$$\delta = \left[\frac{\rho}{\pi f \mu_o}\right]^{\frac{1}{2}} \qquad (4.1)$$

to be 160 μm at a frequency, f, of 10 MHz, a frequency greater than any signal measured. As the shunt was 76 μm thick it was adequately thin for the intended experimental measurement.

In addition to preventing the current from trying to flow in a restricted depth of the lamina the possibility of particularly high currents "pinching" the diode current flow towards the middle of the lamina, and thus changing the effective width of the current carrying channel, was considered. In order to prevent such an occurence thin strips were cut out of the stainless steel along the current carrying direction so forcing the current to flow uniformly across the shunt breadth.

4.3.4 Diode Shunt Calibration

As the shunt had a large ratio of skindepth to thickness it was possible to calibrate the diagnostic with known current sources of frequency less than the frequency of the current that the diagnostic was intended to measure. Two calibrations of the current shunt were made. The first was a low current d.c. test to compare the measured

resistance of the shunt with the calculated value and secondly, a high current measurement was made on the pulsed discharge circuit which was used to provide the magnetic field (Chapter 3).

The measurement of d.c. resistance was carried out by passing a current of 1A, obtained from an accumulator and controlled by a rheostat, through the shunt. The current was monitored with an avometer and the voltage developed across the shunt was observed on a digital multimeter ("Fluke" model 8022). Connections from the acid cell leading current in and out of the stainless steel were made through copper strip lines of breadth equal to the breadth of the brass end rods and screwed down to the brass, and of length greater than the breadth of the lines in order to ensure that current flow along the transmission lines had had enough distance to "spread out" and occupy the full width of the stainless steel. This connecting arrangement was preserved during the pulsed calibration and when the shunt was finally connected to the diode circuit. The result of the measurement on the d.c. circuit gave a value of $(1.6 \pm 0.1)\ m\Omega$ for the shunt resistance. The calculated value of the shunt resistance, based upon the stainless steel dimensions and the above quoted value of electrical resistivity was $2.0\ m\Omega$. The discrepancy between the calculated and measured values may well have been due to the error

in measuring the stainless steel dimensions after machining, a measurement made difficult due to the presence of a 6mm thick insulating board which was fixed to the brass electrodes in order to keep them a set distance apart and to insulate the shunt during use.

A further calibration of the diode current shunt was obtained using the pulsed current of the magnetic field circuit. The circuit was arranged so as to have a rise-time of approximately 80 μs (this being the time from 10% to 90% of peak current level) and the current produced was 320A. Although this rise-time is much longer than that of the Marx circuit the large skin depth of the shunt is such as to make the resistance behave as the d.c. resistance during the electron beam experiments. Current measurement of the discharge was made with Rogowski coil #1 (see later) situated at the earthed end of the magnetic field circuit and independently by a small eight turn magnetic flux probe of 3.81 cm diameter placed inside the solenoidal field coil with its axis aligned parallel to the axis of the solenoidal field coil. The resulting value of shunt resistance obtained from the Rogowski coil was $(1.65 \pm 0.2)\ m\Omega$. The magnetic field probe also gave a favourable value of resistance ($1.69\ m\Omega$) but was considered

to have a larger, and less easily calculated error as the probe position and orientation in the field coil was made visually and therefore the probe was not necessarily centred or aligned correctly inside the coil.

4.3.5 Noise Problems

In order to obtain this agreeable result it was necessary to arrange the earthing connections to prevent unwanted signals. Initial measurements on the shunt were an order or magnitude larger than expected from the d.c. result but had the same profile as the Rogowski coil and pick-up probe signals. The magnetic field circuit was being fired with the electrical spark gap which was connected to the screened room. The current shunt was connected to the "earthy" side of the *RLC* circuit and the signal going back to the screened room meant a second connection to the same earth.

To overcome the inductive pick-up problem the earthed cable, which normally earthed the magnetic field circuit, was disconnected and the mains earth in the EHT unit was removed. In addition the trigger pin cable was disconnected and the circuit fired using the gravity dump. The pick-up problem was reduced in varying degrees by removing the various earths in turn and completely eradicated by removing

all earths other than the screened room. The possibility that the problem had been the result of a faulty cable was checked by measuring the impedance of the cable bringing the shunt signal back to the screened room and by interchanging it with another cable which was known to be sound.

4.4.1 Rogowski Coils

As the currents in the electron beam experiments were rapidly varying a convenient way to measure them was by using Rogowski coils to detect the changing magnetic induction due to the time varying currents. Rogowski coils are basically multiturn toroidal belts in which currents are induced if the belt encircles some time-varying "exciting-current" and their use in measuring the large, time-varying currents typical of neutral and non-neutral, plasma physics experiments is well known [56,58,59].

The technique of using Rogowski belts provides one with a means of making a macroscopic current measurement without the need for a direct connection to the electrical circuit in which the current is flowing. This last point is of advantage when measurements are being made on more than one rapidly varying parameter simultaneously as inductively generated signals between direct connections for separate monitors may produce

noise signals which may result in misinterpretation of data.

Five different Rogowski coils were constructed to meet the different criteria required of separate current measurements and the geometrical configurations of these coils are given in Table (4.1).

Rogowski coils can be employed in either of two modes:

(i) Self-integrating coils in which the output signal voltage is proportional to the current being measured;

(ii) "differentiating" coils in which the output voltage is proportional to the derivative, with respect to time, of the current being measured.

Both modes of operation have their advantage but whichever way one wishes to employ them, each mode of operation presents a set of conflicting requirements necessary for useful operation. Both types of operation were employed in the electron beam experiments and each are discussed below.

4.4.2 Differentiating Rogowski Coils

All five coils wound were used in the magnetic field circuit in the differentiating mode. As the

Rogowski	Area of minor loop cm sq.	mean major radius cm	Number of turns	Calculated Inductance μH
1	2.19	3.25	138	26
5	10.44	5.30	10	0.40
4	10.44	5.30	95	36
3	10.44	5.30	98	38

Geometrical Configuration of Rogowski Belts.

Table 4.1

output voltage from these coils is proportional to the time derivative of the current being measured the signals were separately integrated before being applied to oscilloscopes. The integration was always carried out using a passive "RC" integrator arrangement.

If a Rogowski coil is threaded by a time-varying current, I, then a magnetic flux, ϕ, will be induced in the coil and the circuit equation will be given by [60],

$$\frac{1}{R_T}\frac{d\phi}{dt} = \frac{L}{R_T}\frac{dI_c}{dt} + I_c \qquad (4.2)$$

where I_c is the current flowing in the coil windings, L is the coil self inductance and R_T is the total circuit resistance (including the circuit external to the Rogowski coil). If the coil is designed such that $t_r >> L/R_T$ where t_r is the fastest rise-time of any signal to be measured, then the output voltage of the coil will be proportional to $d\phi/dt$. Figure (4.4) shows the equivalent circuit of such a coil when used with an RC integrator and for times, $t << RC$ the output voltage, v, is given by,

$$V_{out}(t) = \frac{KNI(t)}{RC} \qquad (4.3)$$

where N is the number of turns in the Rogowski belt and K is a constant depending on the geometry of the coil. The approximate

sensitivities of differentiating coils can be calculated assuming,

$$K = \frac{\mu_o(\pi a^2)}{2\pi r} \qquad (4.4)$$

where,

a = the minor mean radius of the coil to the centre of the windings,

r = the major mean radius of the coil.

Note that the d.c. resistance of the Rogowski coil is negligible in comparison with the 50Ω matching impedance, which is shown in fig.(4.4).

The above equations indicate that coil sensitivity may be made desirably large by employing large values of a or N, however, both would tend to increase L and the criteria on L/R_T would be affected. Alternatively, a decrease in the value of RC would improve the sensitivity but this in turn would reduce the valid integration time. As a general rule, an RC constant of fifty times the required integration period is necessary for accurate measurement.

4.4.3 Coil Calibration

The differentiating Rogowski coils were calibrated using the pulsed magnetic field circuit as a known current source. The field circuit, operated with the 300 μF capacitors, had a rise-time

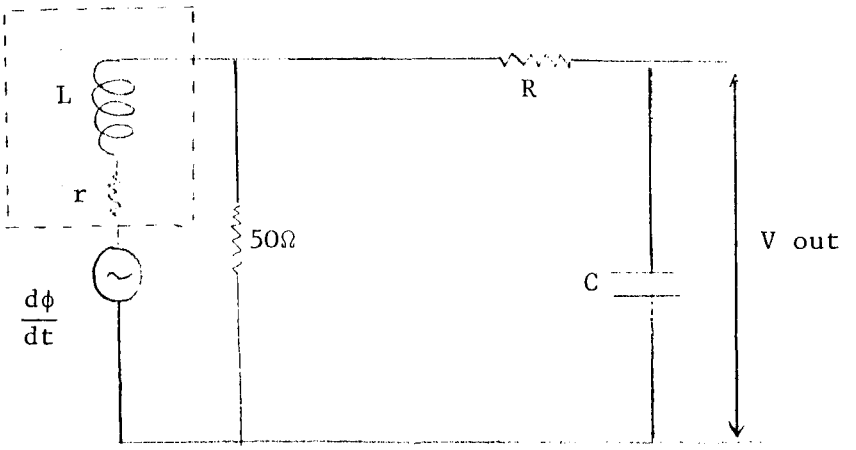

$R >> 50\Omega \gg r$

Fig. 4.4

EQUIVALENT CIRCUIT OF DIFFERENTIATING ROGOWSKI COIL AND ACCOMPANYING PASSIVE INTEGRATOR

of $\simeq$ 1msec which was much greater than the response time of the coils being used in the differentiating mode. This response time is given by L/R as indicated by solutions of the Rogowski circuit equation given by Pellinen et al [60]. During many experiments with Rogowski coils and magnetic pick-up probes a variety of RC integrators were constructed and used and their R and C values are given in Appendix 1.

Only Rogowski # 4 was calibrated against the magnetic field circuit with an appropriately large integrator time (95ms). All the other Rogowski coils were calibrated against Rogowski # 4 with each coil threaded by the circuit having an integrator time $\simeq$ 10ms, however, as both coils had essentially the same integrator constant respective sensitivities could be compared by comparing current signal levels appropriate to a specific time. Comparison of Rogowski coil signals when used with 10ms RC integrators against current measurements from the 1ms rise-time magnetic field circuit, illustrated that the Rogowski coil signals were smaller than expected by the order of five per cent as would be a signal from a square wave current pulse of width T with $T/RC = 0.1$.

Two resistive measurements of the circuit current were made while calibrating Rogowski # 4. The current was measured using the 9.8mΩ shunt as discussed in Chapter 3. However, an additional check was made on the circuit current using the 100.9k Ω resistive divider of section (4.2.2.). The current-shunt-implied current agreed well with the value estimated from the resistive divider column which was connected between the circuit earth and the h.t. end of the solenoidal field coil. This agreement supported the contention that the conducting wire used to wind the coil was of sufficiently small diameter not to exhibit any skin effect during the pulsed discharge. The circuit current inferred from the voltage divider was made by calculating the ratio of the voltage across the divider column to the d.c. resistance of the solenoidal coil.

The resistive divider signal was measured at a time when the shunt voltage signal was a maximum so that no contribution from inductive voltages was present on the divider signal. In order to ensure accurate measurement of the oscilloscope signals the signals were delayed with respect to the trigger signal so that shifting of the base lines from their original settings would not result in false measurements being made.

As the magnetic field profile is quite flat at its maximum, just where to measure the voltage divider signal was quite uncertain, however, as the magnetic field circuit was completely reproducible in behaviour a separate shot with the divider against an un-integrated differentiating Rogowski signal allowed the voltage divider signal to be measured when the Rogowski trace went through zero; this was easily observable. The experimentally determined value of the coil sensitivities are given in Table (4.2).

4.4.4 Self-Integrating Rogowski Coils

As the beam current was much smaller than the Marx current (see Chapter 6) it was desirable that a more sensitive coil was used to measure this parameter. Rogowski # 5 with only ten turns was considered ideal for use as a differentiating coil for the large ($\sim$ 1kA) Marx current with a 100μs integrator giving it a rise-time $\simeq$ 1ns which is sufficiently short to deal with the Marx circuit rise-time ($\simeq$ 200ns). However, the smaller beam current signal required the more sensitive Rogowski # 3 or Rogowski # 4. As the coil inductance is proportional to the square of the number of turns, though, these coils acting in a differentiating mode would

Rogowski	Sensitivity * 10^{-2} mV/A
1	1.7 ± .2
2	5.0 ± .5
3	8 ± 1
4	8.1 ± .6
5	0.83 ± .09

Differentiating Coils

Rogowski	Sensitivity V/kA	
3	14 ± 2	with matching resistor
3	26 ± 3	without matching resistor

Self Integrating Coils

* Normalised for 10 ms integrator

Table 4.2

SENSITIVITIES OF ROGOWSKI COILS USED FOR PULSED CURRENT MEASUREMENTS

have been unsuitable for the fast rising beam current and any attempt to reduce the RC time below 100 μs would have attenuated the beam signals after undesirably short time intervals. Therefore, for the purposes of electron beam current measurements Rogowski # 3 was modified to be a self-integrating Rogowski coil.

Self-integrating Rogowski coils are made with the criteria that $\Delta t << L/R$ where Δt is the width of the pulse being measured. Solution of equation (4.2) then shows that,

$$I_c \simeq \frac{\phi}{L} \qquad (4.5)$$

In this sense self-integrating coils act as current transformers as ϕ is proportional to N, and L is proportional to N^2 so that $I_c \simeq I/N$. To achieve the condition that $\frac{\omega L}{R} >> 1$ the belt is shorted across its major winding with a small "current viewing" resistance, R_{cvR}, compared with which the Rogowski resistance is not necessarily negligible. The sensitivity of the coil is seen to be R_{cvR}/N.

As coils operated in the self-integrating mode produce signals proportional to the flux linking the coil turns rather than the time derivative of this flux, as in the case of differentiating coils, these coils have an

output which is not frequency dependent and which suffers less attenuation along the co-axial cable carrying signals to oscilloscopes. Their useful viewing time or "window-time" is given by L/R as shown by Pellinen [61]. The rise-time of a Rogowski belt employed in the self-integrating mode may be limited by external circuitry but the coil itself will have a rise-time determined only by the transit time of an electromagnetic signal through a single turn of the Rogowski belt as long as the belt is symmetrically excited by the current being measured. The transit time around a single winding is approximated by,[60]

$$T = \frac{1}{c} \left(\varepsilon_r \left(p^2 + 2\pi a^2\right)^{\frac{1}{2}} \right) \qquad (4.6)$$

where, ε_r is the relative permittivity of the material on which the coil is wound, p is the pitch of the windings and is given by $2\pi r/N$ and c is the speed of light. Solution of the above equation for Rogowski # 3 gives a value of approximately 1nsec for the rise-time which was sufficiently short for the intended experimental measurement.

The value of R_{cvR} employed was 3.3Ω which was equal to the belt resistance. On occasion a $48.5\ \Omega$ resistance was placed in series with

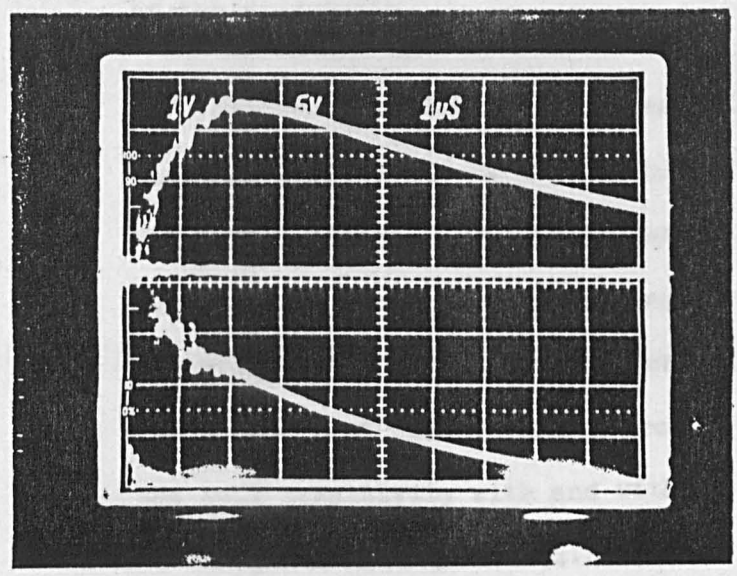

Plate 4.2. Comparison of rise-times between Rogowski #2 and self-integrating Rogowski coil.

Top: Rogowski#2 measuring Marx current (209A/div).

Bottom: Self-integrating Rogowski coil measuring Marx current (357A/div).

1μs/div.

the belt to improve matching with the co-axial cable, an arrangement which halved the sensitivity of the diagnostic.

Calibration of the self-integrating Rogowski coil was carried out by firing the Marx bank into the 440 Ω voltage divider and inferring the Marx current from the voltage developed across the tap resistor. The Rogowski was placed at the earthed end of the Marx circuit and the resulting signal provided the coil sensitivity with and without the 48.5 Ω matching resistor (Table (4.2)).

4.4.5 Rogowski Coil Construction

All coils were wound on PTFE formers and had, therefore, a relative permeability of unity. In order to prevent erroneous signals from any time changing magnetic flux linking the major opening of the toroidal belt the end of the Rogowski winding was brought back through the coil turns to the initial end. This meant that any flux threading the major loop did not thread any portion of the measuring circuit.

The windings of the coil were held in place by smearing them with an epoxy resin to prevent their calibrations from changing with time. When in use the coils were mounted so as to be symmetrically excited by the current being measured. In addition, insulation was used

between the current carrying conductor and the inside of the Rogowski belt to prevent any possible breakdown.

4.5.1 Magnetic Field Measurements

As was discussed in Chapter 3, the axial value of magnetic field in the centre of the solenoidal coil could be calculated from the equation,

$$B_z(t) = \frac{\mu_o N I_1(t)}{l\left[1+\frac{d^2}{l^2}\right]^{\frac{1}{2}}} \qquad (4.7)$$

with the value of I being measured using the cylindrical current shunt or Rogowski coils. The equation (3.8) indicates that the current in the coil is directly proportional to V_o the voltage on the circuit capacitor bank. This fact allowed the magnetic field value for each shot to be inferred from the capacitor voltage if the current for a particular voltage setting was known (assuming the values of R, L and C are kept constant). Therefore, for a given magnetic field circuit the field could be measured simply by noting the E.H.T. setting rather than recording oscillograms for every shot.

In practice the voltage on the capacitors was measured using a voltage divider with the voltage across the tap resistor being measured with a digital multimeter ("Fluke" model 8022). The divider had a moving coil meter (100 μ A F.S.D.) in series with the tap resistor and the total resistance of the column was 50 MΩ (set with a potentiometer). In order to calibrate the divider the voltage across the tap resistor was noted for varying E.H.T. settings. The tap resistance was 10.36kΩ giving a voltage division ratio of 2×10^{-4}.

4.6.1 Microwave Diagnostics

Microwave emission from the interaction between the electron beam and the cavity was detected using commercially available X-band (8.2 GHz - 12.4 GHz) and Ka-band (26.5 GHz - 40 GHz) crystal diode detectors. Due to the limitation on the available magnitude of the applied magnetic field most of the detection was made using the X-band system, but due to the possibility of emission from harmonics of the electron cyclotron frequency some measurements were made with the Ka-band system.

The basic experimental arrangement for microwave detection is illustrated in Fig. (4.5). A microwave receiving horn was placed in front of the opening in the concrete shielding to intercept radiation emerging through the glass end plate fastened to the QVF drift tube. The radiation, having entered the horn, passed down a length of waveguide before impinging on a microwave crystal diode. The crystal diode was housed in an ordinary waveguide to co-axial transition allowing the detected signals to pass down co-axial cable and be taken to an oscilloscope in the screened room area.

Processing of the X-band and Ka-band radiation signals were slightly different from

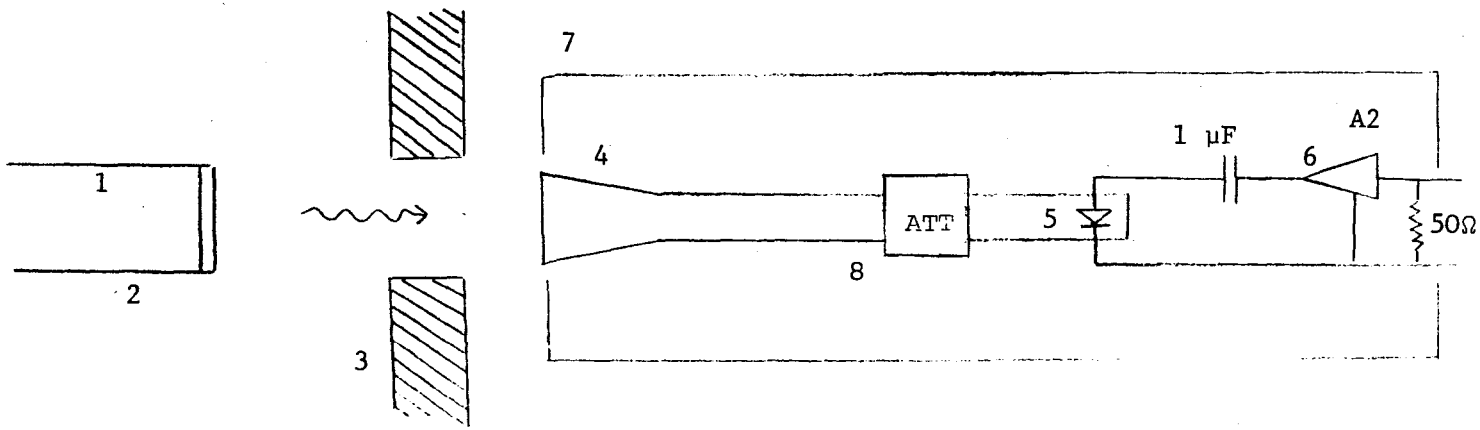

1 Evacuated drift tube
2 Glass end plate
3 Concrete shielding
4 Microwave receiving horn
5 Crystal diode
6 Amplifier (A2)
7 Screening enclosure
8 Variable attenuation (0-60)dB

Fig. 4.5

SCHEMATIC OF MICROWAVE POWER RECEIVING ARRANGEMENT

each other and both will now be considered in turn.

4.6.2 X-Band Detection

In order to check on the response time of the X-band diode a rectangular train of pulses obtained from a klystron unit was passed down a length of waveguide and out through an X-band transmitting horn and then into the detection system. The klystron modulation was set at 1 kHz. The resulting signal from the crystal diode was applied to the input of the CRO placed first locally to the waveguide apparatus and then with the CRO placed back in the screened room area. The rise-time of the output signal with the latter arrangement was found to be much longer than that of the former which was sufficiently short ($\lesssim$300 ns) for measurement purposes. It was suspected that the output impedance of the microwave diode was so high as to limit the charging time of the length of co-axial cable going back to the screened room. In order to improve the detection rise-time without damaging the diode with excessively high currents an impedance transforming amplifier was built so as to maintain the high impedance seen at the crystal diode output but to which a 50Ω termination could be attached at the beginning

of the microwave signal cable. The equivalent circuit for microwave measurements is shown in Fig. (4.6). The cable going back to the screened room was again terminated in 50 Ω to achieve proper matching. The amplifier circuit is shown in Fig. (4.7). Its characteristic was measured by applying a signal from a signal generator and observing the input and output levels. The saturation level of the amplifier can be seen from Fig. (4.8) to occur for an output voltage of approximately 1.2 volts.

It was observed that the amplifier output did not always increase with increasing microwave input power from the Klystron to the microwave diode. Input power to the diode was continuously monitored during this observation to exclude the possibility of variation in the klystron output power. As the amplifier characteristic curve showed that output increased with increasing input it seemed that the amplfier was biasing the crystal diode. In order to decouple the diode from the amplifier a 1 μF capacitor was connected between them. For the fast microwave pulses being detected (see Chapter Six) the effect of the decoupling capacitor on the amplifier characteristic was negligible.

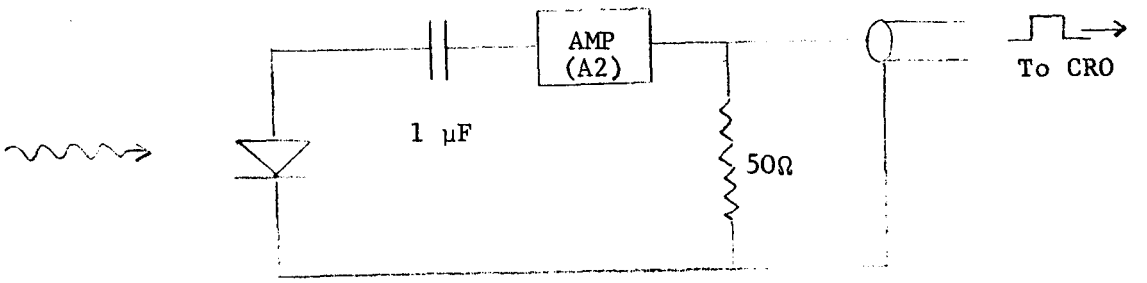

Fig. 4.6

EQUIVALENT CIRCUIT FOR MICROWAVE POWER MEASUREMENTS

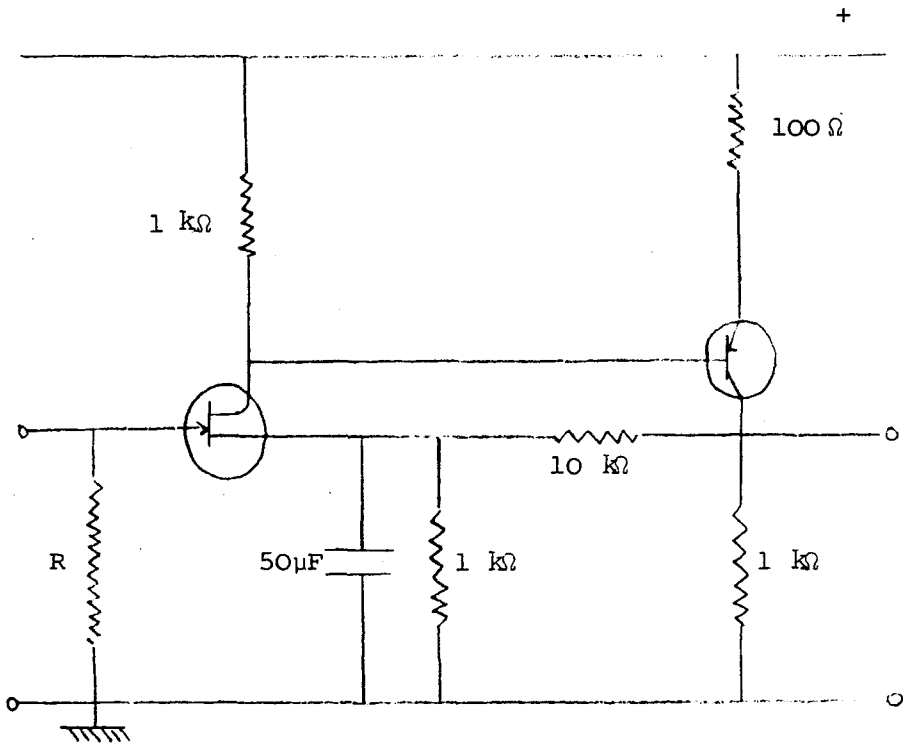

R = 1 MΩ FOR X-BAND SIGNALS

R = 1 KΩ FOR Ka-BAND SIGNALS

AMPLIFIER (A2) EMPLOYED FOR IMPEDANCE TRANSFORMING OF MICROWAVE DETECTOR SIGNALS WHILE MAKING MICROWAVE MEASUREMENTS

Fig. 4.7

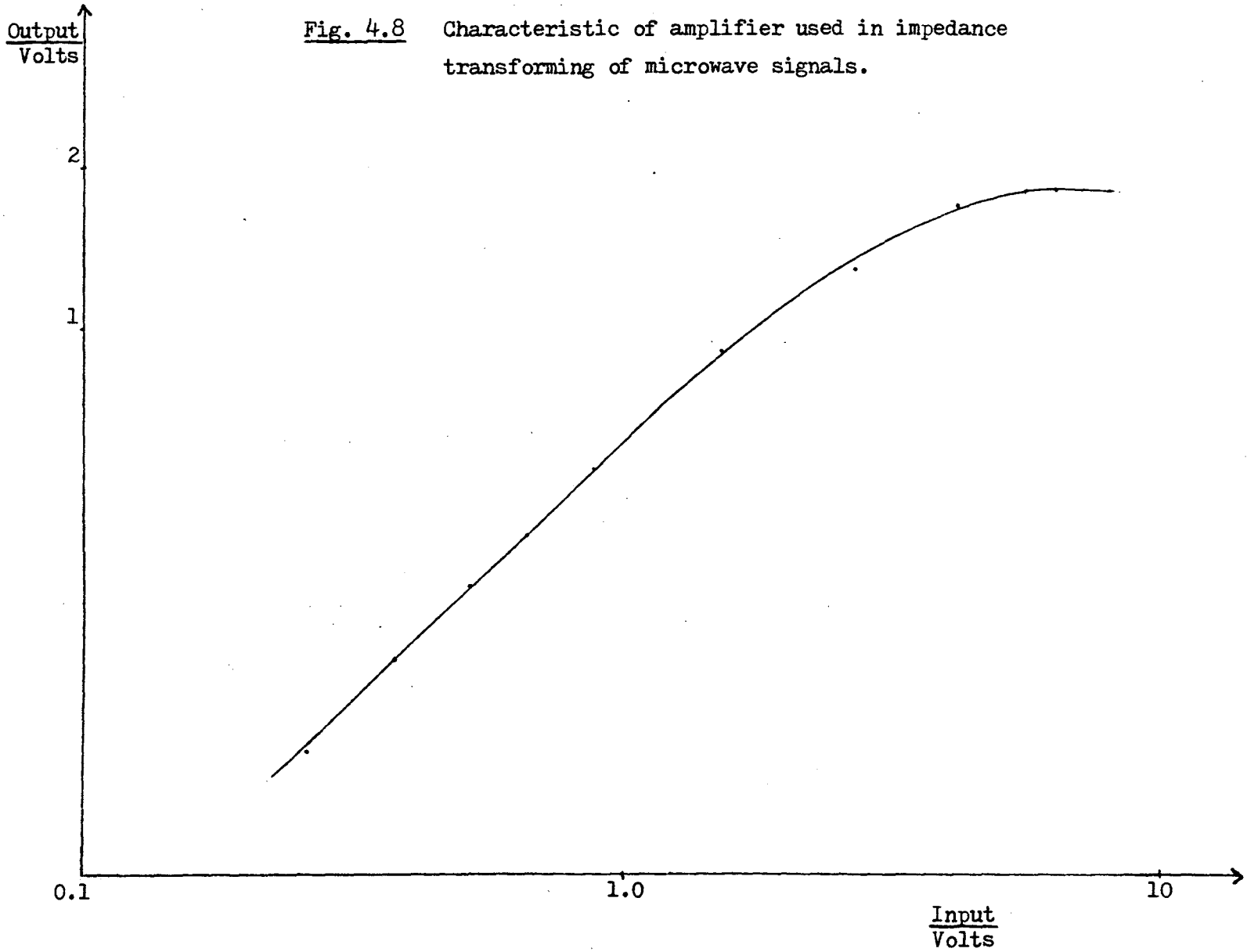

Fig. 4.8 Characteristic of amplifier used in impedance transforming of microwave signals.

In order to accommodate the high output power signals observed at "resonant" magnetic field values during the e-beam-cavity interaction (Chapter Six), two microwave attenuators were employed in the waveguide section between the receiving horn and the crystal diode detector, a distance of approximately thirty centimetres. The attenuators were commercial "Sanders" type VA16 and type CA 16/2, sliding vane attenuators. The type VA16 attenuator had notches indicating the 10dB and 20dB attenuation levels, however, this attenuator could only be used for rough setting as the sliding marker was as wide as the notches themselves and, therefore, accurate reproducible setting of this attenuator was unreliable.

The type CA16/2 attenuator had a thumbdriven micrometer movement allowing accurate resetting of the attenuating vane to within 0.005 mm. This attenuator was supplied with a manufacturer's calibration table giving the required setting for a desired level of attenuation in the range (0-40)dB. This table illustrated that for any frequency interval within the X-band region the required setting for a specific attenuation level was much the same. In order to check that the CA16/2 attenuation calibration had not changed with age it was re-calibrated against the VA16 attenuator.

This was done by observing the distance through which the micrometer had to be screwed in order to produce the same amount of attenuation as the 10dB and 20dB levels of the VA16 attenuator, and a calibration chart was drawn.

While making this calibration the percentage change in the microwave diode voltage output was seen to be dependent on the level of incident radiation power in a fashion which suggested the crystal diode response was changing from "square-law" to "linear-law" with increasing input power, i.e. the output voltage was proportional to incident power for sufficiently low incident power levels and was proportional to incident voltage for sufficiently high incident levels.

The possibility that the change in the form of the diode response was due to changes in the level of the microwave source output power due to back reflections from the changing attenuator vane positions was excluded for the following two reasons:-

(1) The klystron was effectively isolated from back reflections due to the inclusion of a padding attenuator placed between the source and the measurement system.

(2) The signal level incident on the diode was monitored by sampling a fraction of it with a 40dB cross-guide coupler and was not seen to vary during the calibration.

The radiation detection apparatus was enclosed in a metal box to provide screening from electromagnetic noise. A rather makeshift enclosure was used initially but the resulting high noise level (≃200mV), which appeared to be coming down the outside of the signal cables, coupled with the low saturation level of the amplfier meant that improved screening was desirable so that more sensitive measurements could be made. To this end an improved metal enclosure was built with holes cut in it only for the purpose of allowing the radiation to enter the screened box and to allow a signal cable to leave it. The entry hole was cut to the dimensions of the X-band receiving aperture and a metal plate, which could reduce the dimensions of the hole to those of the X-band waveguide, could be screwed against the enclosure.

While making measurements the receiving horn was placed close to, but not touching, the aperture. The co-axial signal cable was taken through a small hole in the side of the enclosure.

This hole had a second outer conducting cable connected to the earth of the system.

The microwave signal cable was wound around ferrite blocks to further reduce noise levels. The resulting noise signal with this screening arrangement was a trace $\lesssim$ 50mV peak to peak.

4.6.3 Ka-Band Detection

Ka-band measurements were made with essentially the same diagnostic arrangement. However, due to the use of the Ka-band crystal diode it was found necessary to alter the input resistance of the amplifier from 1M Ω to 1k Ω The effect of this alteration was to reduce the linear gain of the system by a factor of 0.67.

4.6.4 Polarisation Analysers

Elementary polarisation measurements were made possible using a conducting rod screen to eliminate radiation whose electric field vector ran parallel to the length of the conducting rods. The screen had 22 cylindrical rods nominally three millimetres in diameter. The spacing between the rods was (9.0 $\pm$ 0.5) millimetres and the screen was approximately (19 x 18) cm^2 in area. The screen was mounted in a circular frame which allowed the analyser to be rotated through any desired angle.

4.6.5 Microwave Power Measurements

As the microwave diode sensitivity was not known, and no source of calibrated X-band radiation was available, precise measurements of cyclotron maser power were not possible. At best only an "order of magnitude" calculation could be made of the absolute power emitted during electron beam magnetic field interactions. In order to make an estimate of the emitted radiation power the diagnostic arrangement discussed in (4.6.2.) was used in conjunction with the klystron mentioned above and a detector diode similar to the one used in making X-band measurements.

In order to estimate the attenuating effect of the distance between the stainless steel collector and the X-band receiving horn, a distance of 1.65m, the diode output was measured first with the klystron transmitting horn close to the receiver and then with the transmitting horn placed inside the collector at a distance of 1.65m from the receiver. The diode response was "square-law" (in the sense discussed in section 4.6.2.) for the power levels used in this test and therefore the ratio of the detector output voltages provided an estimate of the forward loss as a result of the source to receiver separation.

The klystron peak power output was believed to be 40 milliwatts (manufacturer's data). Crystal diode voltages recorded during the maser experiments provided an estimate of the power incident on the crystal relative to 40 milliwatts (16dBm).

It is stressed that this "calibration" of microwave power is, at best, only an estimate. The effects of mode conversion at the receiving horn, the effect of the solid angle subtended between the r.f. source and the receiving horn and the output level of the klystron all limit the absolute estimate of the microwave power measurements.

5.1.1 Introduction

Before looking for μ-wave emission from the interaction of the electron beam with the magnetic field the Marx voltage pulse was applied to the cold cathode in the absence of the pulsed magnetic field. This was done in order to gain some familiarity with the diode voltage behaviour and pulse width, and to observe the behaviour and magnitude of the drift chamber electron beam current. Such preliminary studies with varying initial anode-cathode spacings permitted selection of a suitable operating condition for the cyclotron maser experiments, to be discussed in the following chapter.

5.1.2 Explosive Electron Emission

As was mentioned briefly in Chapter One a fundamental concept in the production of relativistic high current beams in vacuum diodes is the phenomena of explosive electron emission. Present understanding of this phenomena suggests that it occurs as a result of an enhancement of the average macroscopic electric field (typically 100kV/cm in the experiments to be discussed here) in the diode due to the presence of microscopic protrusions or "whiskers" which exist on the cathode surface. The large, local microscopic electric fields initiate field emission currents from the material imperfections resulting in their rapid resistive

heating and subsequent explosion forming a metal vapour which diffuses into the surrounding vacuum space. The electron current then ionises the vapour producing a plasma at the cathode surface whose expansion in the diode results in a time changing effective diode gap separation. This so called "cathode flare plasma" diffuses into the diode region with a thermal expansion velocity, characteristic of the emitter material and typically 2cm/μs. As the surface density of these microscopic projections can be expected to be large and uniform the cathode surface in such diodes is rapidly covered with a layer of this expanding plasma.[7] Experimental observations have also been made of an anode plasma formed as a result of electron beam energy deposition on the anode surface.[8]

The notion of the "whisker" theory in explaining the formation of the cathode plasma is exploited in REB diodes in which needle-point emitters are employed as the cathode surface[62].

5.2.1 Temporal Behaviour of Circuit Parameters

As a result of the time-changing anode-cathode gap separation the impedance of the diode also varies with time and, as a result of this, the typical diode voltage, diode current and Marx current traces can be explained by considering the discharge of the Marx bank into the vacuum diode as the discharge of a capacitor through a time

dependent load. The temporal behaviour of the aforementioned diagnostic traces is determined by the impedance collapse of the diode as the vacuum current builds up.

On Marx trigger command the Marx current and diode voltage rise with the characteristic rise time ($\lesssim$ 200 nanoseconds). With no diode breakdown one might expect the diode voltage to reach a voltage given by the series division ratio set by the current limiting series resistor, R_s, and the diode voltage monitor resistance, R_m, i.e. the diode voltage, V_D, would reach its "open-circuit" value, V_{oc},

$$V_{oc}(t) = V_m(t) \frac{R_m}{R_s + R_m} \qquad (5.1)$$

However, due to the rise of the diode current the voltage across the A-K gap suffers an ohmic drop as the diode impedance begins to fall as a result of the cathode's expanding plasma. After the diode has started to break down the diode voltage will be given by the relation,

$$V_D = V_m(t) - I_M(t) R_s = V_m \left[1 - \frac{R_s}{R_s + \frac{Z_D(t) R_m}{Z_D(t) + R_m}} \right] \qquad (5.2),$$

where $Z_D(t)$ is the time dependent diode impedance, showing clearly that the decreasing diode impedance will result in decreasing diode voltage.

For a given initial A-K gap setting a particular value of diode voltage should be necessary to initiate field emission current but it can be seen from plate (5.1) and plate (5.2) that the peak achieved diode voltage for a given gap setting can be increased slightly with a sufficiently large increase in the Marx charging voltage. As presumably the A-K gap always breaks down at some threshold field the increase in diode voltage is thought to be due to the continual discharge of the Marx into the diode.

The Marx circuit current trace begins with the rise of the diode voltage signal and continues to increase in value after the diode voltage starts to fall off, this increasing current being due to the overall decrease of the resistance external to the Marx bank capacitors and despite the fact that the Marx bank charge is decreasing. The Marx circuit current continues to increase in value until around the time at which the diode is electrically shorted indicated by zero diode voltage, at which time as the Marx voltage is falling off and the resistance external to the Marx bank has reached its lowest value, the current begins to decay in the familiar resistor-capacitor discharge manner.

On some shots it was clear that the Marx current signal had started to decrease while there was still some small potential difference across the A-K gap and it is reasonable to assume that this occurred as the rate of

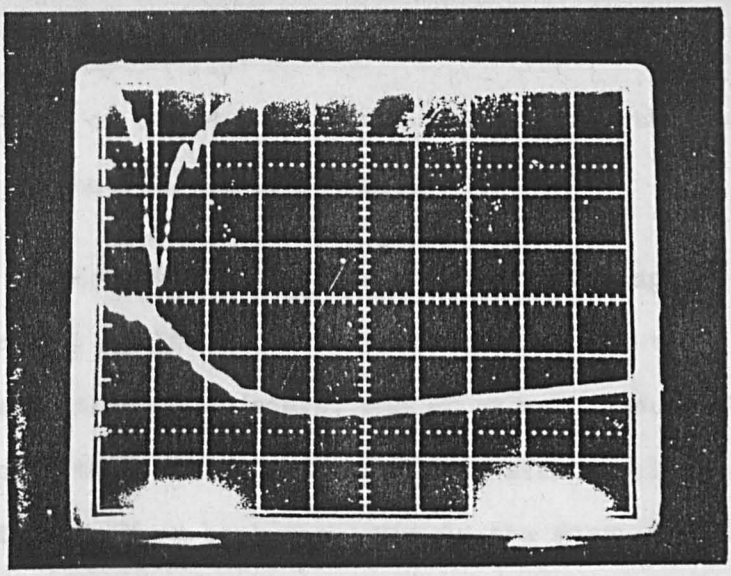

Plate 5.1. Top: Diode voltage profile (23.2kV/div).

Bottom: Marx current trace (630A/div).

Time-base - 200ns/div. Marx voltage setting = 167kV, R_S = 102.5Ω, A-K gap spacing = 7.5 mm.

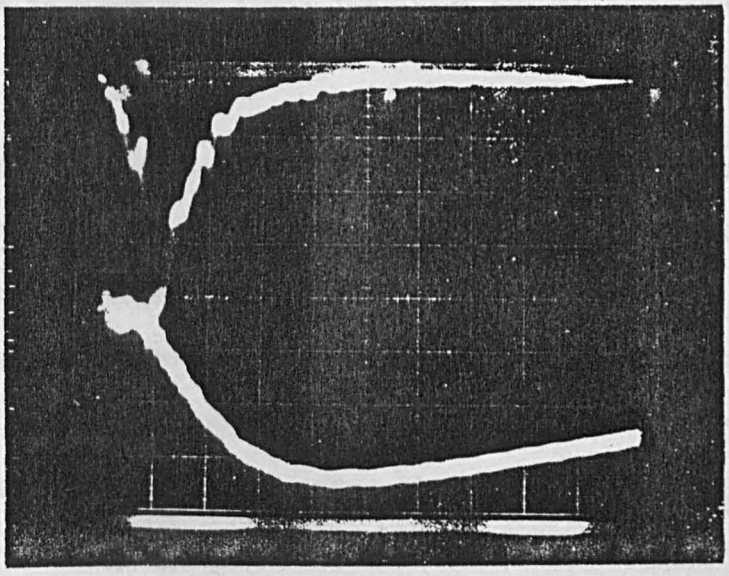

Plate 5.2 Top: Diode voltage trace (23.2kV/div).

Bottom: Marx current trace (630A/div).
t.b. - 200ns/div.

Marx voltage setting - 227kV, R_S = 102.5Ω
A-K gap spacing = 7.5 mm.

voltage decay on the Marx bank was greater than the rate of decrease of the external impedance.

The electron beam and diode current traces appear simultaneously. The diode current increases as the impedance of the diode decays, and after gap closure the diode shorts the voltage monitor and is effectively in series with the Marx bank resulting in the Marx and diode current traces having the same profile.

Before the short circuiting of the vacuum diode the diode current and Marx current would be expected to differ by the magnitude of the current flowing down the voltage monitor and it is clear, for reasons to be discussed later, that there is something irregular about the diode current trace.

The possibility that any contribution to the diode current shunt signal was due to displacement current was excluded on the basis of a calculation of the diode capacitance, and considering the fastest change in diode voltage. An upper limit to the diode displacement current, i_D, was estimated using the expression,

$$i_D \simeq C_D \frac{\Delta V_D}{\Delta t} \qquad (5.3)$$

with C_D, the diode capacitance assumed to be 70pF. Equation (5.3) indicates that displacement currents would have been too small to produce any noticeable deflection

on the CRO for the amplifier settings required to measure the anticipated diode currents.

5.2.2 Electron Beam Signal

The appearance of the electron beam trace was simultaneous with the start of decreasing diode voltage. The direction and magnitude of the trace seen on typical electron beam current signals was checked for validity by placing the Rogowski belt used for beam measurements at the earthed end of the Marx circuit and observing that the conventional current flow direction of the Marx circuit produced a CRO trace in the opposite direction to that produced by the e-beam current. The observed signal then, being in the direction expected from a flow of negative charge, had its magnitude checked by reversing the direction in which the e-beam return current cable threaded the Rogowski belt. The resulting observed signal appeared to be of the same magnitude, as far as was discernible, but of the opposite sign, indicating that electromagnetic pick-up on the e-beam signal diagnostic was negligible. The possibility that the Rogowski signal was due to an ion beam flowing from the collector to the cathode was excluded on the grounds that there was no obvious ion current source.

Observation of the beam-current signal for long times after the A-K gap closure illustrated that after the main pulse of relativistic electrons a large beam signal was observed. This signal was probably due to the diode plasma seeping through the anode mesh producing a high current, low energy beam. This low voltage current was of no interest for the electron cyclotron maser work.

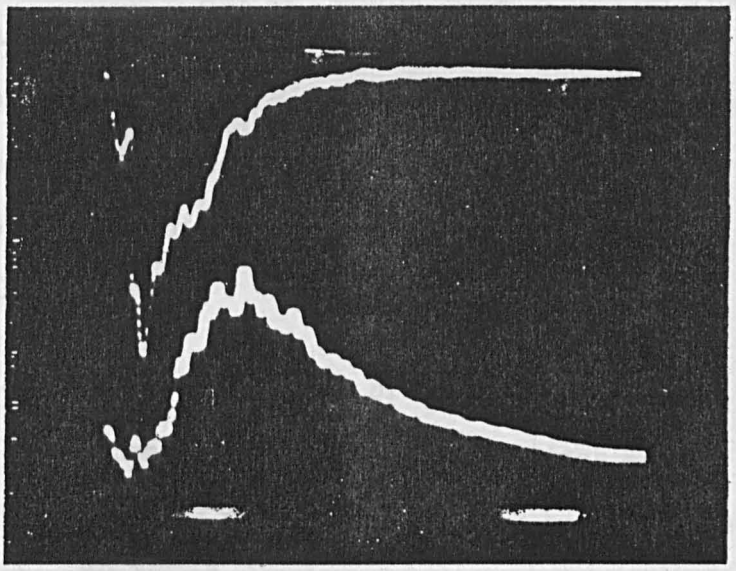

Plate 5.3. Bottom trace shows typical electron beam profile (19A/div).

Top trace is diode voltage (23.2kV/div).

Marx voltage setting at 225kV. Gap spacing is 15 mm.

Time-base at 200ns/div.

5.3.1 Diode Voltage Reproducibility

If any sensible analysis is to be made of the microwave output obtained by injection of the relativistic beam into the magnetised vacuum drift region it is desirable that the diode voltage be predictable and reproducible.

The electrical performance of the diode was observed at a number of different gap settings and Marx voltage settings with each Marx bank series resistor (see Chapter Two) employed in turn. Table (5.1) shows the different operating conditions which were employed most frequently for each of the series resistors. The values of Marx voltage setting for $R_s = 102.5\Omega$ were chosen to give the same open-circuit diode voltage as the corresponding Marx voltage setting with $R_s = 241^{\Omega}$. Initially only three Marx voltage settings were employed at $R_s = 102.5\Omega$ as the lower Marx setting failed to switch the Marx bank spark gaps reliably. Although reliable operation of the Marx bank could have been carried out if some mechanical adjustment to the spark gaps had been made, this same adjustment would have required continual alterations to the gaps to hold off the higher Marx settings of interest. As this mechanical adjustment could not be made as quickly as the spark gap pressure adjustment alterations of this kind would have resulted in slow data acquisition.

Gap Spacing mm	Marx Voltage (kV)			
7.5	160	210	250	285
15	160	210	250	285
30	160	210	250	285
50	160	210	250	285

$R_s = 241\Omega$

Gap Spacing mm	Marx Voltage (kV)			
7.5		167	200	227
15		167	200	227
30		167	200	227
50			200	227

$R_s = 102.5\Omega$

Table 5.1

CONDITIONS UNDER WHICH THE DIODE WAS INVESTIGATED

The diode voltage was usually reproducible with only fine detail on the signal profile varying from shot to shot. However, there were some shots in which the diode signal was significantly different from the norm, particularly at A-K gap settings of fifty millimetres. The overlaying of three diode voltage shots on one oscillogram illustrates the reproducibility of the trace at a gap separation of 3cm, (plate 5.4). At 5cm, however, the diode breakdown behaviour was seen to vary from shot to shot. Figure (5.1) shows the variation of peak diode voltage achieved as a function of initial A-K gap setting with the open-circuit diode voltage as a parameter. This variation is shown for both of the above mentioned series resistors employed in the pulsed circuit.

An obvious result is that the required voltage to initiate breakdown increases with increasing A-K separation.

The first shots at 5cm were with the lowest open-circuit voltage and the diode breakdown profile was similar to that of other gap settings. However, subsequent shots at g = 50mm and higher Marx voltages frequently behaved differently in temporal development. Plate (5.5) shows the diode voltage staying constant at its peak value for times varying from 0.5 μs to 1.2 μs before beginning to decrease. It was noted that the appearance of beam current is synchronous with the beginning of diode voltage decay indicating that this is indeed the time at which the diode had begun to break down.

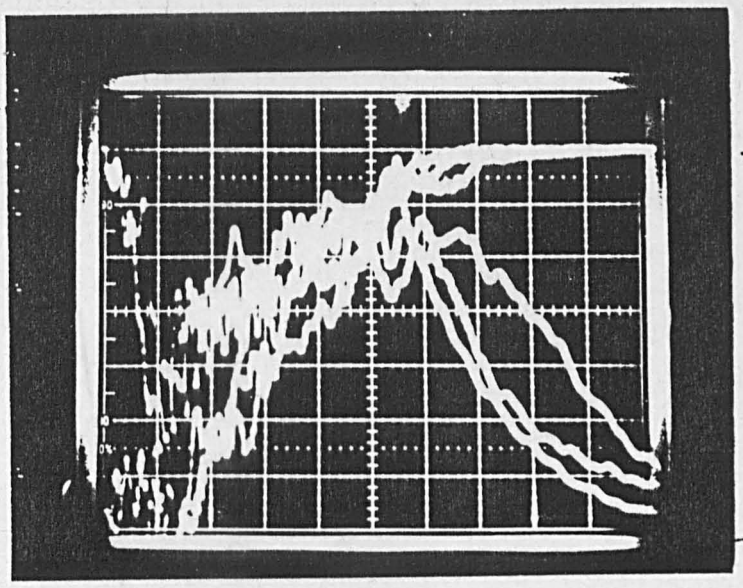

Plate 5.4 The reproducibility of the diode voltage behaviour is illustrated with the "overlay" of three diode voltage shots.

Gap spacing was 3 cm. Marx voltage setting at 210 kV. $R_S = 241\Omega$.

FIG. 5.1(a)

PEAK ACHIEVED DIODE VOLTAGE (V_p) AS A FUNCTION OF GAP SPACING WITH OPEN-CIRCUIT DIODE VOLTAGE (V_{oc}) AS A PARAMETER.
$R_s = 102.5\Omega$

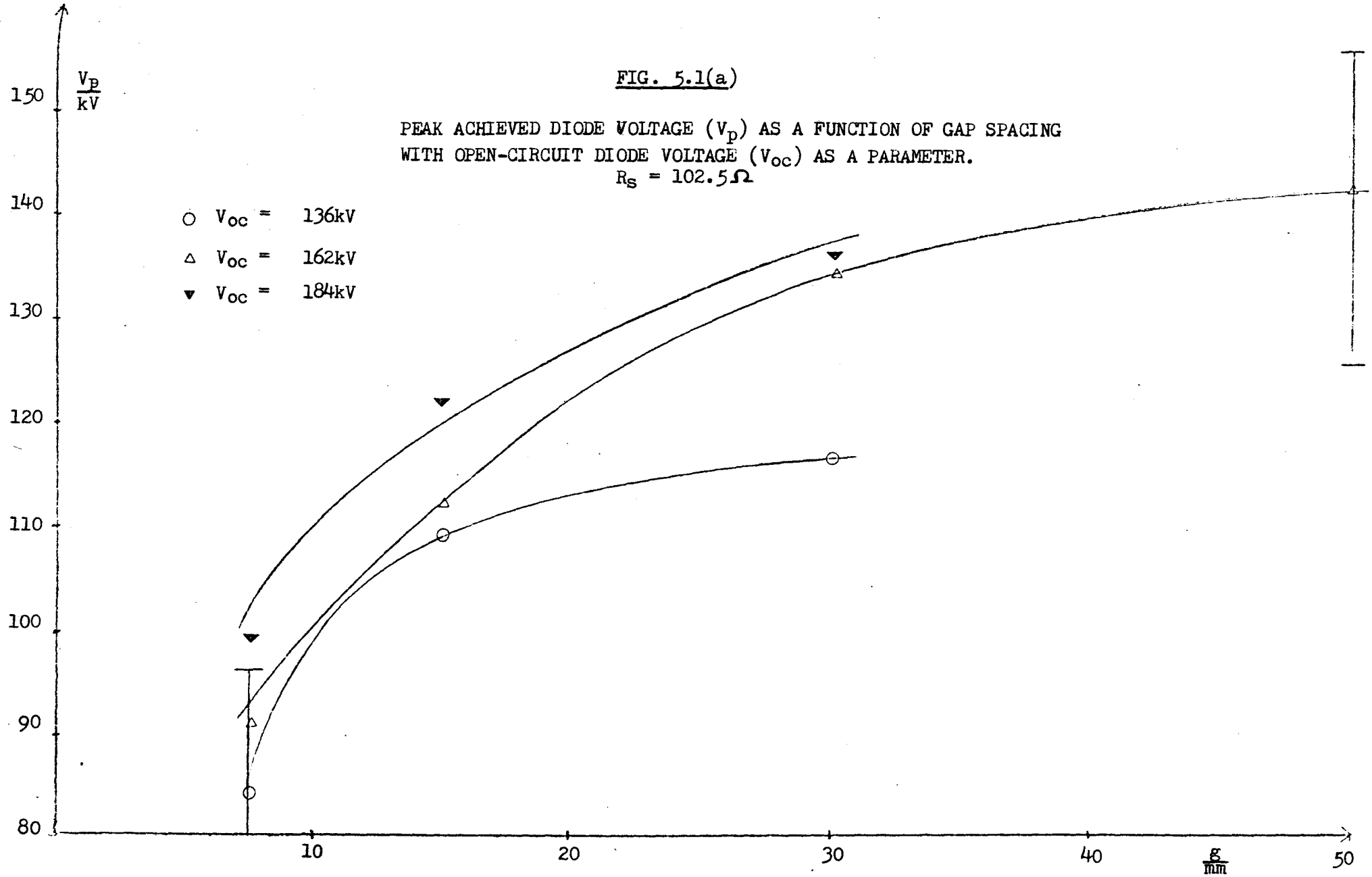

FIG. 5.1(b)

PEAK ACHIEVED DIODE VOLTAGE (V_D) AS A FUNCTION OF GAP SPACING WITH OPEN-CIRCUIT DIODE VOLTAGE (V_{oc}) AS A PARAMETER.

$R_S = 241\,\Omega$

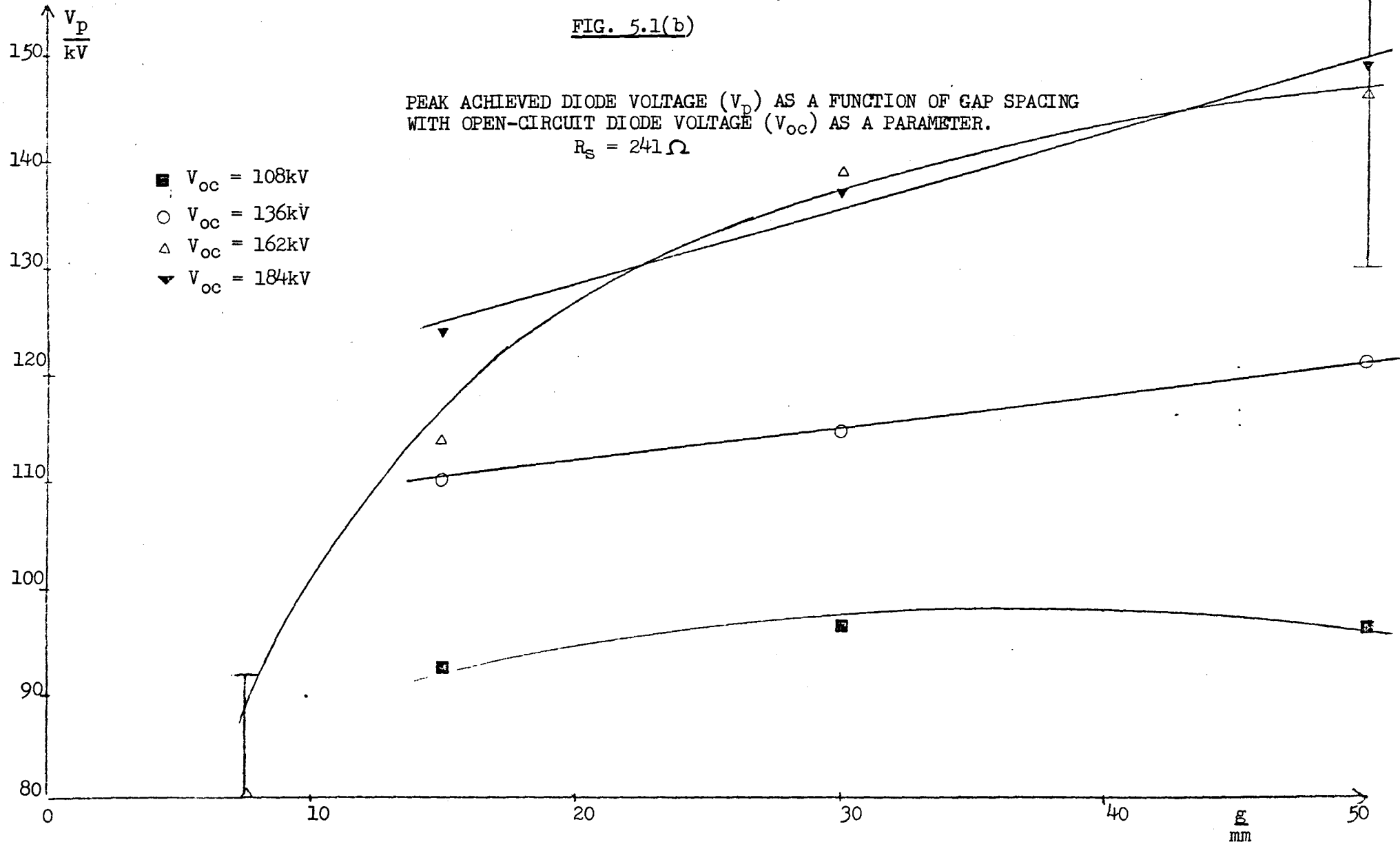

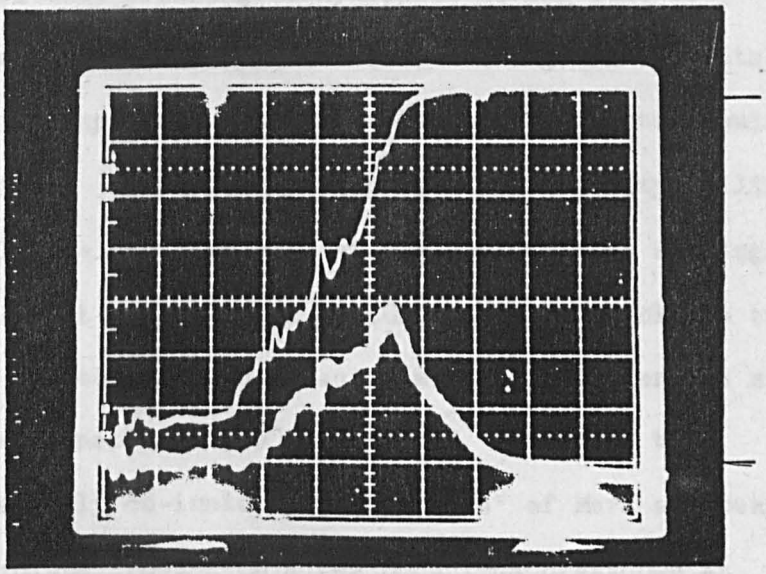

Plate 5.5. The top trace shows the diode voltage staying at a peak value for 1.5μs. for a gap setting of 5 cm.

Time-base at 500ns/cm.

Marx voltage setting was 200kV.

The bottom trace is the electron beam current.

The fact that the diode could sustain such a large voltage without breaking down, despite having done so before, may have been the result of a change in the cathode surface, perhaps as a result of the large currents flowing in the diode. Breakdown at gap settings of fifty millimetres was unreliable and irregular at the Marx voltage settings employed. At gap settings of 50mm, the diode voltage trace, normally monotonically decreasing with time (after the start of the impedance collapse), contained "holes" in the trace seemingly co-incident with "blips" of Marx and beam current (plate 5.6). On a few occasions breakdown at 50mm could not be achieved at all and sometimes occurred in a fashion detrimental to the diode (as was evidenced by an increase in the diode pressure).

The choice of initial A-K gap setting for the microwave production experiment was a compromise between sufficiently long diode pulse width and reliable diode breakdown. For this reason the choice of initial A-K setting was 30mm.

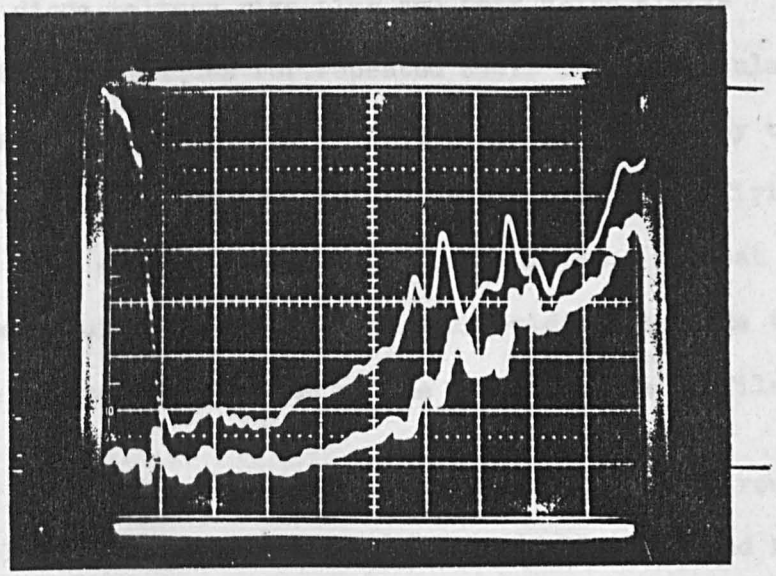

Plate 5.6. Top signal is the diode voltage (23.2kV/div) trace staying constant for 0.5μs for a gap spacing of 5 cm. Bottom trace is the electron beam trace (19A/div).

Simultaneous "blips" in both traces are evident.

Marx voltage setting at 200kV. Time-base at 200ns/div.

Series resistance = 102.5Ω.

5.3.2 Diode Voltage Pulse-Width

The diode voltage rise-time and peak value always assumed the same values for repeated shots at a particular operating condition. A greater variation was shown by the diode voltage pulse-width, that is, the time between firing the Marx bank and the diode impedance collapse. Repeat measurements of the diode voltage pulse-width were made to indicate the reproducibility of the diode voltage profile.

For each different A-K gap separation and open-circuit diode voltage repeat measurements of the full width and full width half-maximum pulse duration were made and a plot of the range of obtained values is shown in Fig. (5.2) and Fig. (5.3), as a function of initial A-K gap separation.

The scatter of values obtained for the pulse width can be seen to be small (less than twenty per cent variation) with the exception of g = 50mm where, as has been discussed above, the diode behaviour was less predicatable. It appears from the data that the full pulse width duration is more reproducible than the FWHM duration.

One might expect the slope of the curve of Fig. (5.2) to be an indication of the flare plasma expansion velocity. This velocity is given by Toepfer[6] as V_E, where,

$$V_E = \left[\frac{4\gamma}{\gamma-1}\right]^{\frac{1}{2}} S\kappa^{\frac{1}{2}} \qquad (5.4),$$

FIG. 5.2

Gap closure time (t_c) as a function of gap spacing and for varying Marx voltage settings. (R_s = 102.5Ω)

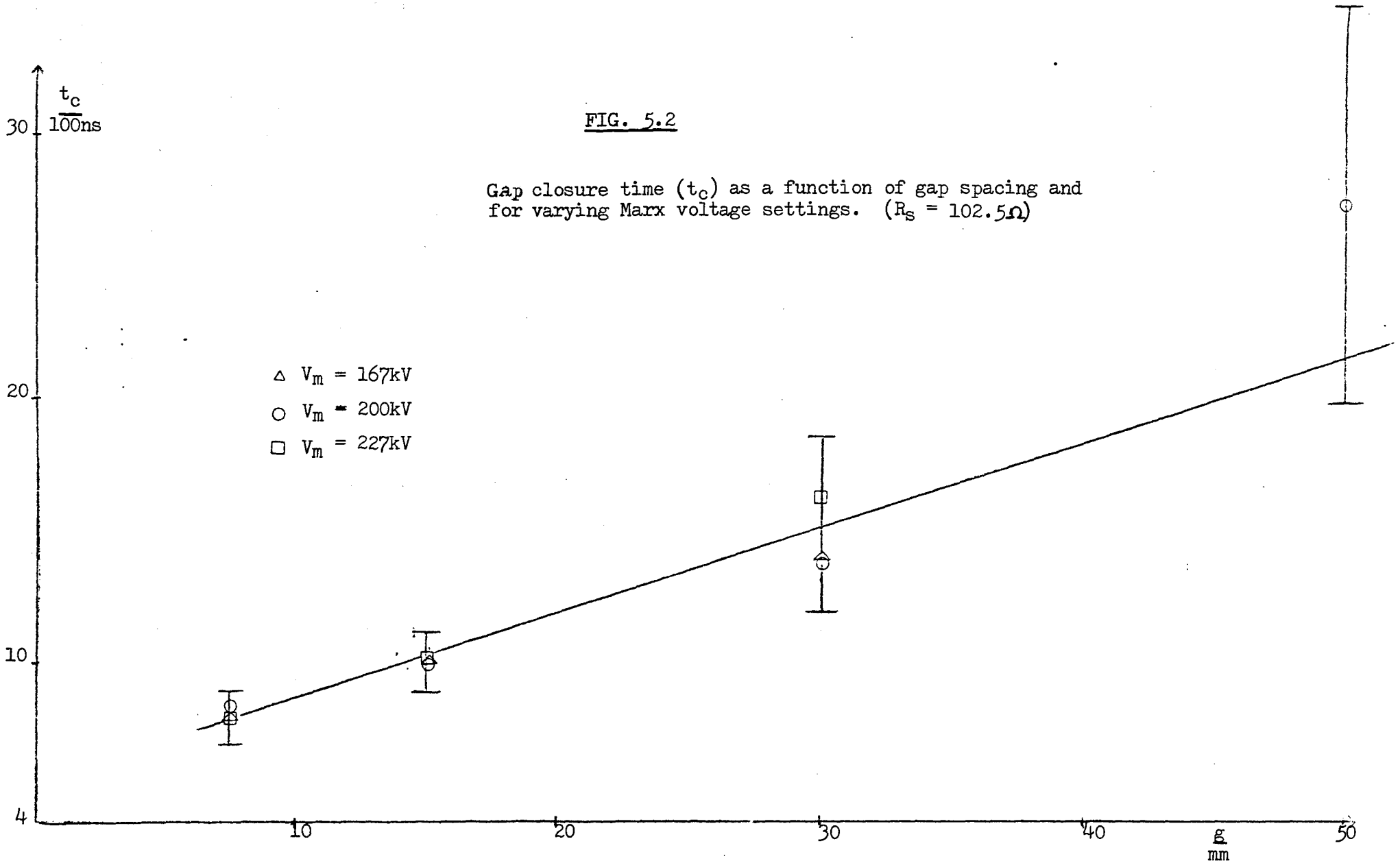

FIG. 5.3

FULL WIDTH HALF MAXIMUM GAP CLOSURE TIME (t_{FWHM}) FOR VARIOUS GAP SPACINGS AND AT DIFFERENT MARX VOLTAGE SETTINGS (R_S = 102.5Ω).

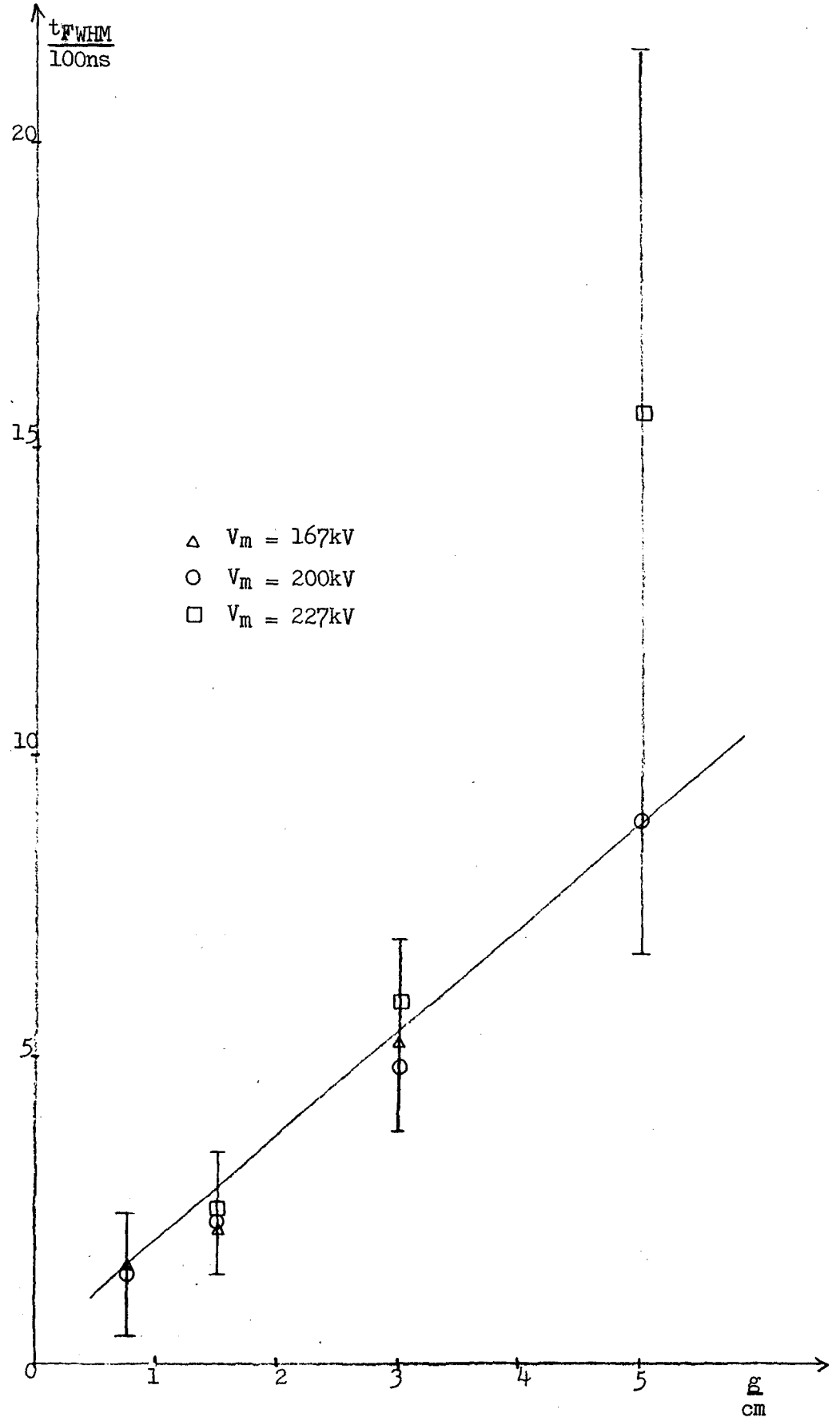

γ is the adiabatic exponent of the flare plasma, κ is the latent heat of evaporation of the cathode material and S is a superheat factor. Typical values of V_E observed by other workers are $(2 \sim 4)$ cm/μs.

Fig. (5.2) would indicate that the average flare plasma velocity is typically 4cm/μs, remembering that the pulse width for the diode voltage is approximately 200ns longer than the time required by the diode plasma to short out the vacuum gap.

As will be discussed later, the diode impedance can be given by

$$Z_D = \frac{c(d(t))^2}{V_D^{\frac{1}{2}}} \qquad (5.5)$$

where d(t) is the separation between the virtual cathode and the virtual anode formed by the electrode plasmas. This distance has been modelled by writing d(t) as [63]

$$d(t) = g - \bar{u}t \qquad (5.6)$$

where $\bar{u}$ is some average value of the approach velocity of the anode and cathode plasmas, and t is the time measured from the appearance of the diode current. Combining equations (5.5) and (5.6) yields the relation

$$\frac{1}{p^{\frac{1}{2}}} = (V_D Z_D)^{\frac{1}{2}} = c^{\frac{1}{2}} (g - \bar{u}t) \qquad (5.7),$$

where p is the beam perveance.

Equation (5.7) indicates that a plot of the square root of the inverse beam perveance against time will yield information on the plasma expansion velocity.

Such a plot is shown in Fig. (5.4) for differing values of the initial separation. The plots indicate that the velocity of the flare plasma may not be constant during the gap closure time but is typically 3.5 cm/μ s. The measurements of the diode impedance, necessary for these plots, are described in section (5.6.1).

FIG. 5.4

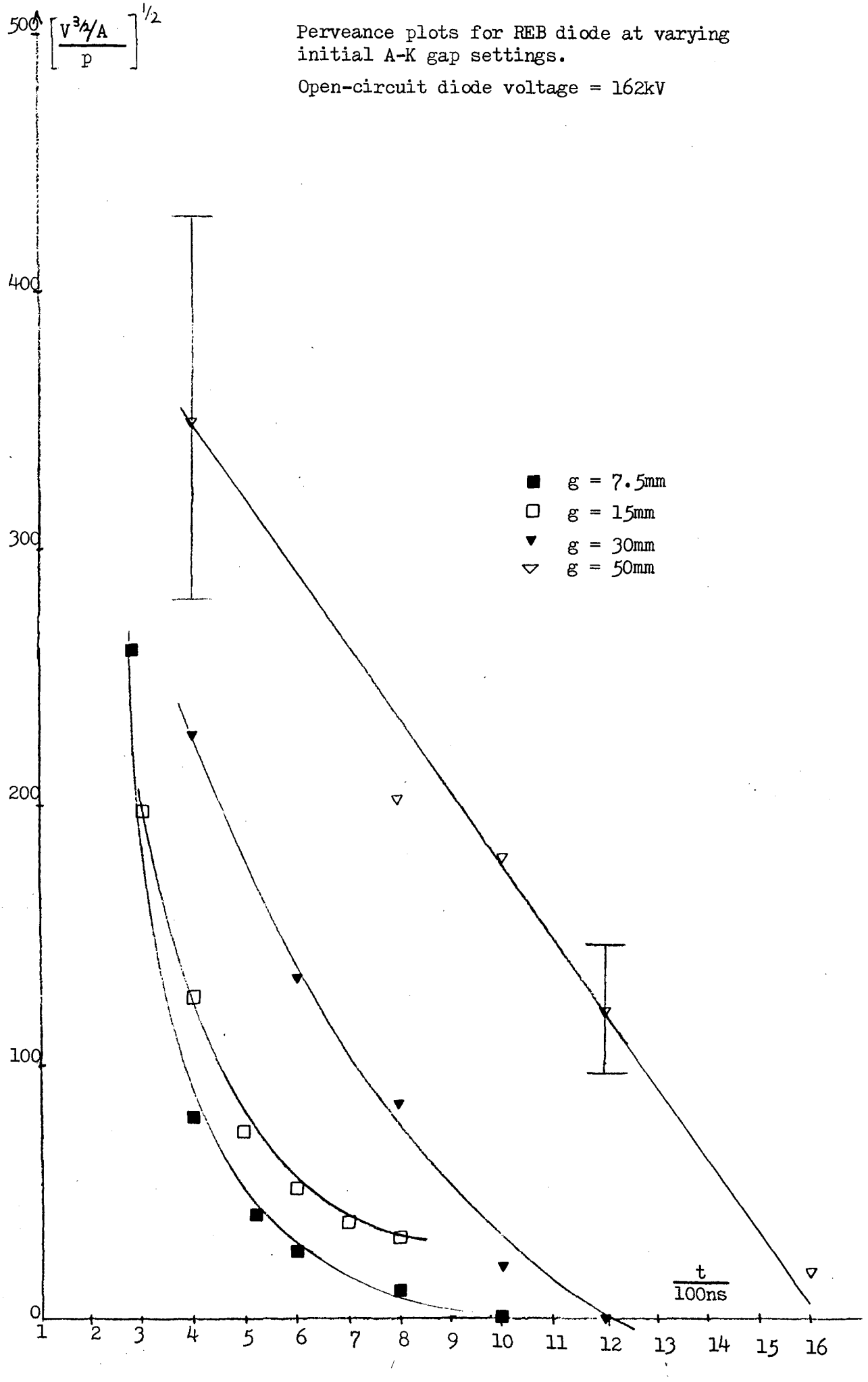

Perveance plots for REB diode at varying initial A-K gap settings.

Open-circuit diode voltage = 162kV

5.3.3 The Effect of the Magnetic Field on the Diode Voltage Profile

In the foilless diode of Friedman and Ury [63] the application of a magnetic field to the diode region resulted in an effective decrease of the plasma expansion velocity as the diode plasma had to move across the magnetic field lines, rather than along the field lines as in the case of a planar diode.

In order to see the effect of the presence of the solenoidal magnetic field on the temporal behaviour of the diode with which this thesis is concerned the diode was fired at a time at which the peak magnetic field of the pulsed coil was 0.4T.

For this test the coil was placed as close to the anode as the vacuum flanges would allow. As will be seen in Chapter Six the conducting anode flange situated between the A-K gap and the solenoid restricted the diffusion of the pulsed magnetic field into the diode region and subsequently little change in the diode voltage pulse-width was observed when the field was present. This proved to be useful in the experiments described in Chapter Six as it meant that the magnetic field in the drift tube could be altered without resulting in any change in the temporal behaviour of the electron energy so allowing one to alter the former parameter without necessarily altering the latter.

5.4.1 Anode Transmission

As the beam drift current was always observed to be much smaller than the diode current ($I_B/I_D < 0.05$) it is obvious that most of the A-K current was lost to the return earth loop rather than passing through the anode mesh. The anode grid spacing and mesh width indicate that on purely geometrical considerations one would expect thirty-five per cent of the incident electron flux to be transmitted to the evacuated drift tube.

However, the efficiency of transmission of diode current to relativistic electron beam current may have been limited by considerations other than geometrical capture cross-section. In particular, the possibility of large angular emissions of electrons from the cathode surface may have resulted in diode currents impinging on the anode flange rather than striking the transmission grid.

As will be discussed below, however, the contribution this mechanism is likely to have made in limiting the transmission of diode current is not thought to be large enough to explain the observed transmission factors. Therefore, some "non-geometrical" capture effects may have been present.

As the required angle of emission for an electron to strike the anode flange after leaving the cathode tip will depend upon the initial A-K gap setting one can expect some gap setting dependent transmission factor for the diode.

The trajectory of any electron will be dependent on its angle of emission and the electric field which it subsequently experiences.

Although the diode geometry is not simple and the distribution of potential in the A-K gap is not easy to calculate, conventional electrolytic tank techniques can be used to plot the electric field in the gap and such studies indicate that for the smallest gap setting (7.5mm) it is unlikely that emission angles of sufficient magnitude would have occurred to dump the electrons on the duralumin anode flange.

In order to investigate the hypothesis that some A-K gap dependent transmission effect exists, due to electrons striking the anode flange, measurements were made of beam current and diode current values at varying A-K gap separations with initial Marx voltage setting as a parameter. Due to the noise problems associated with the diode shunt measurements (see later) the diode current values which were used in the transmission plots were inferred from simultaneous measurements of the Marx current and diode voltage. This necessitated the need for three separate traces (I_B, I_M, V_D) to measure anode transmission, and, therefore, as each oscillogram had two traces, two shots were necessary for each calculation. This need for two shots for each experimental point is not too serious as the diode behaviour is fairly reproducible (for most settings). However, a reliable diode current shunt reading would have resulted in a smaller systematic error in any single

measurement of the transmission factor.

The electric field in a vacuum diode will be determined by the A-K gap separation and diode voltage. The distribution of potential however will depend only on the A-K spacing and not on the instantaneous cathode voltage. For a vacuum diode, therefore, the measurement of the anode transmission could be made at any time during the diode voltage collapse. However, the presence of the virtual cathode plasma in a relativistic electron beam diode will mean that the effective gap separation will depend upon the time at which the measurement is made. Due to the presence of the expanding plasma, transmission measurements were made at a fixed time after the rise of the electron beam current in order to ensure that the difference between the values of the diode gap settings before the application of the Marx pulse were the same as the difference between the effective gap separations. This assumes that the average flare plasma velocity will not vary with the initial gap setting. In order to accommodate the short pulse widths observed at the smaller gap settings a time of two hundred nanoseconds after the onset of the electron beam current was chosen at which to make the measurements, this time being large enough to give a sufficiently large beam trace to measure. Any possible error in the measurements arising from the relative timing of the signals due to signal cable length is likely to be small as the upper limit to the difference in diagnostic

cable length is six metres. This distance corresponds to a propagation time of less than twenty nanoseconds, one tenth of a division on the oscilloscope trace.

The plots of transmission against gap separation are shown in Fig. (5.5). From the data it can be seen that the percentage transmission is small ($\lesssim 5\%$). Although changes in the transmission between g = 7.5mm and g = 15mm are small in comparison with the experimental error there is a very definite decrease in the percentage transmission between g = 7.5mm and g = 50mm.

Recalling that little electron impingement on the anode flange is likely for the smallest gap setting it is apparent, in view of the small transmission, that the loss to the anode flange is much less serious than non-geometrical capture.

From the data plotted it would appear that, for a given gap setting, the anode transmission factor is smaller for the higher Marx bank voltage settings. Although the differences in anode transparency are small in comparison with the errors associated with each experimental point the fact that the errors are calculated from the systematic error in the diagnostic calibrations, rather than a random error from repeat measurements, might indicate that a Marx setting dependent transmission factor may exist. The source of this dependency is not obvious as the diode current

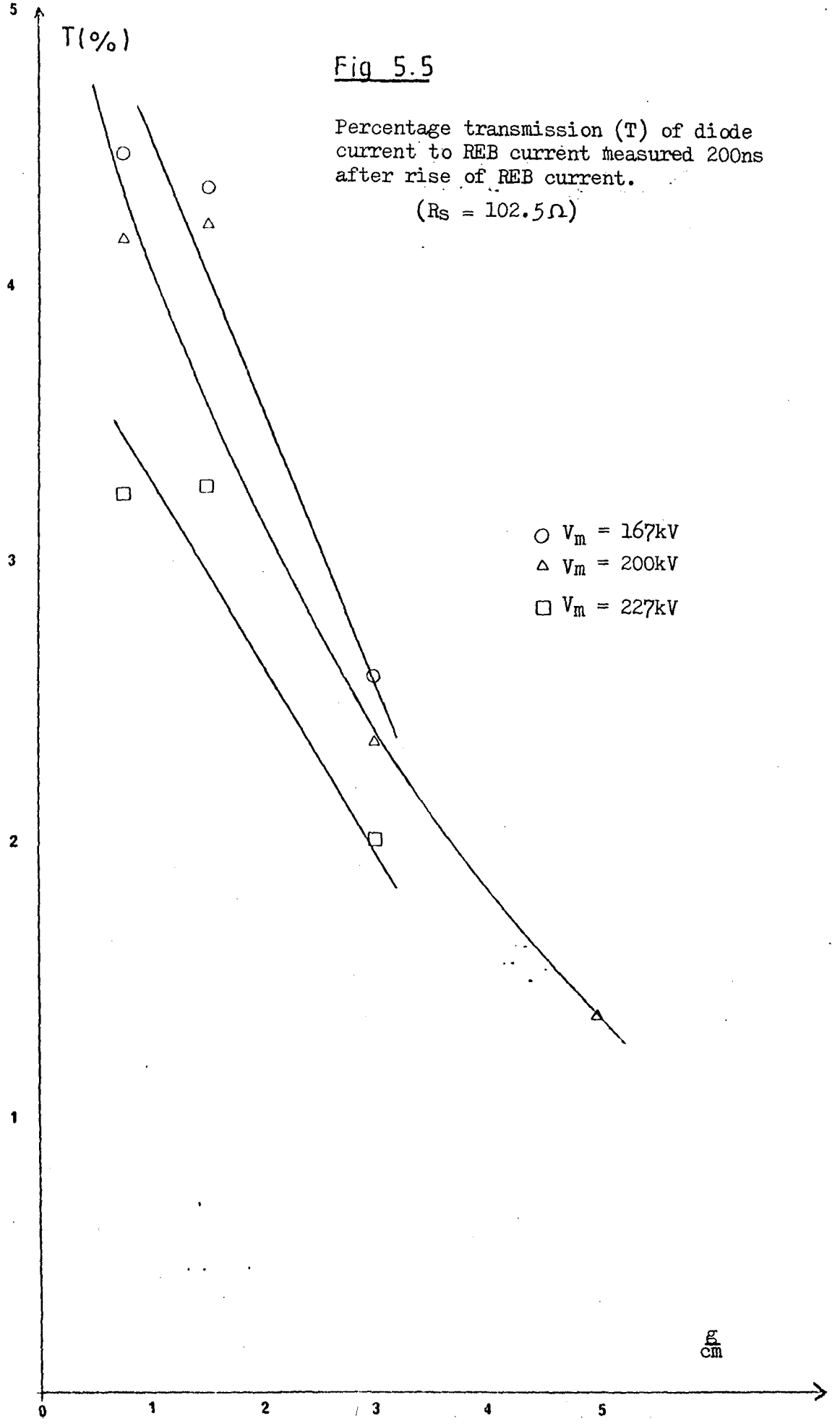

Fig 5.5

Percentage transmission (T) of diode current to REB current measured 200ns after rise of REB current.

(R_S = 102.5Ω)

is assumed to have come on when the diode voltage reached a specific value, for a given gap setting, although as illustrated in Fig. (5.1) the peak observed diode voltage increases with increasing Marx bank voltage setting.

It should be noted that the anode transmission is defined here as the ratio of the beam drift current to the diode current, rather than the percentage of the incident electron flux on the anode mesh which is transmitted to the evacuated drift region.

One would expect the geometrical anode capture to be a 'particle' effect, proportional to the beam charge density, rather than a current effect, proportional to the product of the charge density with the axial electron velocity. However, as little change in electron axial velocity is expected between the diode and the drift chamber the anode transmission is not thought to be due to decreasing axial velocity. To resolve the question completely a measurement of either the change in electron charge density or the change in electron axial velocity would have to be measured in addition to the diode and drift currents.

A separate measurement of the anode mesh transmission factor was made by measuring both the beam current and the diode current at a time when the diode voltage assumed a specific value (23kV). The value of voltage chosen was large enough to make the beam energy of interest in the cyclotron maser process and not so large as to result in too

small a beam current at the smaller gap settings. Due to the increasing diode voltage required to initiate breakdown at different A-K settings the time at which V_D = 23 kV is different for each measurement, and therefore, the extent of the plasma expansion will result in different effective gap settings for each measurement. These results also show a predominantly decreasing transmission with increasing gap spacing, (Fig. 5.6).

FIG 5.6

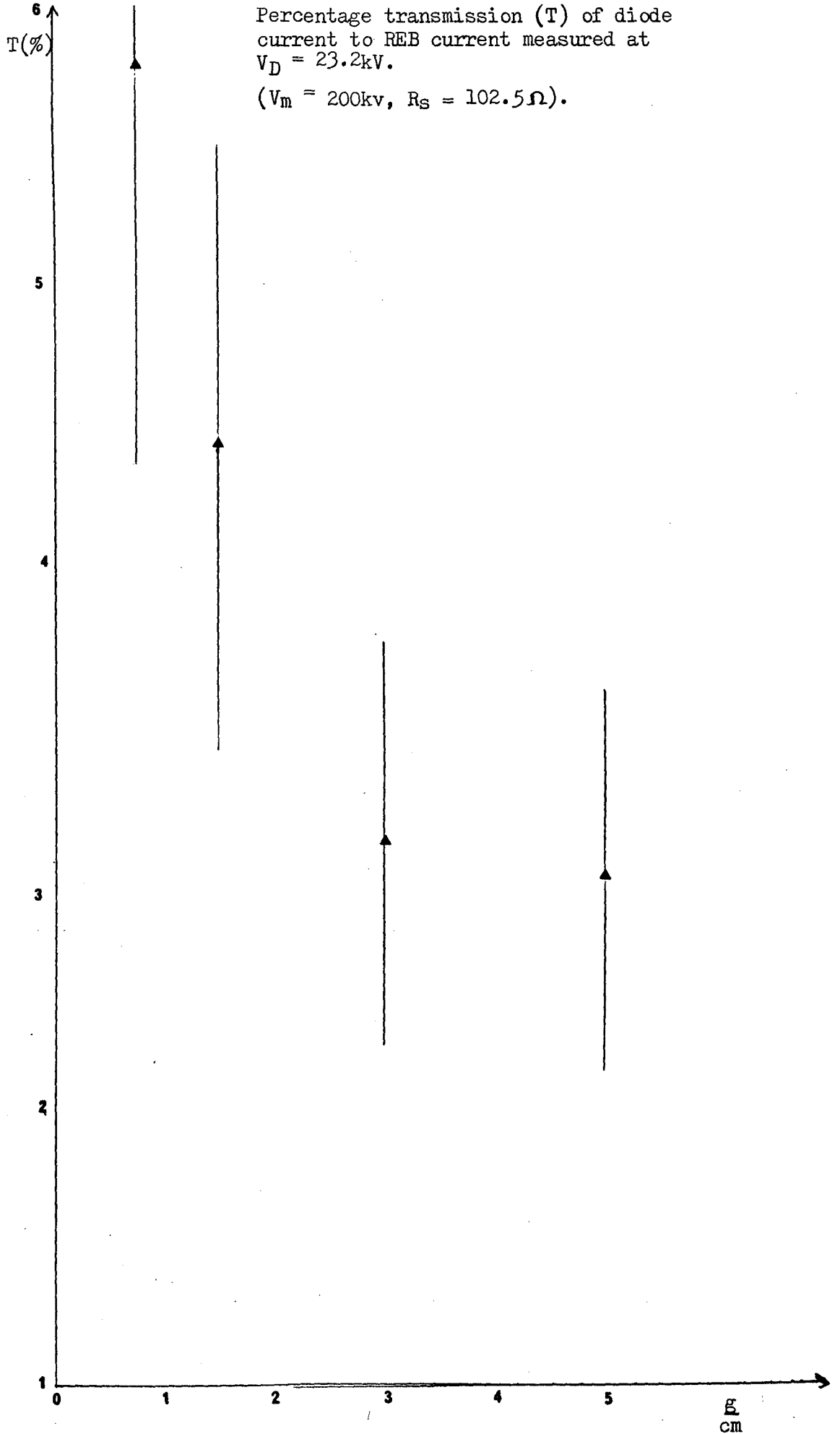
Percentage transmission (T) of diode current to REB current measured at V_D = 23.2kV.
(V_m = 200kv, R_S = 102.5Ω).
T(%)
6
5
4
3
2
1
0
1
2
3
4
5
g/cm

5.5.1 Electron Beam Characteristics

If the electron beam current transmitted to the vacuum drift region was not to see widely different magnetic field values due to the spatial variations in magnetic flux it was important that the beam should retain its hollow annular form.

The axial distance from the anode to the edge of the magnetic field coil, approximately eight centimetres, is shorter than the distance observed by other workers before beam instabilities in REB diodes began to "fill-in" the hollow beam profile [64]. Also, the geometry of the emitter-surface in the diode was expected to produce a very small inward component of radial electric field and so it was considered unlikely that the electric field distribution in the gap would "fill-in" the hollow beam profile. [65]

If the electron beam reached the magnetic field region before any transverse spreading occurred then the flux lines would have acted to reduce any subsequent transverse spreading further downstream by tying the particles to the magnetic flux lines. Observation of the faint damage pattern on the stainless steel laminar electron collector, placed in the drift chamber approximately halfway between the anode transmission grid and the edge of the magnetic field coil, indicated that little spreading had occurred.

The damage pattern on the collector consisted of a ring approximately five centimetres in diameter and five millimetres in thickness, dimensions consistent with the dimensions of the face of the cathode stalk.

The effects of radial space charge spreading will have been governed by the Lawson formalism discussed in Chapter One.

5.5.2 Space Charge Spreading

Typical observed values of diode voltage and electron beam current, along with the pertinent dynamical equations, can be used to predict paraxial streaming motion of the beam electrons and so explain the lack of space charge spreading indicated by the stainless steel collector.

The low operating pressures (2×10^{-6} millibar) in both the diode and drift tube regions will have resulted in the absence of collisonal ionisation and therefore charge and current neutralisation. However, beam energy deposition on the anode mesh and flange may have resulted in ion currents from the anode plasma so serving to depress the space charge potential in the diode and reducing radial expansion in the A-K gap.

The magnitude of the diode current transmitted to the drift chamber was typically 40A at diode voltages of approximately 50kV. The potential drop between the inner radius, a, and outer radius, b, and a grounded drift tube of

radius R is given by $\Delta\phi$ where

$$\Delta\phi = \frac{I}{4\pi\epsilon_0\beta c}\left[1 + \frac{2\ln(R/b) - 2\ln(b/a)}{(b^2/a^2 - 1)}\right] \qquad (5.8)$$

For this case then a radial potential drop of 4.4 kV is estimated with a drop of $\lesssim$ 2.5kV across the beam width. The value of the electron drift velocity used in estimating $\Delta\phi$ from equation (5.8) is calculated from the beam injection energy rather than beam drift energy, however, the correction to the drift velocity after calculation of the potential drop is only 3.5%.

Equation (1.2) for an un-neutralised stream reduces to,

$$K = \frac{2\nu}{\beta^2\gamma^3} \qquad (5.9)$$

which, in conjunction with

$$I_B = \left[\frac{ec}{r_o}\right] \beta\nu \qquad (5.10)$$

and,

$$\gamma = 1 + \frac{eV_D}{E_o} \qquad (5.11)$$

(where E_o is the rest energy of the electron, equal to 511 keV), allows the generalised beam perveance to be

calculated. Taking the beam injection energy and drift velocity to be 46 keV and 0.4c respectively gives a value of 0.057 for K. For the chosen values of I_B and V_D the classical beam perveance is 4.05 micropervs which would give a value of K = 0.061 for non relativistic electrons, which is in good agreement with the calculated value for the mildly relativistic electron current.

The calculated value of K in view of Lawson's work[2,3] would indicate that the beam would be stable against radial space charge spreading as a result of the beam's self electric field.

It should be stated that in equation (5.10) the value of β is that appropriate to the drift velocity, i.e. it is the ratio of the electron axial speed to the speed of light, whereas in equation (5.9) the value of β represents the actual speed of the electron, that is, $\beta^2 = 1 - 1/\gamma^2$. In this analysis no distinction has been made between different βs because of the value of the Budker parameter, ν/γ. Lawson identifies different β's by defining different gammas, but he shows that when $\nu/\gamma \ll 1$ then little difference need be taken into account. The value of $\nu/\gamma = 0.005$ appropriate to the beam in these experiments shows that this approximation is valid here. The above quoted values of ν and γ plotted on the "beam-chart" of reference (3) shows that the drift current in these experiments was within the space-charge limit region and so

formed a practical charge particle stream.

Although equation (5.9) is given for a solid cylindrical beam it can be shown that (keeping all other assumptions the same) the beam envelope equation for an annular beam density profile yields the same relation as equation (5.9), (Appendix 3).

5.6.1 Diode Impedance Collapse

The current-voltage relationship existing in an REB diode is known to be dependent on the time from the application of the diode voltage pulse.[66,67] The early rise of current in a cold cathode diode is governed by the Fowler-Nordheim equation for field-emission [6].

$$I_D = F^2\beta^2 K_1 A \exp(-K_2/\beta F) \qquad (5.12)$$

where F is the macroscopic electric field, A is the area of the emitter surface and K_1 and K_2 are constants for the cathode material. The field enhancement factor, β, is a product of two factors, one to account for enhanced current due to field enhancement at the edge of the cathode stalk and the other to account for field enhancement at the tips of the cathode whiskers. The geometry employed in the diode with which this thesis is concerned produced an electric field in the vicinity of the cathode a factor of three times greater than the average electric field in the diode [65].

Formation of the cathode plasma results in a transition from field-emission dominated flow to space-charge limited flow which, for relativistic diodes, would give the following current-voltage relation [6],

$$\left[1+\frac{eV_D}{m_o c^2}\right] \int_1 \frac{d\dagger}{(\dagger^2-1)^{1/4}} = \lambda I_D^{\frac{1}{2}} d \qquad (5.13)$$

where λ is a constant determined by the diode geometry and d is the effective anode-cathode gap separation. In the non-relativistic limit, equation (5.13) reduces to the familiar Child-Langmuir relation[68],

$$I_D = \frac{A\lambda' V_D^{3/2}}{d^2} \qquad (5.14)$$

where λ' is a constant, equal to 2.33×10^{-6} $A/V^{3/2}$ for a planar diode.

From equation (5.14) it can be shown that the diode impedance, $Z_D(t)$, may be given by,

$$Z_D(t) = \frac{c(V_D)\, d^2(t)}{V_D^{\frac{1}{2}}} \qquad (5.15)$$

where $c(V_D)$ is an insensitive function of the diode voltage. As d, the effective A-K gap separation decreases as a result of the expansion of the cathode flare plasma one would expect the diode impedance to decrease with increasing time.

5.6.2 Diode Impedance Collapse Measurements

In order to measure the temporal development of the gap impedance, simultaneous measurements of the diode current and diode voltage were made at varying times after the application of the Marx voltage pulse. These measurements were made for the operating conditions of Table (5.1).

Unfortunately, it was found that the diode shunt signals contained "noise" contributions which limited the usefulness of the shunt in measuring diode current. With both the diode voltage monitor and current shunt connected to the REB generator the shunt signals after gap closure were clearly erroneous, the shunt signal being vastly different with the voltage monitor disconnected. Even with only the diode current shunt directly connected to the experimental arrangement the early diode shunt signals still appeared to be in error as witnessed by the fact that they implied larger currents than the Marx current (measured using Rogowski # 3), and indeed even implied diode current larger than one would expect with the initial Marx voltage applied to the series resistor alone. Better agreement between the diode-shunt-implied current and the Rogowski-belt-implied current was obtained after diode gap closure, (plate 5.7).

An attempt to compensate for the noise contribution present on the diode shunt signal was made by firing the Marx bank such that the gap failed to break down and recording the

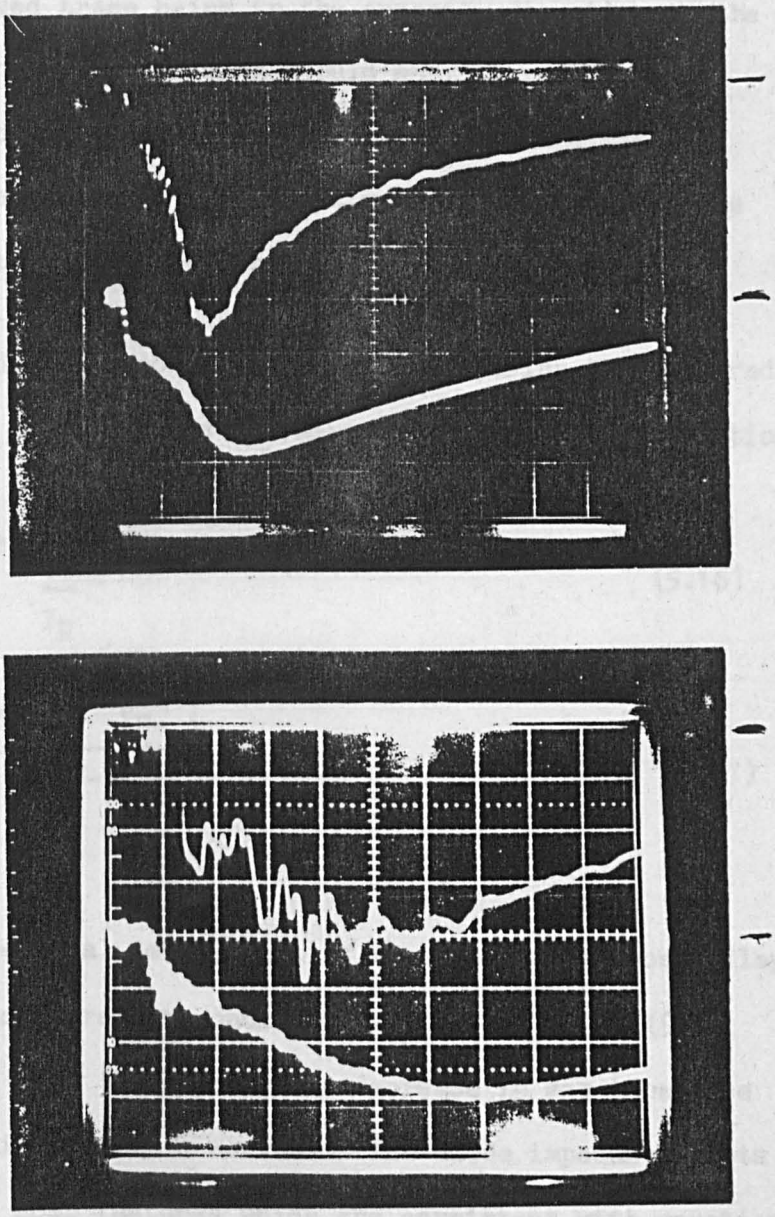

Plate 5.7 Top: Top trace is 1.7mΩ current shunt measuring diode current (1V/div) Bottom trace is Marx current signal (630A/div) from Rogowski loop.

Marx voltage setting was 225kV. Gap setting at 3 cm.

Series resistance = 102.5Ω. Time-base at 500ns/div.

Bottom: As top but time-base at 200ns/div.

The agreement between the two measurements improves at later times.

"noise" signal on the current shunt. This failed due to the observed trace being in the opposite direction to the normally observed trace and could not, therefore, be subtracted out from the normal trace. In addition, as no diode current was present it was not certain that the noise contribution would be the same.

The diode impedance was calculated using the measured values of diode voltage and Marx current using the relation,

$$Z_D = \frac{V_D}{I_D} \tag{5.16}$$

$$= \frac{V_D}{I_M - V_{D/R_m}} \tag{5.17}$$

The temporal development of the diode impedance collapse for various operating conditions is shown in Fig. (5.7) through to Fig. (5.12), and the decrease in gap impedance with time is readily observed. The diode impedance plots illustrate some features which are consistent with equation (5.15). Fig. (5.7) - Fig. (5.9) show the diode impedance development for a given initial Marx voltage setting with the gap setting, g, as a parameter.

It can be seen that the larger A-K spacings result in larger diode impedances. Alternatively, the plots of the diode impedance for a given initial A-K separation, with the Marx voltage as a parameter, shows that the diode

FIG 5.7

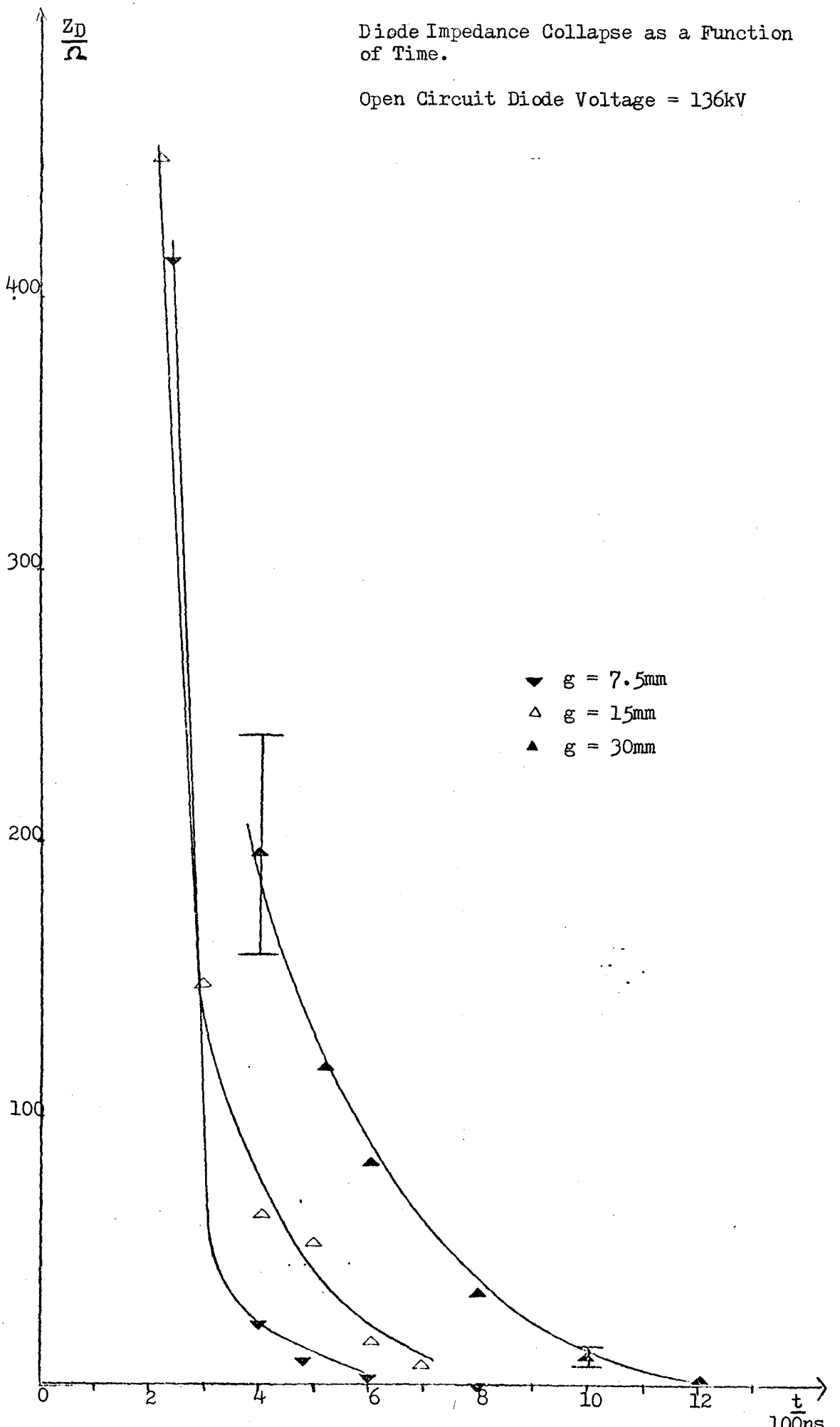
Z_D / Ω
Diode Impedance Collapse as a Function of Time.
Open Circuit Diode Voltage = 136kV
400
300
200
100
g = 7.5mm
g = 15mm
g = 30mm
0
2
4
6
8
10
12
t / 100ns

FIG. 5.8

Diode Impedance Collapse as a Function of Time.

Open Circuit Diode Voltage = 162kV.

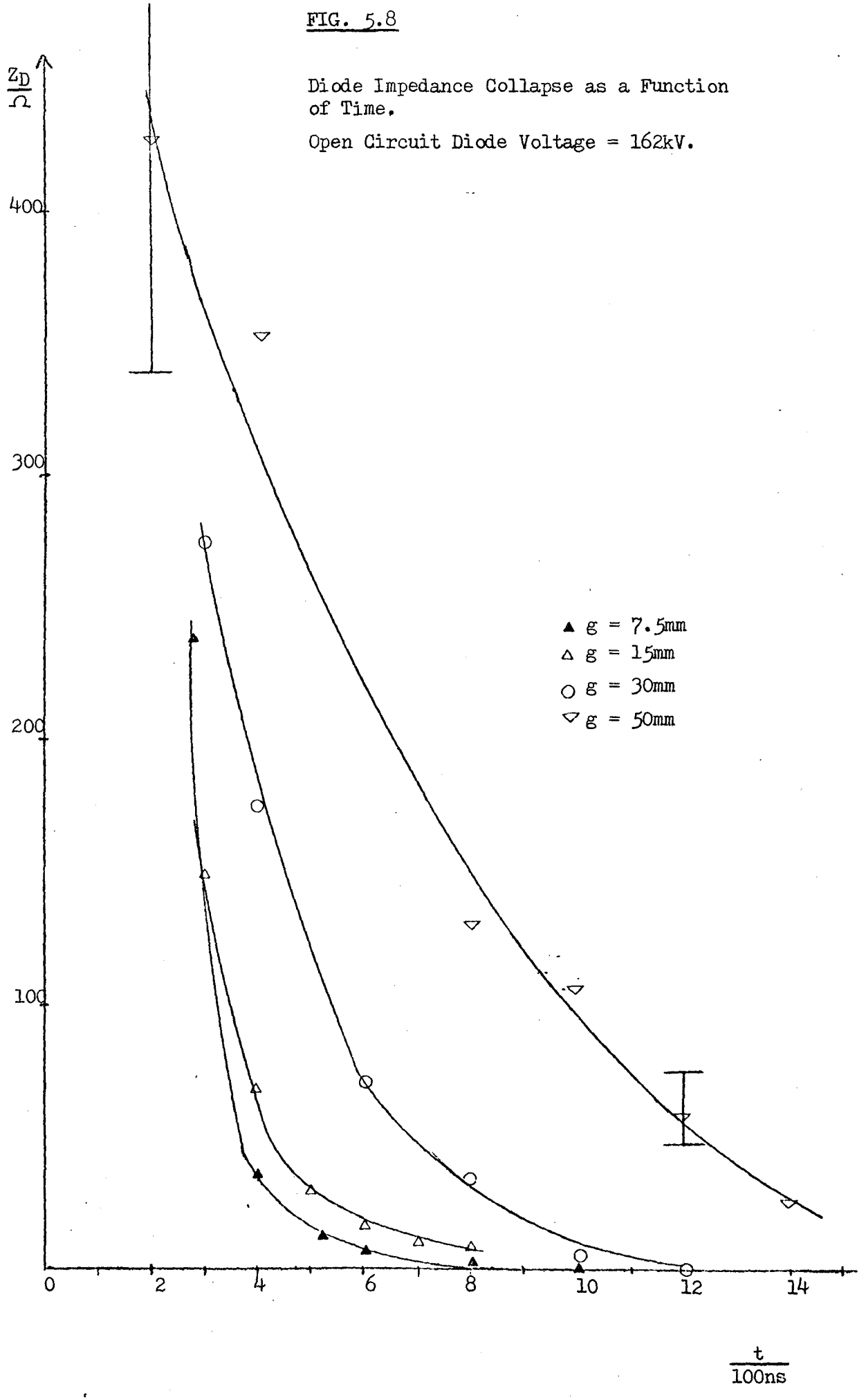

FIG. 5.9

DIODE IMPEDANCE COLLAPSE AS A FUNCTION OF TIME.

OPEN-CIRCUIT DIODE VOLTAGE = 184kV

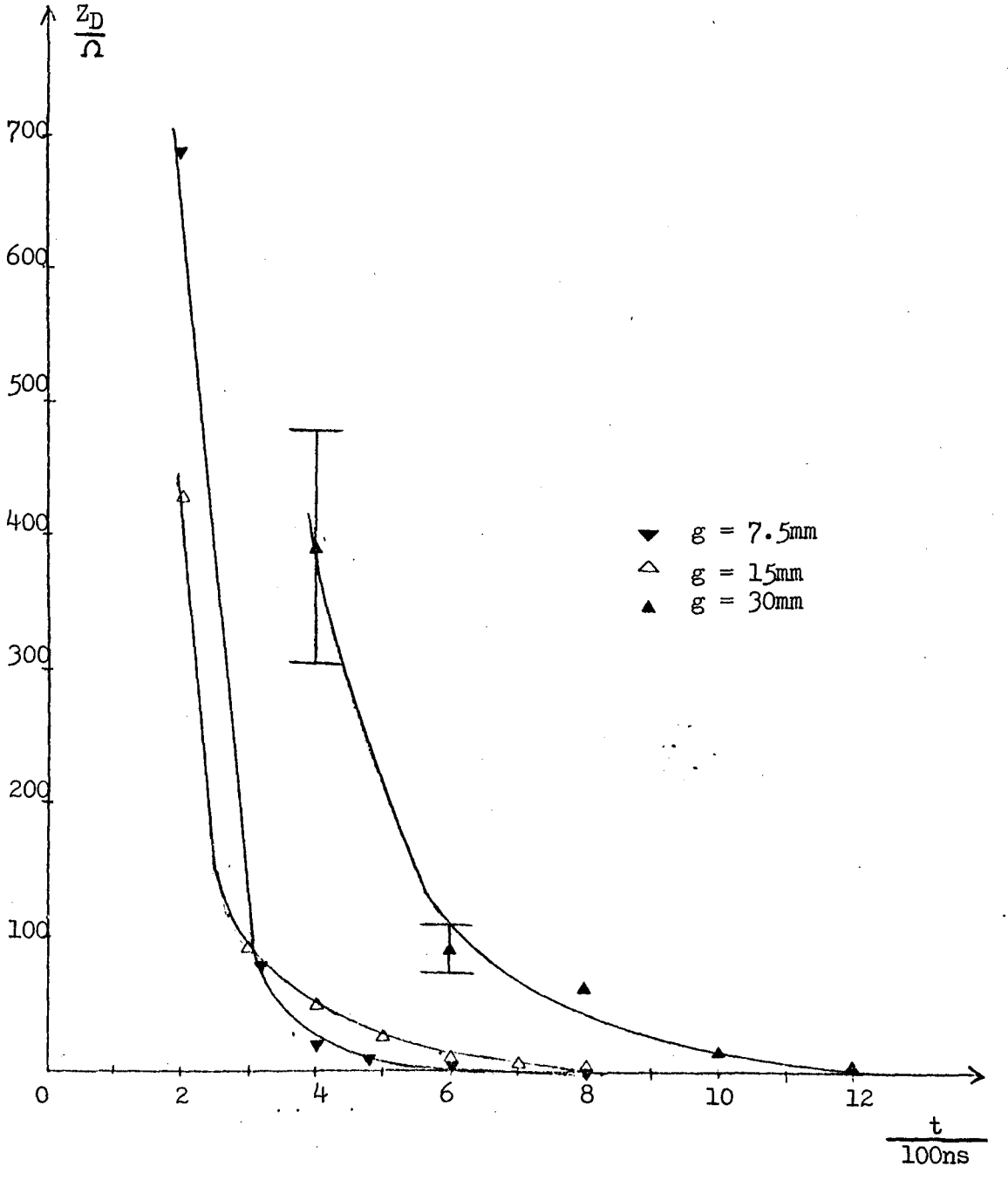

FIG. 5.10

Diode Impedance Collapse With Diode Open-Circuit Voltage (V_{oc}) as a parameter.

g = 7.5mm

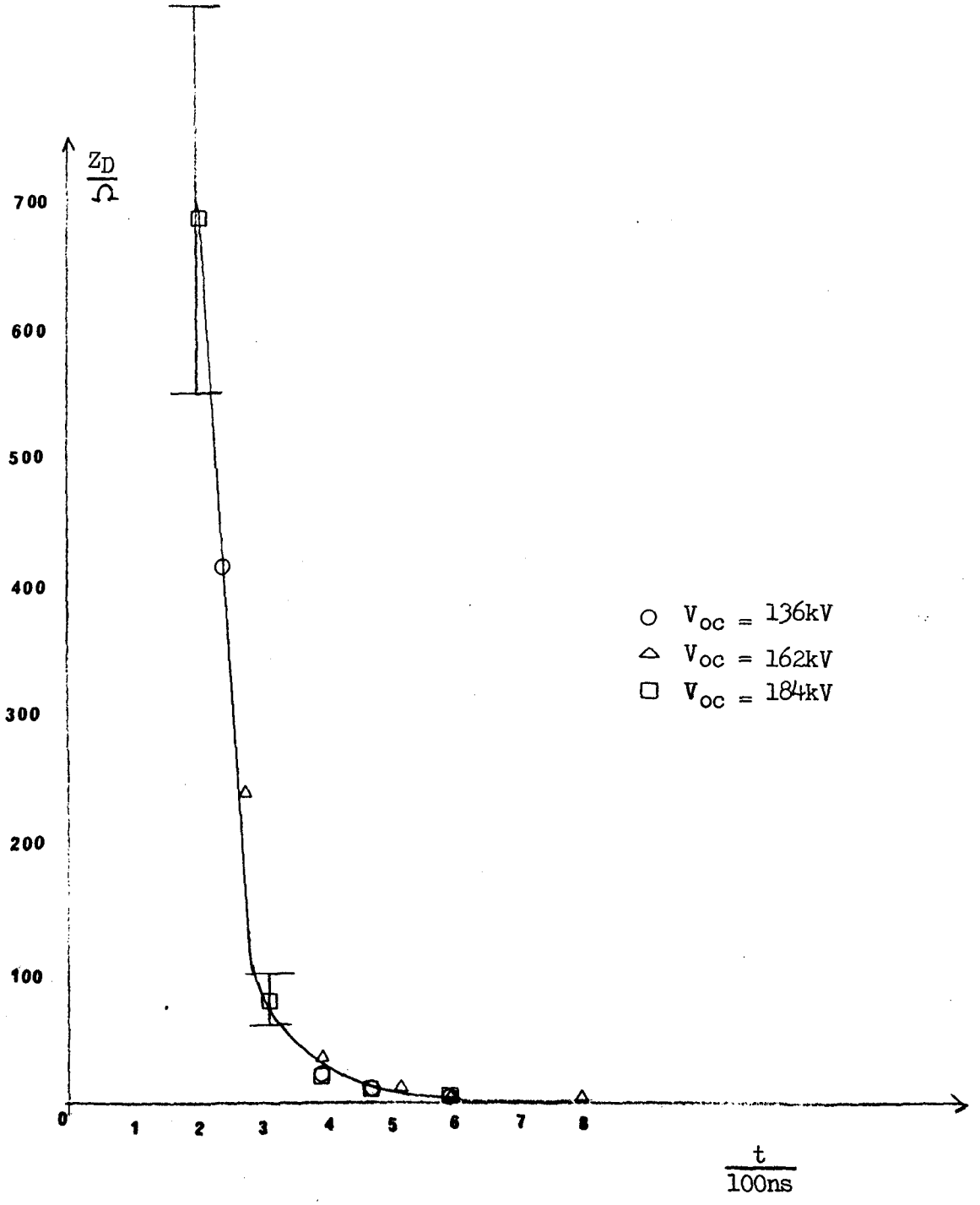

FIG. 5.11

Diode Impedance Collapse With Diode Open-Circuit Voltage (V_{oc}) as a parameter.

g = 15mm

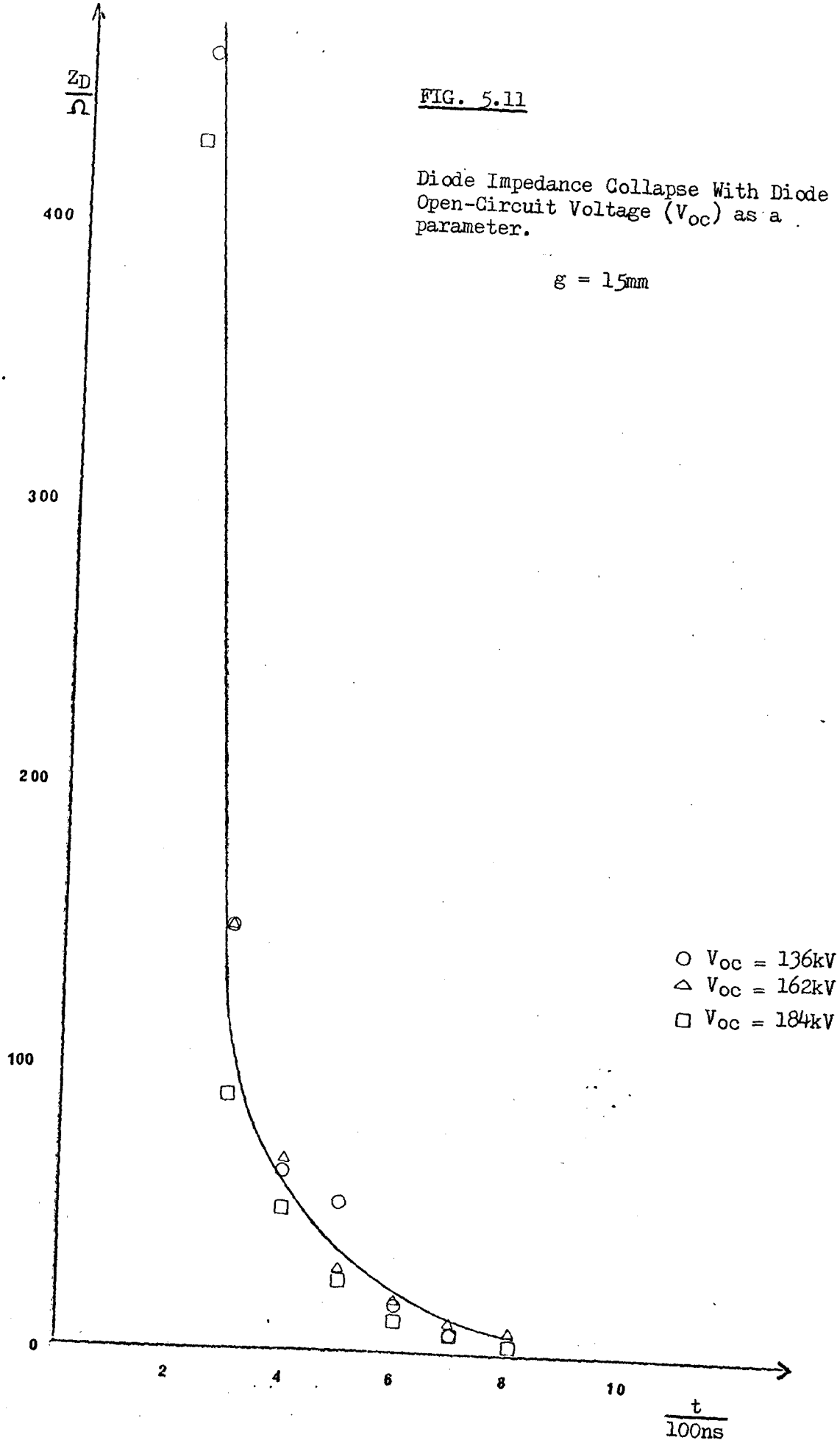

FIG. 5.12

DIODE IMPEDANCE COLLAPSE WITH DIODE OPEN-CIRCUIT VOLTAGE (V_{oc}) AS A PARAMETER.

g = 30mm

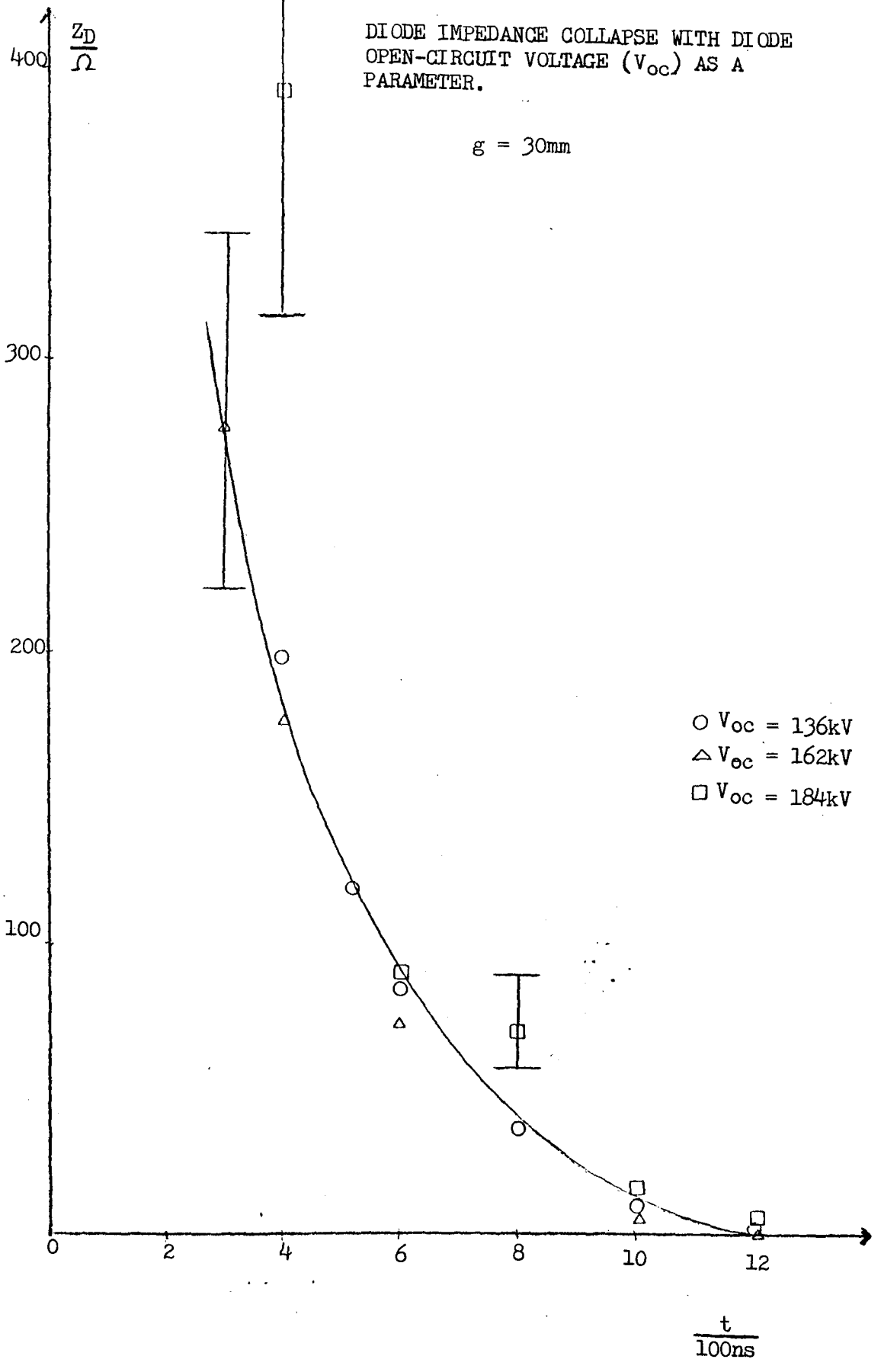

impedance is insensitive to initial Marx setting and that the diode impedance, at a given time from the switching of the Marx, is virtually the same for each open-circuit diode voltage.

As will be discussed in Chapter Six the diode impedance profiles of Fig. (5.12) were not identical to the diode behaviour observed while investigating the production of microwave radiation from the interaction of the e-beam with the magnetised drift tube. The change in the electrical behaviour of the A-K gap was thought to be a result of the removal of the field-grading rings which were placed between the anode and cathode, and to changes in the cathode emitter surface as a result of the large diode currents. This change in diode behaviour will be discussed further in section (6.10).

5.7 Errors

Except where stated the error bars shown in graphs in this chapter concerning the measurements of Marx current, electron beam current and diode voltage were estimated from consideration of the following;

(i) the calibration error associated with the CRO amplifier sensitivities;

(ii) the scale resolution error associated with recording the signal magnitudes from the oscillograms. Consideration was also taken of the contribution electromagnetic noise made to the uncertainty in reading some of the oscillograms;

(iii) the error in the calibration of the sensitivities of the diagnostic used to measure each of the above parameters.

5.8 Summary

The experimental work with which this chapter has been concerned yielded information on the behaviour of the REB diode which was valuable to commencing work on beam injection into the magnetised drift region. The variation in the diode voltage pulse width with changing A-K gap separation illustrated that pulse durations of sufficient interest for the microwave production experiments could be obtained by proper selection of initial A-K gap spacing. In addition, the measured values of electron beam current, although much less than the diode currents, indicated that a stable, mildly relativistic beam of $\gtrsim$ 50A would be available for injection into the evacuated drift tube.

CHAPTER SIX MICROWAVE GENERATION

6.1 Introduction

This chapter deals with the results obtained on the generation of microwave radiation by injecting the relativistic electron beam into the vacuum drift region in the presence of the quasi-static magnetic field. Before looking for microwave radiation the axial magnetic field profile of the pulsed solenoidal coil was mapped out by measuring it with magnetic flux probes (section 6.2). Microwave radiation was observed at both X-band and Ka-band frequencies and the level of the radiation was seen to be strongly dependent upon the value of the external magnetic field strength.

6.2 The Axial Magnetic Field Distribution

In order to inspect spatial variations in the axial magnetic field of the pulsed solenoidal coil two small differentiating flux probes were constructed. The flux probes consisted of enamelled wire wound on a hollow insulating rod and of diameter(14.98 ± 0.02) mm. The first and second probes (see Fig (6.1)) had fifty-three and fifty-four turns respectively. In order to prevent the probe turns from moving, and perhaps changing the probe sensitivities, the enamelled wire was wound through holes drilled in the insulating tube wall leaving the probe centres a fixed distance of 9.6 cm apart. The insulating tube on which the flux probes were wound was, in turn, fixed to a long piece of earthed copper pipe. The probe wires had their enamel stripped back and the bared ends soldered to the inner and outer of co-axial cable which was drawn through the copper tubing and terminated in BNC-bulkhead sockets to which cables could be attached for recording signals. The copper tube was mounted on supports which allowed one to vary the positions of the probes along the cylindrical axis of the solenoidal coil. The conducting tube had a marker on it which allowed the positions of the probes, relative to the magnetic field coil, to be recorded.

Initial investigations were aimed at measuring the vacuum distribution of the longitudinal magnetic field component of the solenoid inside and outside the coil.

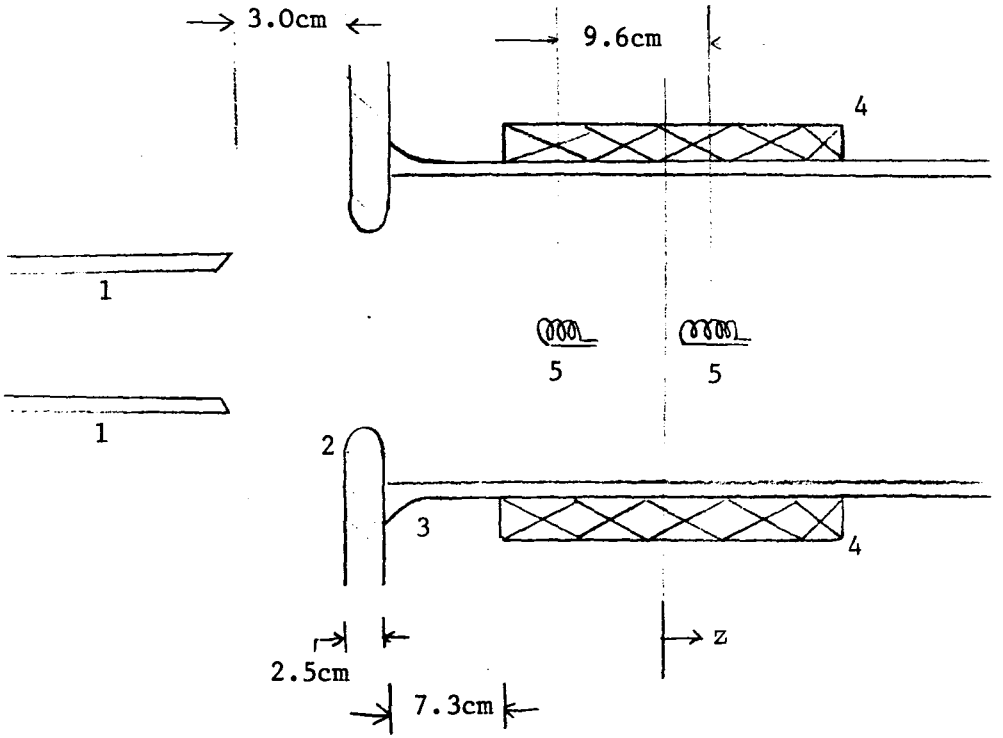

Fig. 6.1

ARRANGEMENT FOR MEASURING AXIAL DISTRIBUTION OF MAGNETIC FIELD

For these tests the coil was positioned centrally between the vacuum flanges on the QVF tube to avoid distortion of the pulsed magnetic field distribution by the conducting flanges, Fig. (6.2). Axial variations in the magnetic field on axis of a finite length solenoid are given by the familiar expression, (in the geometry of Fig. (6.1)),

$$\frac{B_z}{B_o} = \tfrac{1}{2}\left[\frac{(l/2 - z)}{\sqrt{(d/2)^2 + (l/2 - z)^2}} + \frac{(l/2 + z)}{\sqrt{(d/2)^2 + (l/2 + z)^2}}\right] x\left(1 + \frac{d^2}{l^2}\right)^{\frac{1}{2}} \qquad (6.1)$$

where B_o is the field at the centre of the coil,

$$B_o = \frac{\mu_o N I}{l\left(1 + d^2/l^2\right)^{\frac{1}{2}}} \qquad (6.2)$$

Figure (6.2) shows the results obtained from probing along the axis of coil # 3 (see Chapter Three) compared with the theoretical profile. Although the agreement is good it is stressed that the probe measurements are only relative. The long probe lengths mean that the axial field measurements are an average over twenty-eight millimetres, and these measurements yield only the axial field profile rather than absolute values.

The magnetic field is still determined by measuring the circuit current and the probes could be calibrated by placing either directly in the centre of the solenoid and calibrating against the Rogowski signal. Although the flux probe geometries were known accurately their

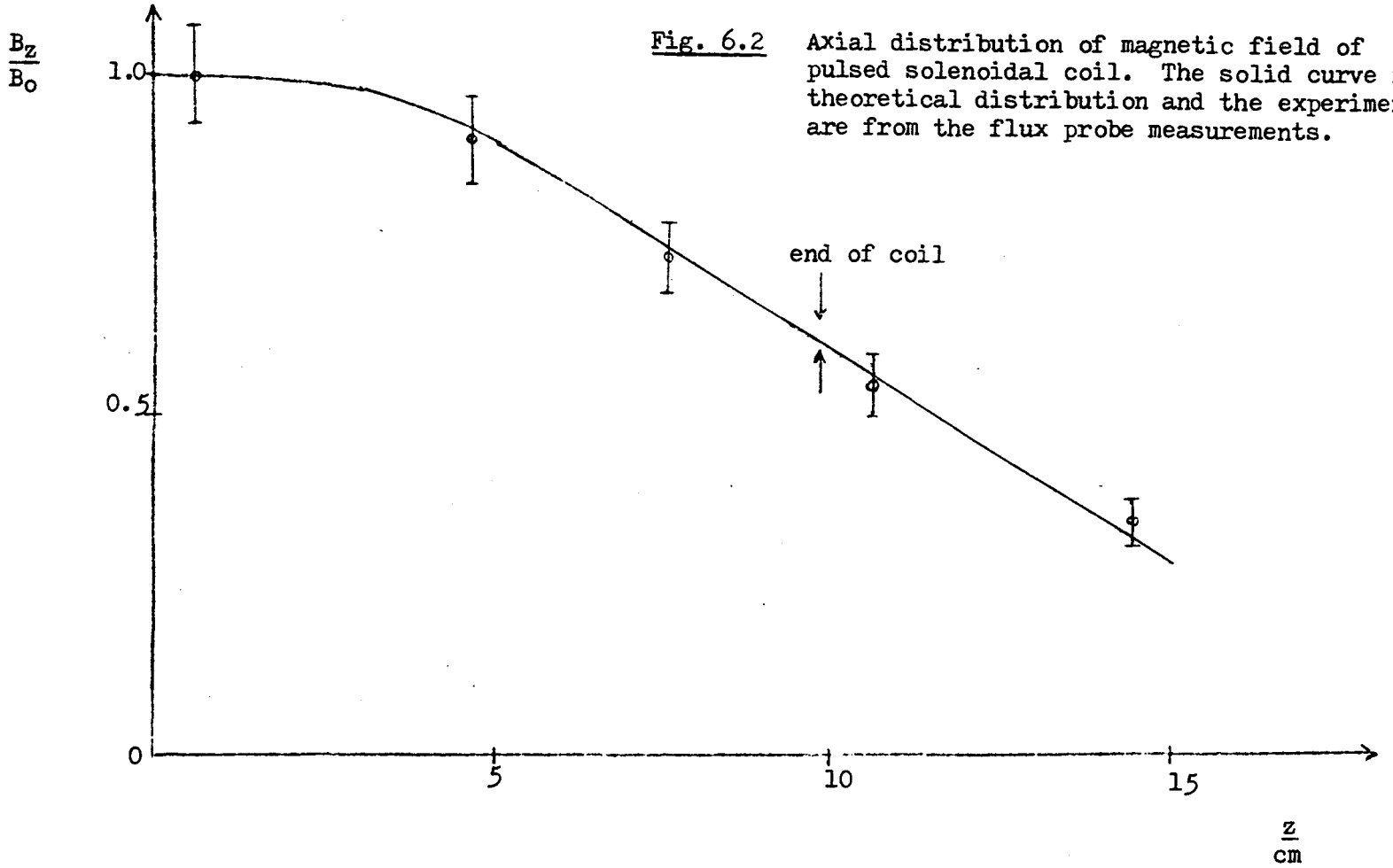

Fig. 6.2 Axial distribution of magnetic field of pulsed solenoidal coil. The solid curve is the theoretical distribution and the experimental points are from the flux probe measurements.

calibrations were not easily calculable due to the long probe lengths, these being desired for good probe sensitivity. Despite this difficulty an approximate calculated probe sensitivity was within seven percent of the value indicated by comparison with the Rogowski signal.

A more important series of measurements were made with the coil moved as close as possible to the anode flange. Probe measurements with this arrangement allowed one to estimate the magnitude of the magnetic field inside the A-K region at various times from the start of the magnetic field current pulse. Oscillograms show that close to, and inside, the A-K region, where conducting materials exist, the magnetic flux is excluded at early times by the anode flange. However, once flux "leaks" into the diode region it is "trapped" there and remains for longer times than it does within the drift tube region. Plate (6.1) shows the development of the magnetic field with time for a given probe position.

This occurrence whereby the pulsed external magnetic field leaked into the evacuated drift region quicker than it leaked into the diode region has been used by Ginzburg et al [69] to control the magnetic mirror ratio between their interaction region and their diode by varying the delay between the application of their diode voltage pulse and their magnetic field.

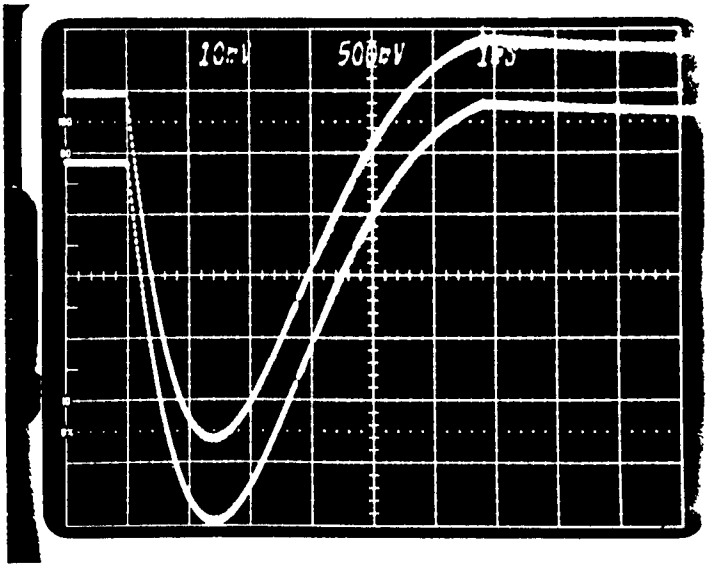

Plate 6.1 (a)

Plates6.1 (a), 6.1 (b) and 6.1 (c) illustrate how the magnetic field changes with time at different points along the axis of the magnetic field coil. The positions are given in the geometry of Fig.(6.1). The top traces pertain to the probe furthest from the anode flange.

Top: z = -0.6 cm, 0.1T/div.

Bottom: z = -10.2 cm, 0.05T/div.

Time-base at 1ms/div.

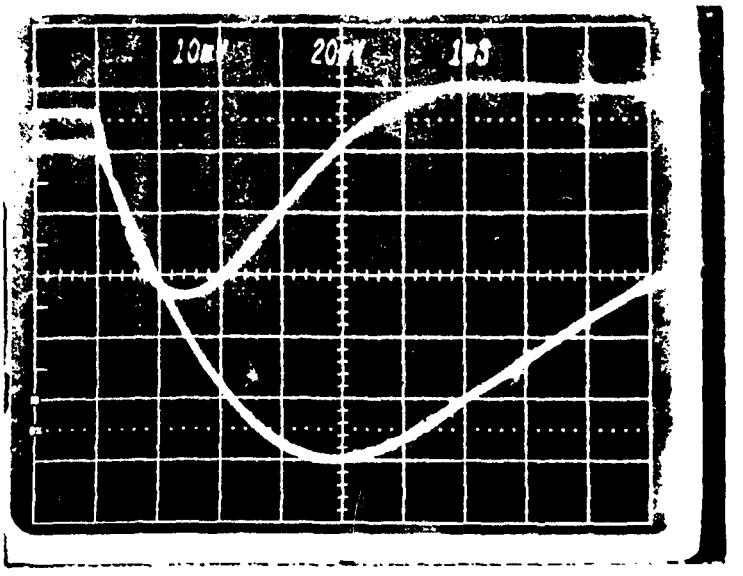

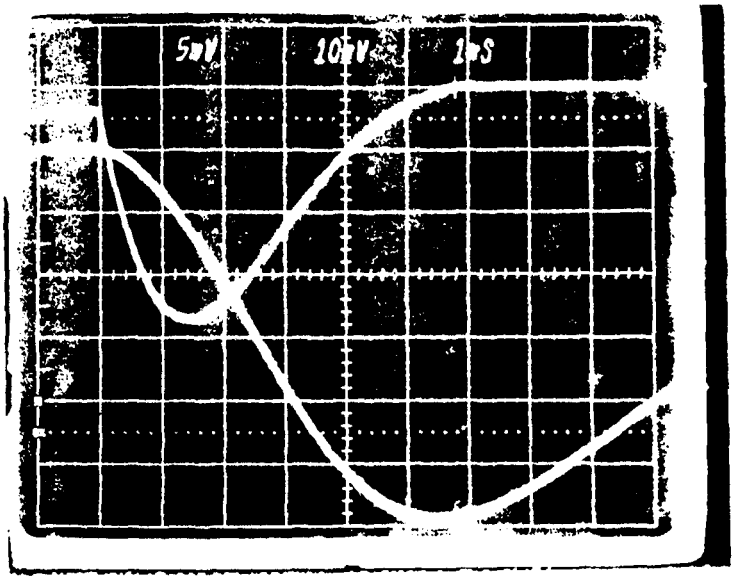

Plate 6.1 (b)

Top photo, Top: z = -10.6 cm, 0.1T/div

Bottom: z = -20.2 cm, 0.002T/div

Bottom photo, Top: z = -13.6 cm, 0.05T/div

Bottom: z = -23.2 cm, 0.001T/div

Time-base at 1ms/div.

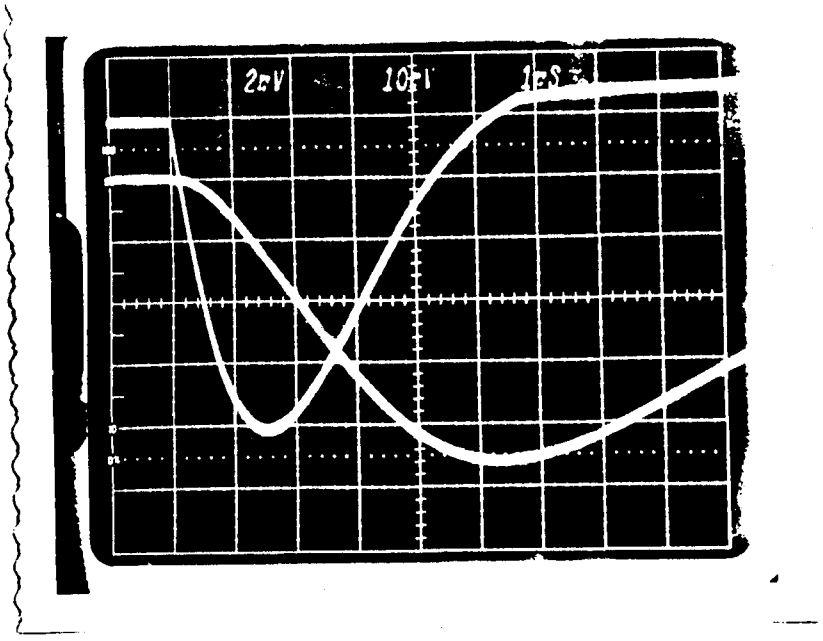

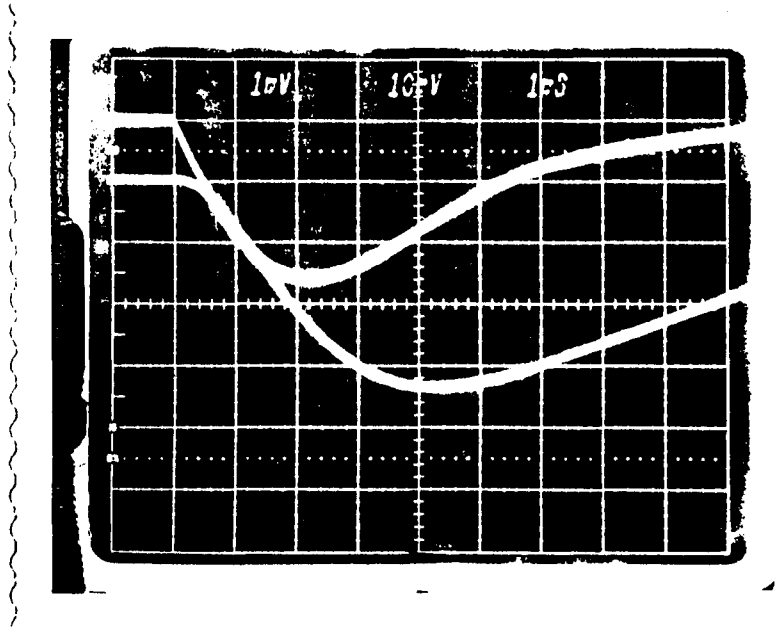

Plate 6.1 (c)

Top photo, Top: z = -15.6 cm, 0.02T/div

Bottom: z = -25.2 cm, 0.001T/div

Bottom photo, Top: z = -18.6 cm, 0.01T/div

Bottom: z = -28.2 cm, 0.001T/div

Time-base at 1ms/div.

On some shots the magnetic flux probes were placed underneath the high tension end of the pulsed solenoidal coil and the probe connections to the coaxial cable were reversed to check for the possibility of electrostatic effects. Although the resulting signals were of equal size irrespective of how the probes were connected, both probes were covered in a shield of aluminium foil which was fastened to the earthed copper tubing. The shield was then covered in electrically insulating material to prevent the aluminium shielding touching conducting parts of the diode, an effect which was assumed to have occurred when the respective probes gave widely differing values when used to measure the magnetic field at the same axial position.

In order to eradicate a "pulse" of noise early in the flux probe signal the BNC socket attached to the coaxial cable coming from the probe was insulated from the earthed copper tubing. The source of this noise was the pulse generator which was used to provide a trigger for the pulsed magnetic field discharge current.

The distribution of the magnetic field along the coil axis and inside the diode at different times is shown in Figs. (6.3 and 6.4).

When measuring the time development of the solenoidal field the oscilloscope time-base was triggered a little

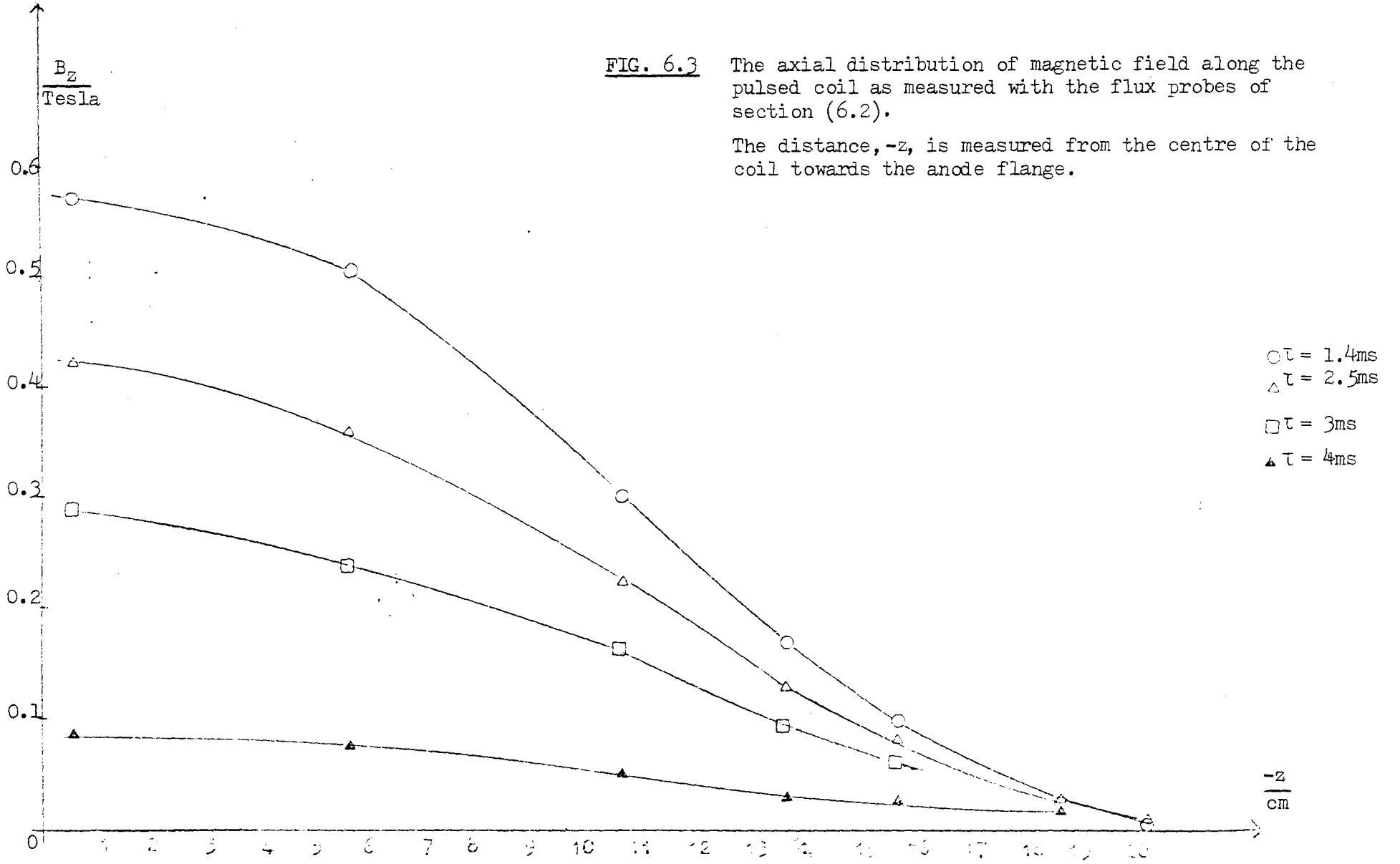

FIG. 6.3 The axial distribution of magnetic field along the pulsed coil as measured with the flux probes of section (6.2).

The distance, -z, is measured from the centre of the coil towards the anode flange.

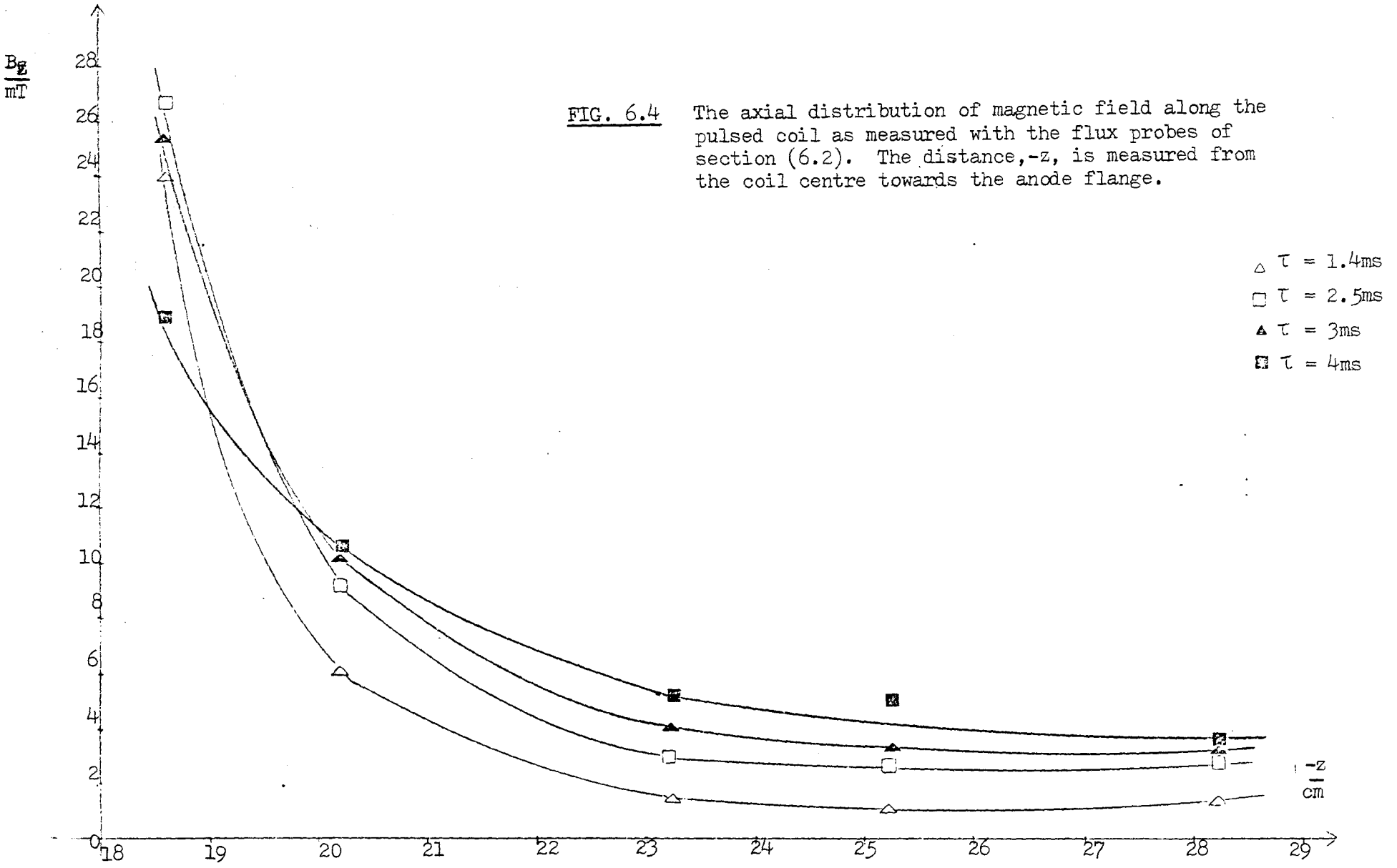

FIG. 6.4 The axial distribution of magnetic field along the pulsed coil as measured with the flux probes of section (6.2). The distance, -z, is measured from the coil centre towards the anode flange.

earlier than the field current in order to ensure that the timing was properly recorded, that is, the "zero-time" was correctly measured.

When measuring the magnetic field values at times of 4 milliseconds after the rise of the solenoid current it was obvious the integrator times were becoming too short to be valid as witnessed by the probe signals going through zero prior to the Rogowski loop signals on the same shot. In order to measure the magnetic field at such times an integrator of a much larger "RC" time could be employed, however, the small magnetic field values far from the coil centre meant that the probe-integrator combination was not sufficiently sensitive to measure accurately. In order to circumvent this difficulty an active integrator technique was employed. With this configuration the valid integration time, t_I, which for a passive integrator is $t_I \ll RC$, is, $t_I \ll RC(G+1)$, where G is the open loop gain of the amplifier in the integrator circuit [56]. However, the integrator sensitivity, given by equation (4.3), is multiplied only by a factor $\frac{G}{G+1}$ which is virtually unity. Hence, much shorter RC times may be employed for increased sensitivity without affecting the integration time. For these measurements an operational amplifier of gain approximately equal to 7000 was used and an RC time of 0.97 ms was employed, giving the integrator a valid integration time of up to 100 ms.

Radial and axial misalignment of the flux probes provided a possible source of error in the measurements of the axial magnetic field profile. In particular, stress due to the weight of the copper tube might have "dipped" the front probe a little resulting in its end face not being perpendicular to the axis of the solenoid. In addition, magnetic pressure between the end of the coil and the conducting anode flange resulted in a very gradual shift of the coil position, approximately seven millimetres. However, the good agreement between the probe and Rogowski signals during the vacuum profile measurements indicated that any errors were small.

6.3 Microwave Measurements

Initial experiments involving the injection of the relativistic electron beam into the magnetised vacuum drift region consisted of firing the beam into randomly chosen magnetic field values and cautiously inserting large levels (60dB) of attentuation in front of the microwave diode. The X-band detection system was employed for these experiments. The absence of any signal above noise levels prompted the gradual removal of all attentuation and a continued search for microwave power using different peak solenoid currents and different time intervals between discharge of the Marx circuit and solenoid capacitor banks. The eventual appearance of microwave diode signal under some conditions resulted in a more ordered search through a range of magnetic field values.

The scan through magnetic field strength was carried out mainly by varying the value to which the solenoid charging banks were charged rather than varying the time, τ, between the discharge between the two banks. The voltage setting was more readily altered, by simply switching the magnetic field at the occurrence of any desired reading on a digital multimeter (Chapter Four), than the time interval, τ, which was set by altering the delay between two trigger pulses observed on the time-base of an oscilloscope.

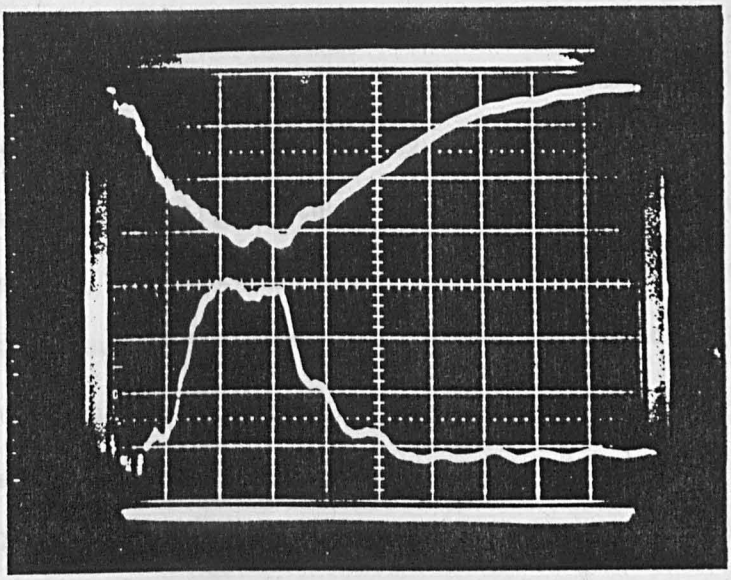

Plate 6.2

The bottom trace shows a typical microwave output power signal. External magnetic field was set at 0.322T. P_μ = 16 kW.

Top trace is diode voltage (23.2kV/div).

Time-base at 200ns/div.

The fact that the microwave signal was definitely dependent on the presence of the magnetic field was confirmed by repeatedly firing the Marx bank on its own or by firing both banks but by arranging the time interval between the firing of the banks to be zero and thus injecting the electron beam into zero magnetic field. Fifteen successive shots with the aforementioned conditions resulted in no detection of any microwave signal and occasional single shots (misfires, in fact) with zero field demonstrated that both the e-beam and magnetic field were necessary for observation of microwave emission.

With the time-interval, τ, between switching on the magnetic field current and injecting the electron beam into the drift region set at 2.5 ms a scan through various magnetic field settings revealed variations in the level of the output signal from the microwave diagnostic. The microwave output signal variations are shown in Fig. (6.5). The immediate point of interest in the microwave signal output variations is the appearance of "resonant" magnetic field settings at which relatively large signal levels of output radiation are evident. The microwave signal levels plotted in Fig. (6.5) as well as those used for further graphs in this chapter, are the peak levels recorded on each individual oscillogram, irrespective of the time at which this level occurred with respect to the Marx

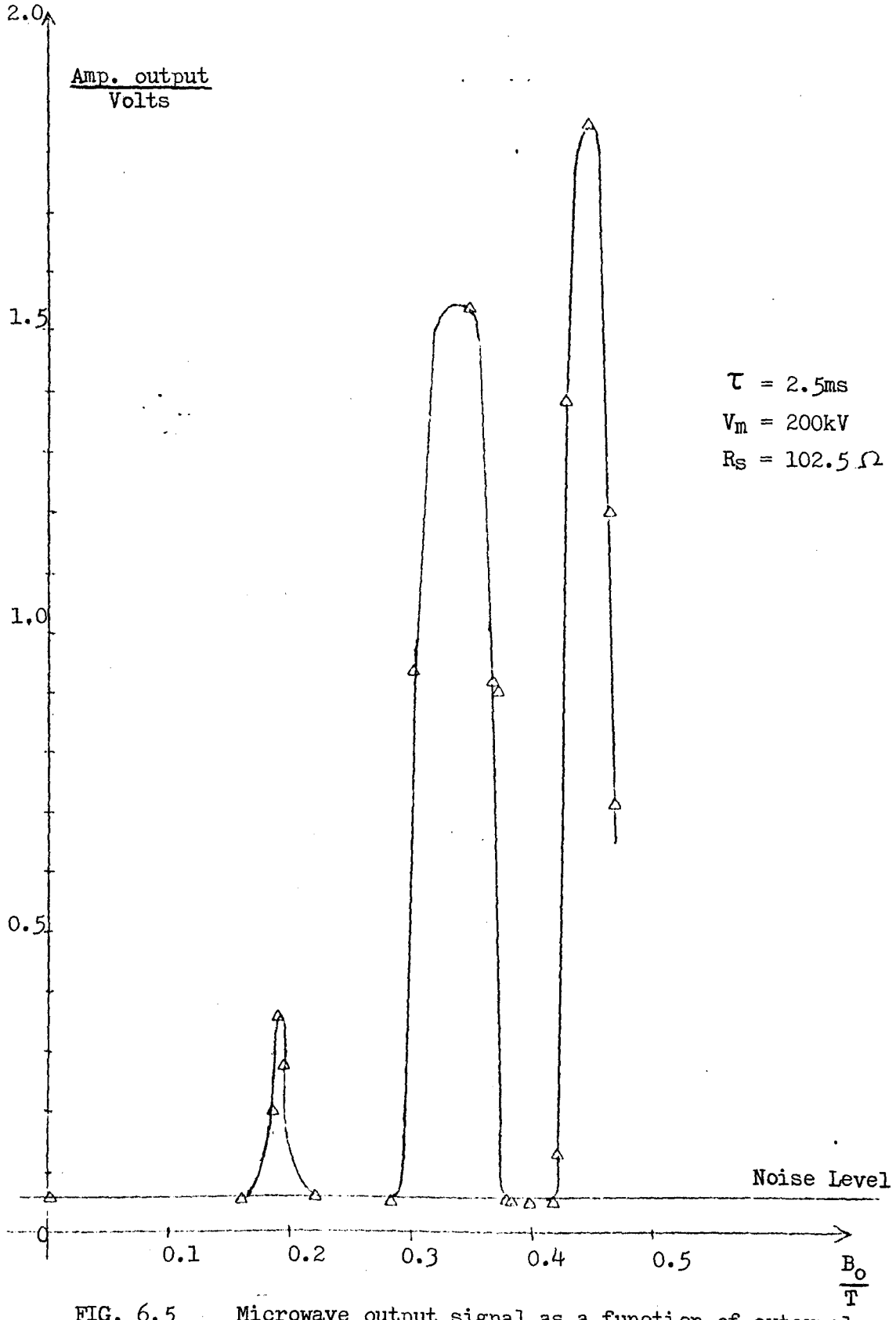

FIG. 6.5 Microwave output signal as a function of external magnetic field setting.

bank trigger pulse. By measuring the time interval between the appearance of the peak radiation signal level and the onset of the electron beam current the values of diode voltage at which the peak microwave power levels occurred were estimated to be approximately 67kV, corresponding to a γ factor of 1.13.

Using the calibration procedure described in section (4.6.5) the information of Fig. (6.5) was used to construct the variation in output microwave power with changing external magnetic field, this variation being shown in Fig. (6.6). Also shown in Fig. (6.6) are some experimental points which were measured at different values of τ. It is clear from Fig. (6.6) that microwave signal levels for the two resonances at the higher settings of external magnetic field are above the level at which the amplifier employed in the microwave diagnostic set up had a linear response. In order, therefore, to obtain a more realistic estimate of the absolute microwave power levels 30dB of attenuation was placed in the waveguide and the microwave output investigated with the external field setting varied between 0.291 T and 0.3325 T . The output obtained is shown in Fig. (6.7) which indicates peak powers of 75dBm (32kW).

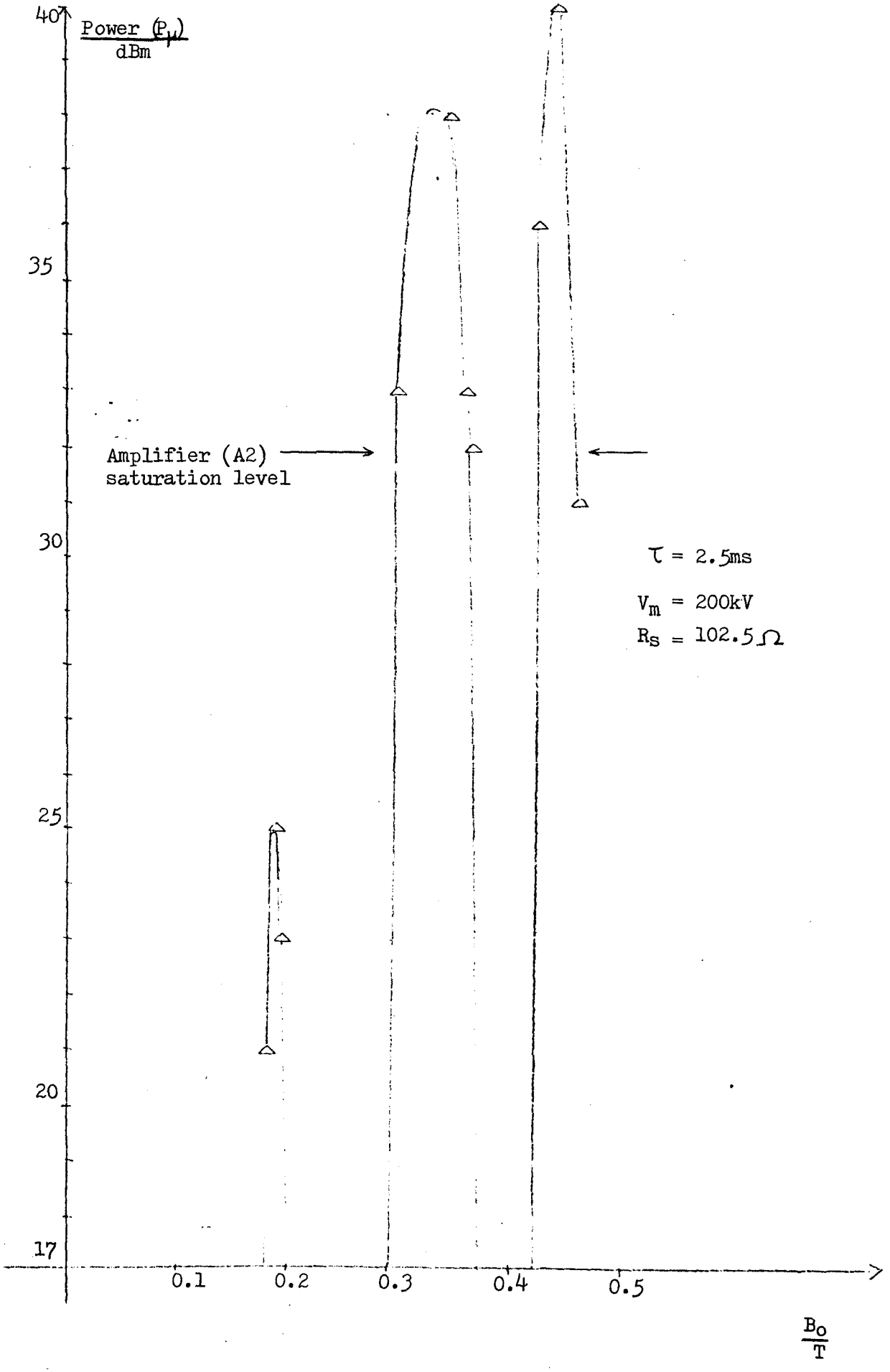

FIG. 6.6 Estimate of peak emitted microwave power levels, from Fig.(6.3) and "calibration" procedure of section (4.6.5.)

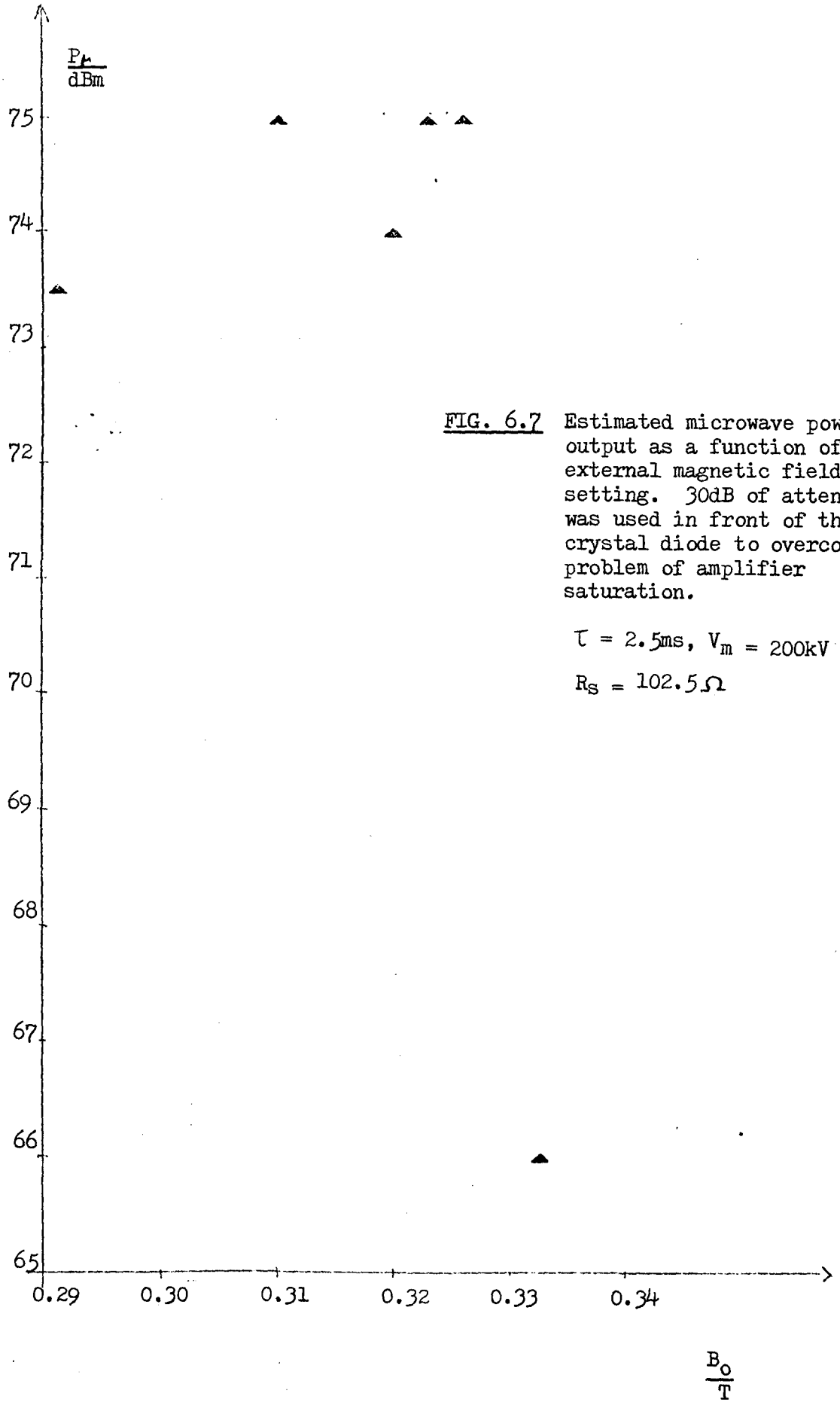

FIG. 6.7 Estimated microwave power output as a function of external magnetic field setting. 30dB of attenuation was used in front of the crystal diode to overcome the problem of amplifier saturation.

τ = 2.5ms, V_m = 200kV

R_S = 102.5Ω

6.4.1 Microwave Resonances

The appearance of the high levels of microwave emission at certain magnetic field values is assumed to be due to a resonant interaction between the electron cyclotron frequency, for the magnetic field employed, and some resonant mode of oscillation associated with the "cavity" in which the electron beam drifts. Bott [38], in his 1964 paper, proposed a similar explanation for the resonant emissions he observed in a cylindrical cavity.

The postulated cavity of this work is not easy to define accurately. Obviously the stainless steel collector would form part of a cylindrical resonator. The end caps may be considered to be the anode mesh, at one end, and the partially reflecting output window (or even the end of the collector), at the other end. The exact geometrical definition of such a cavity is further complicated by the wave length of the radiation involved ($\sim$3cm) as diffraction effects are likely to be important, so that strict definition of the cavity might include the presence of the conducting vacuum flanges at either end of the QVF tubing.

The microwave emission is then pictured as being due to the beam injection exciting electromagnetic oscillations in the cavity which in turn cause co-operative emission of radiation from the beam electrons at a frequency close to the Doppler shifted electron cyclotron frequency, forming a type of super-radiative maser.

The natural modes of oscillation of the cavity might be expected to satisfy a relation of the type,

$$\frac{\omega^2}{c^2} = K_z^2 + K_r^2 \qquad (6.3)$$

where ω is the angular frequency of these modes and K_z and K_r are the axial and radial wave numbers, dependent on the "length", l_c, and the radius, R, of the cavity respectively. The uncertainty in the value of the l_c makes it difficult to estimate a value for K_z. The axial wave vector, K_z, would presumably be related to l_c by the relation

$$K_z = \frac{n\pi}{l_c} \qquad (6.4)$$

where n is an integer associated with the longitudinal modes of oscillation of the cavity.

Linear theory predicts that the growth rate of the ECM instability will be maximised when the group velocity of the positive energy waveguide mode equals the axial beam velocity of the fast cyclotron wave mode[46]. This condition implies that the modes with greatest gain will be those whose cut-off frequency for the TE^{o}_{lm} mode will be close to the Doppler shifted cyclotron frequency or its harmonics, i.e.

$$\omega \gtrsim s\omega_{ce} + K_z v_z, \qquad (s = 1,2,3,\ldots) \qquad (6.5)$$

Simultaneous solution of equations (6.3) and (6.5) yield, for the emission frequency (for s = 1),

$$\omega = \omega_{ce}\gamma_z^2 \left\{ 1 \pm \beta_z \left[1 - \left(\frac{\omega_{co}}{\omega_{ce}\gamma_z} \right)^2 \right]^{1/2} \right\} \qquad (6.6)$$

where $\beta_z = v_z/c$, $\gamma_z^2 = (1 - \beta_z^2)^{-1}$ and $\omega_{co} = K_r c$.

In view of the above, the possible TE_{1m} modes (appendix 4) responsible for the observed microwave signals can be estimated from a knowledge of the cavity diameter (9.7cm) and the frequency of the emitted radiation. The emitted frequencies in these experiments may be evaluated from the measured values of the external magnetic field and relativistic electron mass (inferred from the diode voltage). Assuming that the radiation is emitted with frequencies close to ω_{co} then $(K_z c/\omega)^2 \ll 1$. Calculation then indicates that the TE_{42}, TE_{81}, TE_{23}, TE_{03}, TE_{13}, TE_{02}, TE_{61}, TE_{32}, and TE_{71} modes may have been excited.

The witness plate damage (section 5.5.1) indicates that the 5cm diameter beam propagates co-axially with the 10cm diameter drift tube. In view of this the spatial structure of the TE_{03} mode would be expected to couple strongly to the beam electrons. In addition, the azimuthal symmetry of TE_{omn} modes would indicate that these modes are more likely to be excited than, for example, TE_{11n} modes.

In order to change the cavity in which the ECMI was produced the length of the cylindrical collector was changed from 60cm to 104cm. While investigating the main resonance feature in detail a signal was observed at a magnetic field of 0.291T, which was below any setting at which the resonance had been seen before. Indeed previously this setting had shown no signal above the noise level. The sharpness of the skirts of the main resonance is illustrated in plate (6.3) where a healthy microwave signal is reduced to zero with a change of magnetic field by < 0.2 per cent. A digital frequency meter indicated that the setting of τ was extremely stable over a long period of time and that this was not an alternative reason for the change in the lower cut-off of the resonance. This change in the resonance with an alteration in cavity length lends credence to the idea of the microwave emission being due to a resonant interaction.

Although, as has been stated, it is difficult to define the proposed cavity with which the beam interacts it is clear that altering the length of the collector-anode will change the length, l_c, of the cavity. In view of this, and considering the interaction as a resonant one it is clear that a particular mode will occur at a different frequency for the longer collector length.

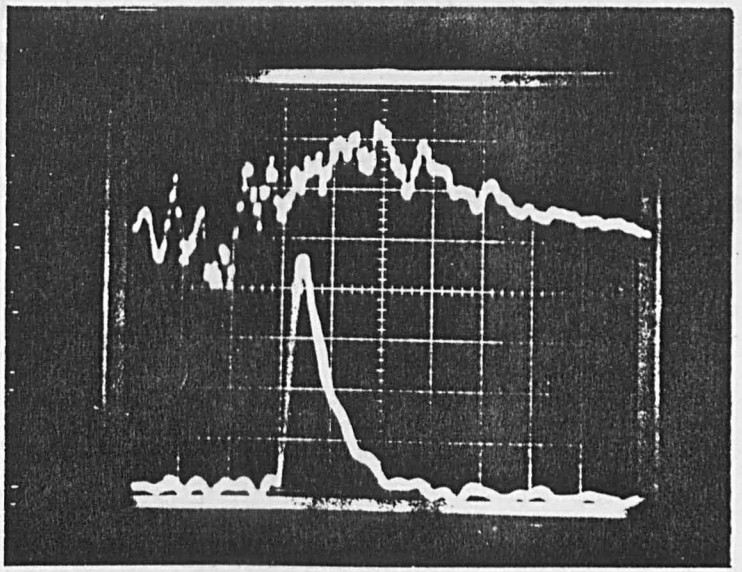

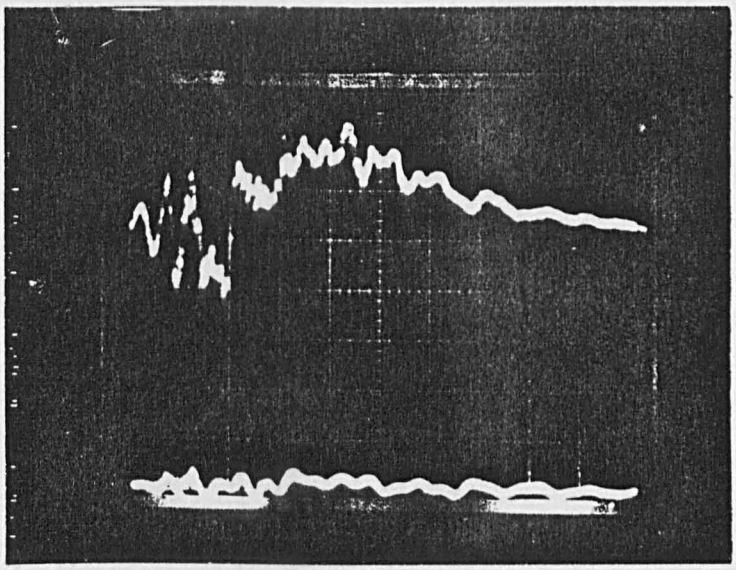

Plate 6.3 The photographs above illustrate the change in output microwave signal as a result of a 0.2% change in magnetic field setting. P_μ = 1.6 W

Top traces for both photographs are electron beam current (7.7A/div). Bottom traces are microwave signal. $P_\mu \lesssim 8$ mW.

Time-base 200ns/div.

It was noted that the observed beam current did not alter with the change in the length of the collector-anode. This observation would imply that the magnetic flux lines around which the beam electrons spiralled all terminated on the extent of the original collector length and that no charge was being "dumped" on the QVF tubing or vacuum flanges.

6.4.2 Resonance Linewidth

A number of factors may have contributed to the width of the resonant features exhibited in Fig. (6.5). The condition necessary for production of the ECM instability is that the mismatch frequency, $\Delta\omega$, should be close to zero, where $\Delta\omega$ is given by

$$\Delta\omega = \omega_r - (\omega_{ce} + K_z V_z) \qquad (6.7)$$

where ω_r is the resonant frequency of one of the cavity eigenmodes which has an electric field transverse to the direction of beam propagation.

The spatial variations in the axial magnetic field strength will mean that different electrons will have had different electron cyclotron frequencies and so one might expect there will be electrons resonant with the cavity over a range of voltage settings for the magnetic field bank.

In addition, it is obvious from (6.7) that any velocity spread among the electrons will result in the mismatch condition being met at varying values of the external magnetic field. Space charge potential depression across an annular beam will result in a spread in the relativistic mass factor of the beam electrons so resulting in slightly different values of ω_{ce}. The

electrostatic potential drop, ϕ_B, across an annular beam is given by the third term on the right-hand side of (5.8), i.e.,

$$\phi_B = \frac{I \quad \ln (b/a)}{2\pi\epsilon_o\beta c \quad (b^2/a^2 - 1)} \tag{6.8}$$

Despite the use of an anode mesh which limited the axial beam temperature, variations in axial electron velocity may be expected as they are correlated to variations in the perpendicular velocity of the electrons which are "born" and finally impinge on real electrodes after passing through conservative fields. Thus for any fixed value of external magnetic field there will have been a spread in the value of the Doppler shifted electron cyclotron frequency and so, for a given cavity mode, there may be resonant electrons even if there is a small shift in the external magnetic field.

Examination of the oscillograms obtained shows that the time interval between the appearance of the electron beam and the microwave radiation signal is different for different values of the external magnetic field.

Fig. (6.8) shows the time interval between the onset of the electron beam current and the occurrence of the peak level of the radiation signal plotted against the magnetic field strength for some of the settings within

FIG. 6.8

The time interval, Δt, between the onset of the e-beam current and the occurrence of the peak level of the microwave signal for different magnetic field settings (V_m = 210kV for all points).

τ = 2.5ms

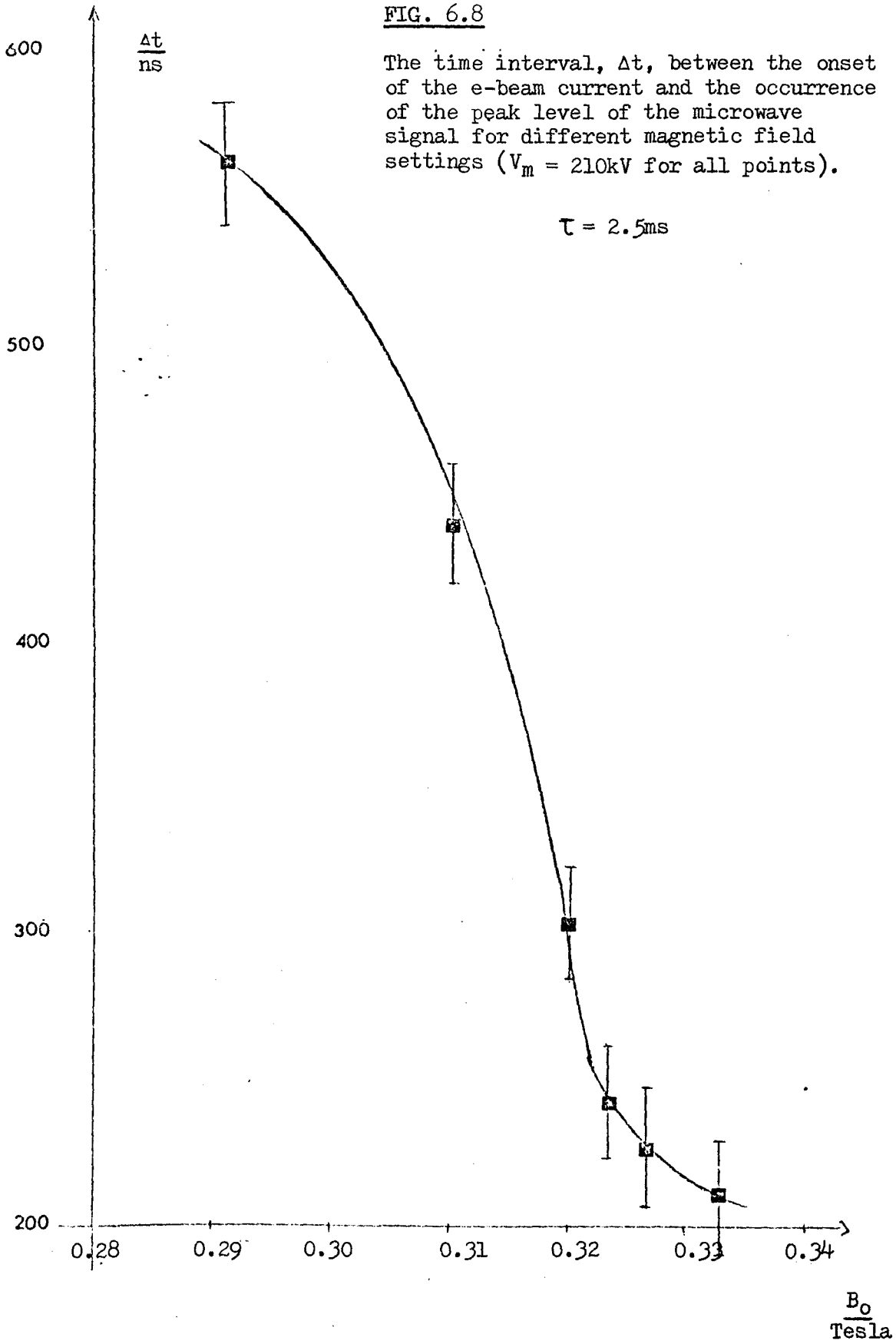

the resonance centred around B = 0.3T.

It can be seen that the higher magnetic field settings result in the radiation signal appearing earlier, at a time when the diode voltage, and hence electron energy, were larger. Note that the appearance of the radiation signal is always after the peak diode voltage signal and hence the electron energy is decreasing with time. Despite the fact that both B and γ are decreasing with time there is no firm suggestion that the width of the resonance is due to constancy of the relativistic cyclotron frequency. The percentage change in B, from Fig. (6.8) is 14%, whereas, although the diode voltage changes by a factor of two, the percentage change in γ is approximately 3%. Whether or not the value of the Doppler shifted electron cyclotron frequency is remaining constant would depend on the value assumed for K_z. Although the change, ΔV_z, in the axial velocity with time is great the value of $K_z \Delta V_z$ is likely to be only a few per cent of ω_{ce}, assuming $K_z = \pi/l_c$.

The data employed in plotting Fig. (6.8) was obtained for Marx bank voltage settings of 210kV. In addition, the shots from which the data was extracted were successive shots to ensure that the diode performance would not differ during the collection of the information (see later). The value of B is, of course, effectively constant during the period of A-K gap closure.

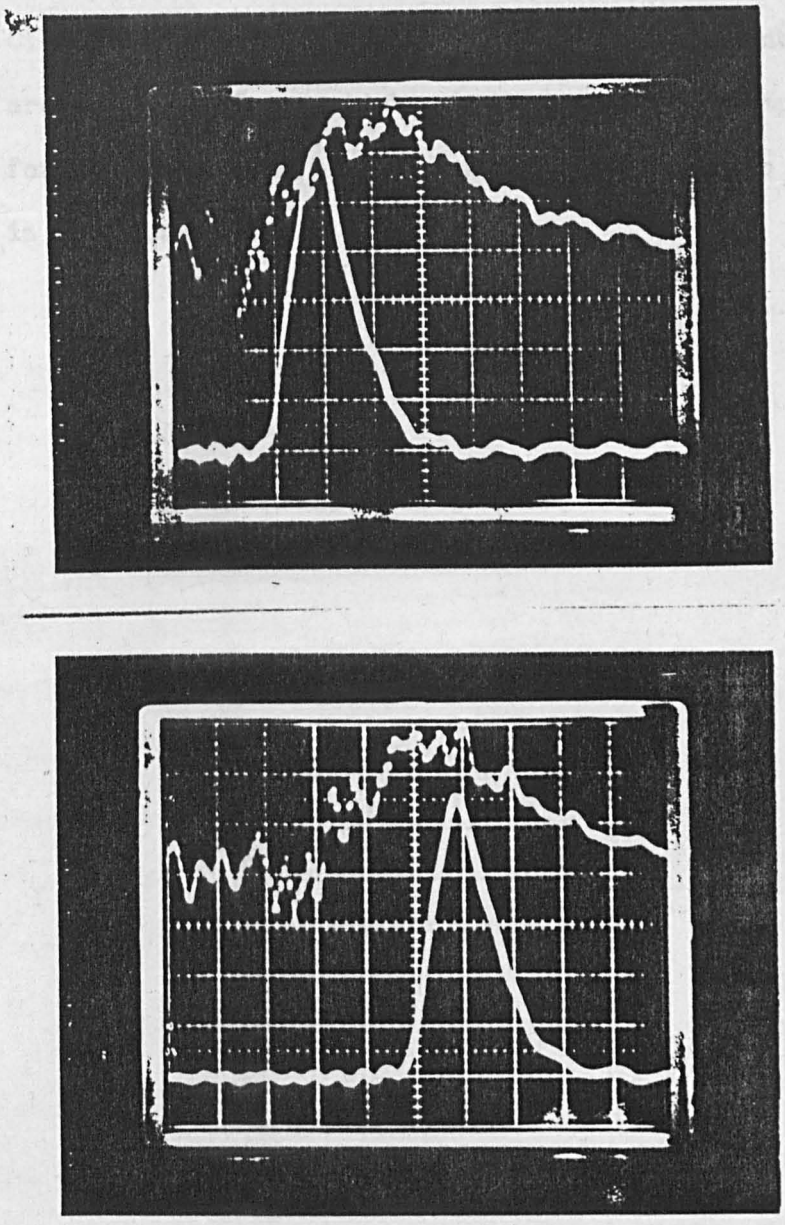

Plate 6.4 An illustration of the change in time between the rise of the beam current and the appearance of the microwave signal for different magnetic field settings.

Top: Magnetic field set for 0.332T.
Top trace is beam current (7.7A/div)
Bottom trace is microwave signal. P_μ = 32 kW

Bottom: Magnetic field set for 0.291T.
Top trace is beam current (7.7A/div).
Bottom trace is microwave signal. P_μ = 22 kW

Both shots at Marx setting of 210kV
Time-base at 200ns/div

Calculation shows that over a period of 2 μs centred around τ = 2.5 ms, which was the value of τ employed for this work, the percentage change in magnetic field is less than 0.1%.

6.5 Microwave Signal Pulse Width

All recorded microwave signals are of course the spectral sum of all received frequencies above the cut-off frequency of the X-band waveguide (6.57 GHz). Despite the variations in magnetic field values the widths of the detected radiation pulses are generally the same. The duration of the radiation signal will depend upon the values of both the diode voltage and beam current. The diode voltage must be sufficiently high to give the beam electrons a minimum value of transverse velocity so that there will be free electron energy for microwave radiation production. In addition the diode voltage must be sufficiently large to make the frequency mismatch close to zero.

As the radiation signal is sometimes seen to rise simultaneously with the electron beam current it is apparent that the fraction of current which is "resonant" is always sufficiently large to produce radiation. Early work on CRMs produced radiation with milliamp currents, although these currents had a much greater percentage of the beam in resonance with the magnetic field [37].

Many of the microwave traces featured a double peaked appearance with the temporal separation of the peaks being typically two hundred nanoseconds (Plate 6.5). Dispersive waveguide elements were used as a spectral

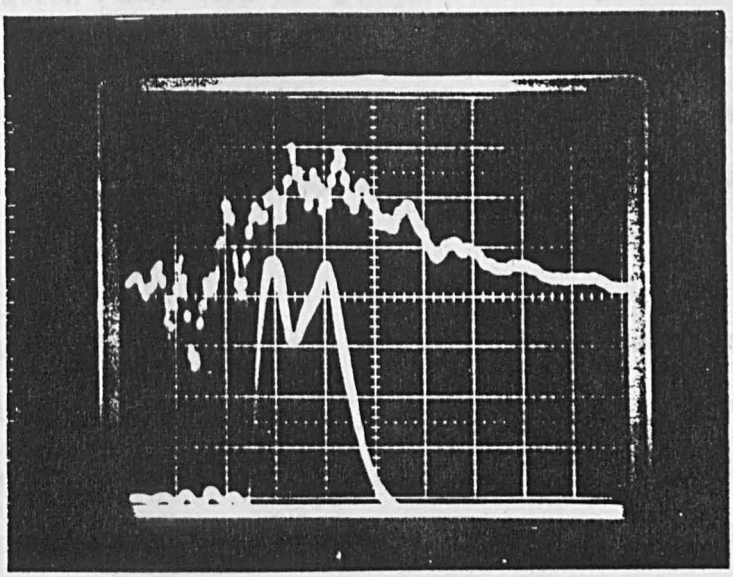

Plate 6.5 Bottom trace shows the appearance of a microwave signal with a double peaked trace.

Time-base at 200ns/div.

Magnetic field setting at 0.306T

analyser by Nation [70] for X-band detection, the waveguide separating out different frequencies through their different propagation times down the guide. However, for the length of waveguide employed here, the separation of the peaks could not be due to waveguide dispersion (unless one peak was due to radiation extremely close to the cut-off frequency).

As the beam drift tube was not much larger than the length of waveguide employed and the transverse dimensions of the cavity were large it was assumed no appreciable dispersion of detected radiation occurred in the drift tube.

6.6.1 Harmonic Emission

The smallest resonance featured in Fig. (6.5) is centred around B = 0.194T and appeared when the electron's relativistic mass factor, γ , was equal to 1.129 thus indicating an electron cyclotron frequency of, at most, 4.81 GHz. Assuming K_z to be given by equation (6.5) with n = 1 and l = 0.6m then the emission frequency would be 4.93 GHz.

As this frequency is below the cut-off frequency for the X-band waveguide the possibility exists that this resonance is due to the resonant interaction between a cavity mode and a harmonic of the electron cyclotron frequency.

The possibility that the microwave signal received at the magnetic field setting of 0.194T was due to an evanescent wave at a frequency of 4.93 GHz can easily be ruled out by calculation using the relations below.

$$K_g^2 = K_o^2 - K_c^2 \qquad (6.9a)$$

$$P_R = P_I \exp(2iK_g z) \qquad (6.9b)$$

where K_g is the guide wavenumber, K_o is the free space wavenumber and K_c is the cut-off wavenumber. The ratio P_R/P_I , the power received on the microwave crystal to the power entering the X-band waveguide, gives a value of $\simeq 10^{-28}$.

The small magnitude of this ratio indicates that the signal is more likely to be due to harmonic emission.

6.6.2 Ka-Band (26.5 GHz - 40 GHz) Measurements

Having observed radiation which appeared to be a harmonic of the fundamental electron cyclotron frequency it was decided to check for emission of radiation at higher frequencies than X-band. To this end the X-band detection system was replaced with a Ka-band (Q-band in U.K. designation) receiver horn and crystal diode detector, and the magnetic field coil was fired at values varying from 0.387T to 0.467T.

The first observations of radiation using the new microwave diagnostics showed traces with long "tails" on them which illustrated large output signals for times exceeding five microseconds, much longer than the diode voltage pulse width. The possibility that this high frequency signal was due to high frequency waves other than ECM waves was excluded by firing the diode with no applied magnetic field, a condition which never resulted in any detected signal. Therefore, the observed trace obviously required the presence of both the electron beam and the magnetic field.

A pulsed Gunn diode source of Ka-band radiation gave a square wave output from the Ka-band detection system with the amplifier of section (4.6.5) removed. However, with the amplifier occupying its normal place, between the r.f. crystal and the oscilloscope, the output trace contained long tails. This indicated that the later

part of the traces seen during the beam-field interaction was the result of a diagnostic temporal response problem. The 1MΩ input resistor of the amplifier was subsequently replaced by a 1kΩ resistor which resulted in the removal of the long tails observed on the output pulse from the Gunn diode.

The Ka-band signals observed, although much lower in power than the X-band signals were still well above the powers expected from harmonics of the incoherent cyclotron emission process. Ka-band powers approximating to 10 watts were seen at a magnetic field of 0.463T. The ECR frequency for such a field in the reference frame of the laboratory would be 11.5 GHz (for $\gamma = 1.13$) which is well below the cut-off frequency of the Ka-band waveguide (21.08 GHz). Whether or not this indicates that the microwave signals are the result of the first harmonic of the cyclotron frequency would again depend on the magnitude of the Doppler shift although it seems likely that this trace must be the result of harmonic emission. As others have observed, the conversion of beam power to microwave power at harmonics of the fundamental cyclotron frequency is with poorer efficiency than at the fundamental frequency [71].

High frequency radiation has been generated by backscattering electromagnetic radiation from a relativistic

electron "mirror" resulting in a Doppler upshift of the incident radiation frequency [72]. The scattered radiation frequency, ω_s, is given in terms of ω_i, the incident frequency, by

$$\omega_s = (1 + \beta)^2 \gamma^2 \omega_i \qquad (6.10)$$

yielding a Doppler upshift factor of typically 2.7 for the experiments discussed here. Although such Doppler upshifted frequencies could be detected by the Ka-band detector it would seem unlikely that this mechanism could have been responsible for the observed signals as the beam currents and geometry indicate an electron beam plasma frequency which would be too low to efficiently scatter microwave radiation reflected back into the cavity from the output window. In addition, the hollow beam would not be the ideal profile to act as a relativistic mirror.

6.7 Polarisation Measurements

The polarisation analyser, discussed in Chapter Four, was employed to measure the relative microwave signal field strength in the X and Y directions of Fig. (6.9). The conducting rods of the analyser were placed in front of the X-band receiving horn parallel to the X direction and the maser fired in order to record the subsequent microwave signal. The experiment was repeated with the polarising rods rotated through ninety degrees and with all other parameters (I_{max}, τ , V_m , attenuation) kept the same, a condition which resulted in the absence of any microwave signal. In this configuration the rods would absorb the electric field vectors perpendicular to the broad wall of the waveguide while the electric field vector perpendicular to the waveguide narrow wall could not propagate down the waveguide.

By rotating the waveguide through ninety degrees and leaving the polarising rods parallel to the Y direction the original microwave signal was restored and was seen to be of the same magnitude. Subsequently, rotating the conducting rods back through ninety degrees and maintaining the orientation of the waveguide the microwave signal again disappeared, except for a small signal thought to be due to the waveguide rotation being not quite 90^{o} from its original orientation. On all shots the beam current trace was the

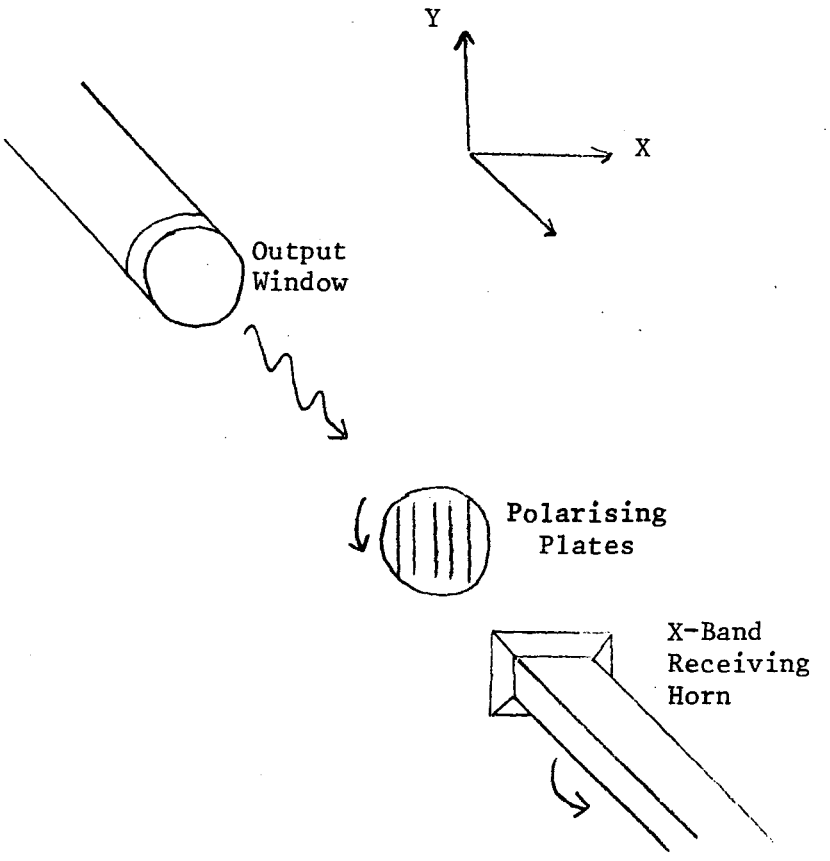

Fig. 6.9

SCHEMATIC ARRANGEMENT FOR POLARISATION MEASUREMENT

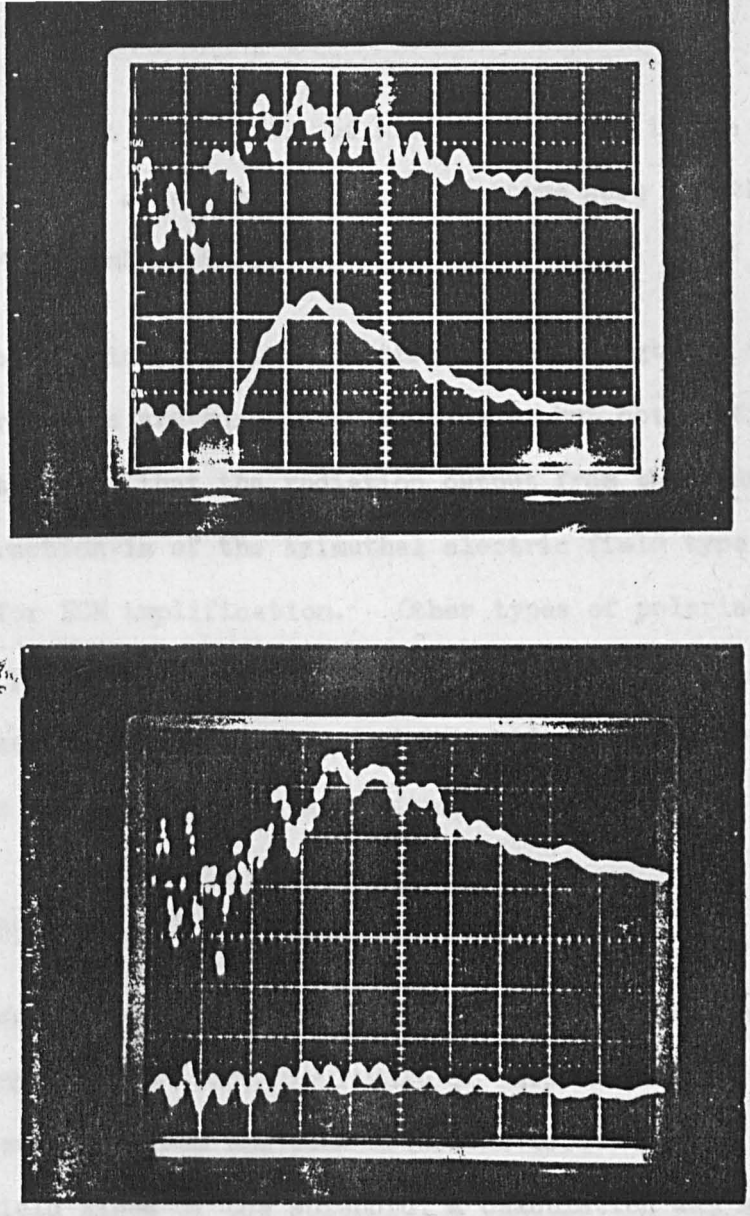

Plate 6.6 The above photographs were taken for identical conditions of Marx voltage, magnetic field setting and microwave power attenuation. The top traces are e-beam current and clearly are nominally the same.

The change in the microwave signal between shots is the result of a change in the orientation of polarising plates with respect to the microwave receiving horn (section 6.7).

same ensuring that the absence of microwave traces in the second and fourth arrangements discussed above were not the result of Marx bank misfire.

The observation that the electric field strength in the X and Y directions are equal is a necessary, but not sufficient, condition to prove that the radiation output from the beam-field interaction is of the azimuthal electric field type predicted for ECM amplification. Other types of polarisation would have produced the same result and in order to completely characterise the output radiation phase shifters (quarter wave-length plates) would have been required.

6.8 Magneto-Bremsstrahlung Power Calculation

In order to exclude the possibility that the microwave traces being detected were the result of incoherent cyclotron emission from the beam electrons orbiting the magnetic field lines of the solenoid, a calculation was made on the upper-limit that this "magnetic-bremsstrahlung" radiation might be expected to contribute to the microwave signal.

The total power, P_T, emitted in all harmonics from a single relativistic electron in a static magnetic field, B, is given by [73],

$$P_T = \frac{e^4 B^2}{6\pi\varepsilon_o m_o^2 c} \left[(1-\beta_z^2) \left[\frac{E}{m_o c^2} \right]^2 - 1 \right] \qquad (6.11)$$

This equation was used, in conjunction with the total number of estimated beam electrons, to provide an "order of magnitude" value for the gyromagnetic radiation level. The number of beam electrons contributing to the process was estimated in two fashions. Firstly, the electron beam current diagnostic had a passive RC integrator (RC = 20.68 μ s) connected to it before going into the oscilloscope amplifier. The resulting trace gave a value for the total charge impinging on the drift tube collector.

As a cross check on the value obtained above the area under the "I_B-time" trace was estimated. This estimate was made over all appreciable beam current (before gap closure) and is therefore an upper estimate as not all electrons will contribute to cyclotron maser radiation. The two values of charge so obtained agreed within a factor of two and indicated a total electron charge $\lesssim$ 13 μC.

In calculating P_T from equation (6.11) the value of E was chosen to be that appropriate to the peak diode voltage for the shot in question and all electrons were assumed to have $\beta_z = 0$. In addition, the value of B used in the calculation was the maximum value of B "seen" by any electron for the same shot (0.33T). All of these assumptions, although clearly incorrect, ensure that the estimate of the incoherent radiation level will be an upper estimate. The resultant estimate obtained was 40 milliwatts.

The above value of gyrotropic power level is that which would be emitted by the electrons in all directions. As the electrons in question are only mildly-relativistic ($\beta < 0.5$), the polar pattern of the radiation would be expected to have an angular distribution, $dP/_{d\Omega}$, for which [34],

$$\frac{dP}{d\Omega} \quad \alpha \quad (1 + \cos^2\theta) \qquad (6.12),$$

where θ is the angle between the direction of the magnetic field and the direction of observation. Thus, not all of the emitted incoherent radiation would necessarily impinge on the microwave receiving horn.

The calculated value of 40mW should be compared with an observed microwave signal of 12.5kW for the conditions of this particular shot.

Therefore, even the estimated upper-limit to the magnetic bremsstrahlung radiation, assumed to be all in the forward direction, would still be five orders of magnitude below the measured signal level, lending support to the assertion that the observed signals are due to a co-operative emission process.

6.9 Microwave Power Measurements at Higher Beam Powers

In order to study the microwave power output at increased electron beam powers the Marx bank was operated at voltages varying between 200 kV and 350 kV. The resulting increase in the maximum achieved diode voltage over this operating range was approximately 30%. However, the electron beam currents in the drift tube were observed to increase by a factor of two along with increasing diode currents (see later). With the external magnetic field setting kept constant (B = 0.33T) the microwave radiation output was plotted against the instantaneous value of the electron beam power, obtained by measurement of I_B and V_D at the same instant at which the radiation signal was at a peak. Fig. (6.10) shows the variation in microwave output power with increasing pulsed beam power. The apparently obvious result that the microwave output power increases with increasing beam power is not so readily predicted as some devices operating on the principle of the ECM instability illustrate that increasing space charge effects, due to increasing gun current, can be detrimental to efficient operation of the cyclotron maser [45].

Fig. (6.11) shows the "instantaneous" device efficiency, $\eta = (P_\mu / I_B V_D)$, plotted against increasing beam power and shows that there is an increase in the relative efficiency over the Marx voltage settings employed. The error in the absolute value of P_μ makes it difficult to estimate the

FIG. 6.10 Change in peak output microwave power level as a function of increased beam power (P_B) level, obtained by operating at increasingly higher Marx voltage settings.

External magnetic field setting = 0.323T

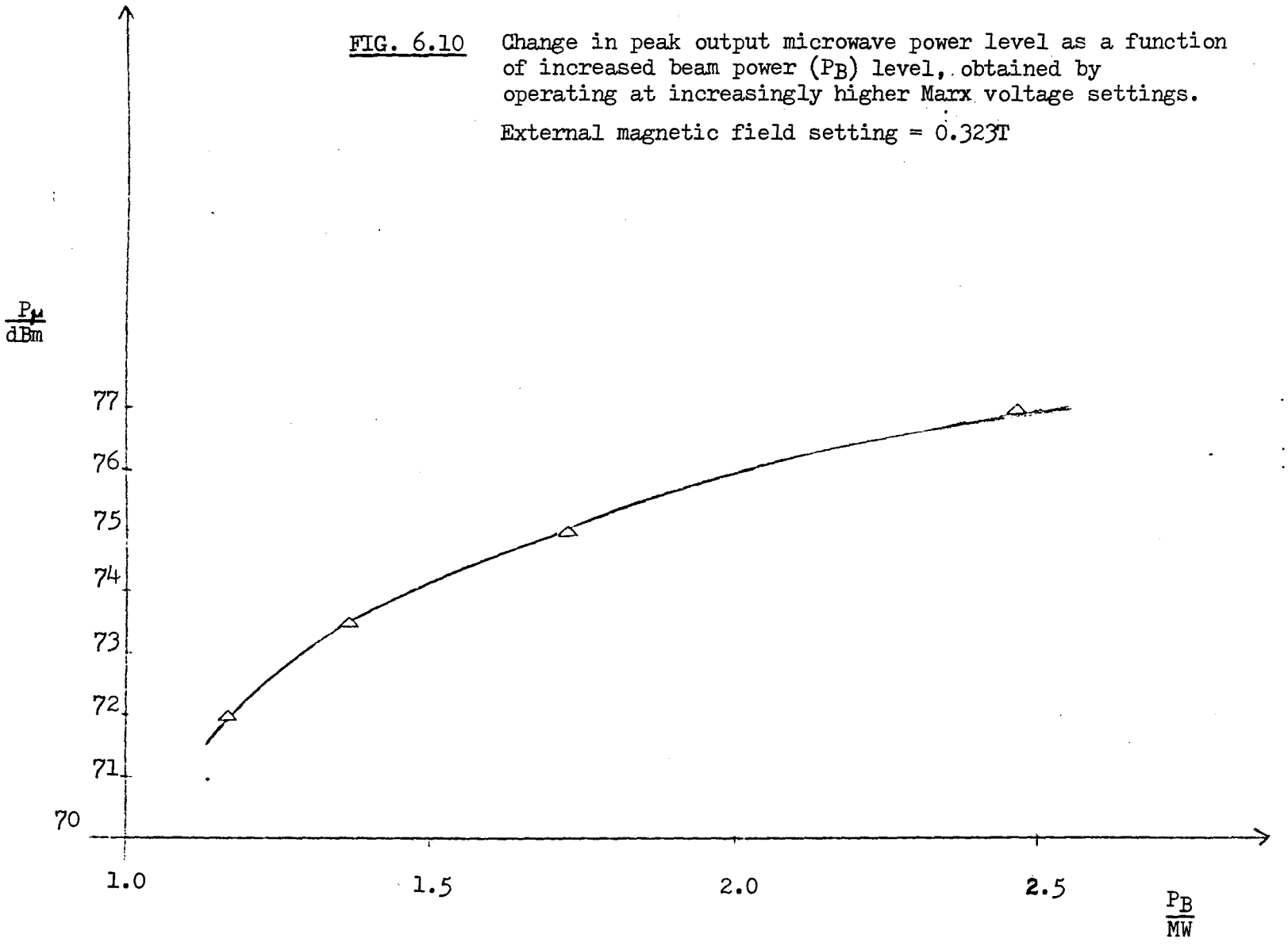

FIG. 6.11

"Instantaneous" device efficiency, η, as a function of increasing beam power. η was calculated from data of fig. (6.10).

$B_o = 0.323T$

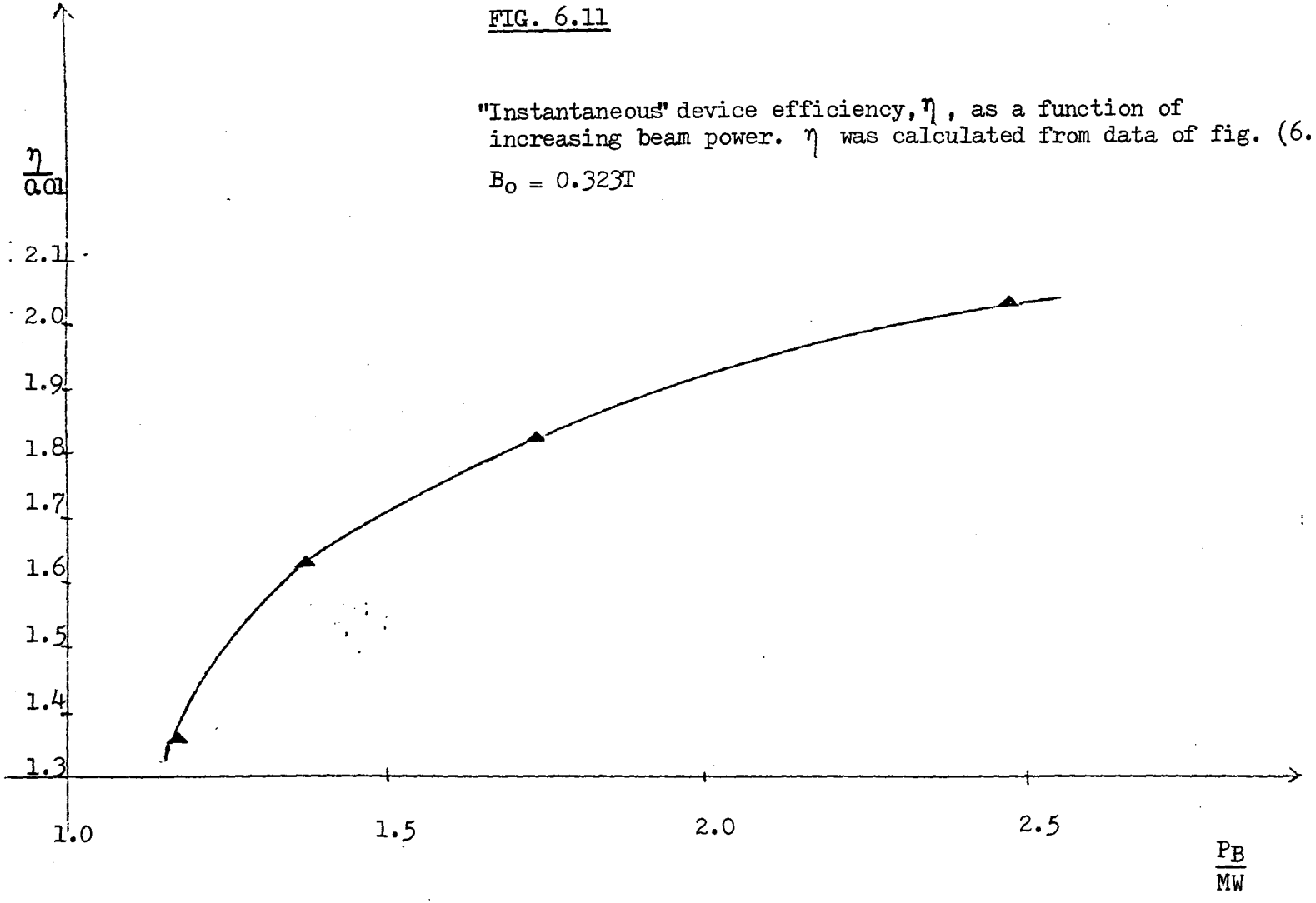

absolute value of the efficiency but a value of (2 ~ 3)% appears reasonable.

For a single shot the ratio of the time integrated microwave power to the time integrated product of I_B and V_D gave a ratio of approximately 0.005.

6.10 Changes in Diode Behaviour

The electrical behaviour of the REB diode during the experiments on microwave generation was different from that during the experiments discussed in Chapter Five. Two occurrences were thought to be responsible for this change. Firstly, after having failed to properly create an electron flow through the A-K gap at a gap spacing of 50mm all of the field-grading rings (Chapter Two) were removed from the diode.

The removal of the field-grading rings had the effect of diminishing the extent to which the gap could be considered planar and, as can be seen from Plate (6.7), resulted in current flow in the gap at lower values of diode voltage (for a given gap setting). In addition to impedance collapse beginning at lower diode voltages the diode voltage profile is seen to be flatter around its peak value.

The second change in the diode performance was due to a slow, continuous change in the cathode emitter as a result of repeated use of the diode. Visual inspection of the cathode tip indicated that the large diode currents had resulted in some wear of the sharpened cathode surface. Refurbishing of the cathode tip seemed to indicate a slightly larger beam current for a given diode operating condition, indicating that cathode surface wear may have caused a slight change in the diode current over a large number of diode shots.

(I)

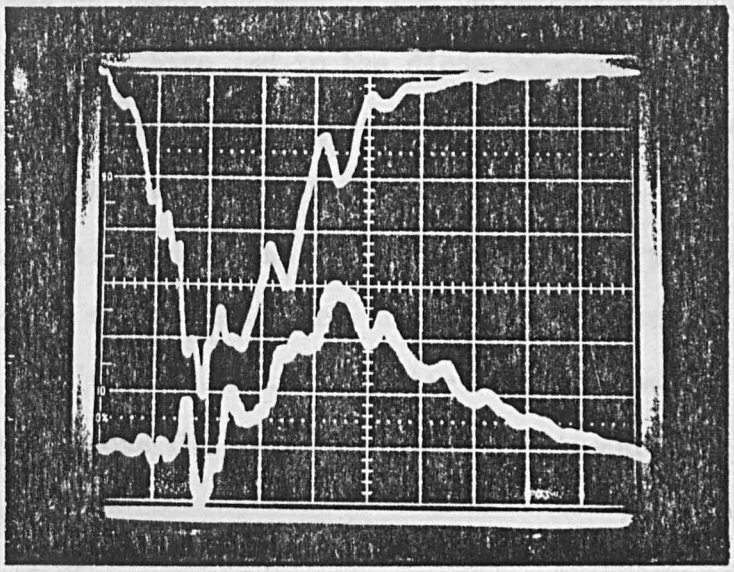

(II)

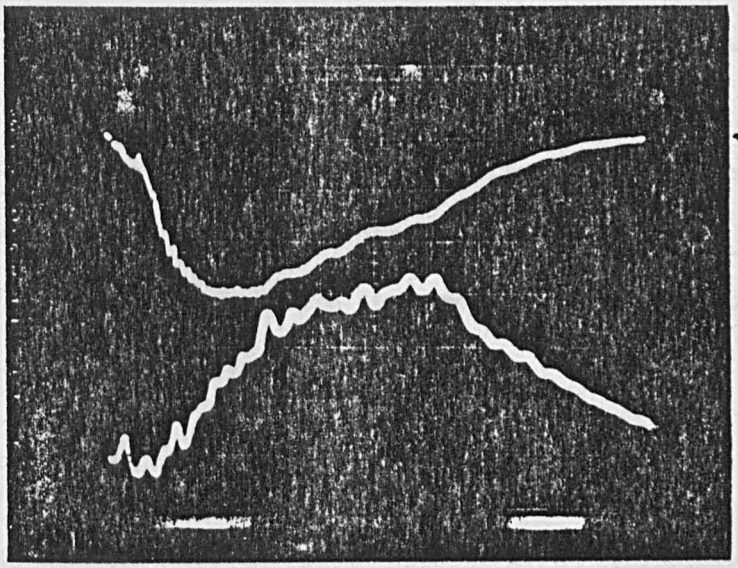

Plate 6.7

Diode voltage and beam current traces before (I) and after (II) the removal of the field grading rings.

Top traces: Diode voltage (23kV/div).

Bottom traces: Electron beam current

R_s = 102.5Ω, g = 3cm.

The effect of these changes in the performance of the diode is presumed to have led to the diode impedance collapse observed while investigating the microwave radiation output at the higher values of Marx voltage setting. As was discussed in section (6.9) the higher Marx settings produced little change in the maximum value of the diode voltage (consistent with the argument of Chapter Five), however, large changes in both the Marx current and diode currents were observed.

This Marx setting dependent behaviour of the REB diode is presumed to be responsible for the higher electron beam currents which produced increased microwave radiation power. The failure of the increased Marx voltage settings to significantly alter the electron energy is reflected in the microwave resonance region appearing at the same magnetic field setting as for the lower Marx voltage settings.

6.11 Magnetic Field - Beam Current Variations

While checking to see if the microwave signal was really dependent on the presence of the magnetic field it became apparent that the beam current was also varying with the magnitude of the magnetic field. Shots with and without the application of the external magnetic field illustrated not only the disappearance of the microwave radiation but also a drastic change in the magnitude of the drift chamber beam current. Subsequent shots at varying magnetic field settings illustrated a gradually decreasing beam current with increasing magnetic field, Plate (6.8).

The value of beam current was plotted against the magnetic field, keeping τ the same. In order to keep other conditions the same the value of beam current used in the plot was that occurring 320 nanoseconds from the start of the beam trace with the Marx voltage setting kept at 210 kV. As was discussed in Chapter Five, the diode voltage trace was unaffected by the presence of the magnetic field and the good diode voltage reproducibility will have ensured that the different beam magnitude was a result of the different applied fields.

As a result of the noisy appearance of the e-beam trace two graphs were plotted to illustrate the beam current - magnetic field relationship. Fig. (6.12a) is drawn with the "raw" or instantaneous value of I_B, while Fig. (6.12b) is

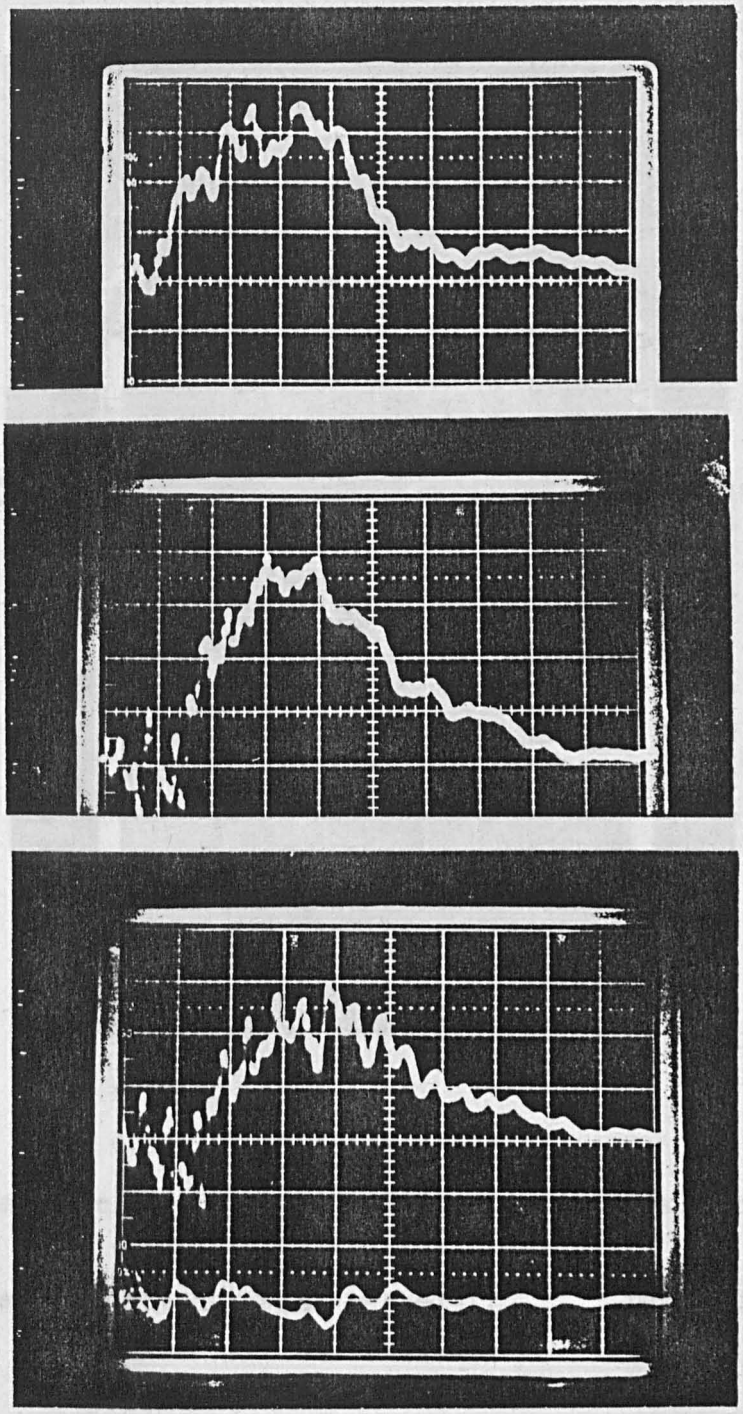

Plate 6.8 (a)

Top: Magnetic field setting = 0, beam current (38A/div)

Middle: Magnetic field setting = 0.193T, beam current (7.7A/div)

Bottom: Magnetic field setting = 0.290T, beam current (7.7A/div)

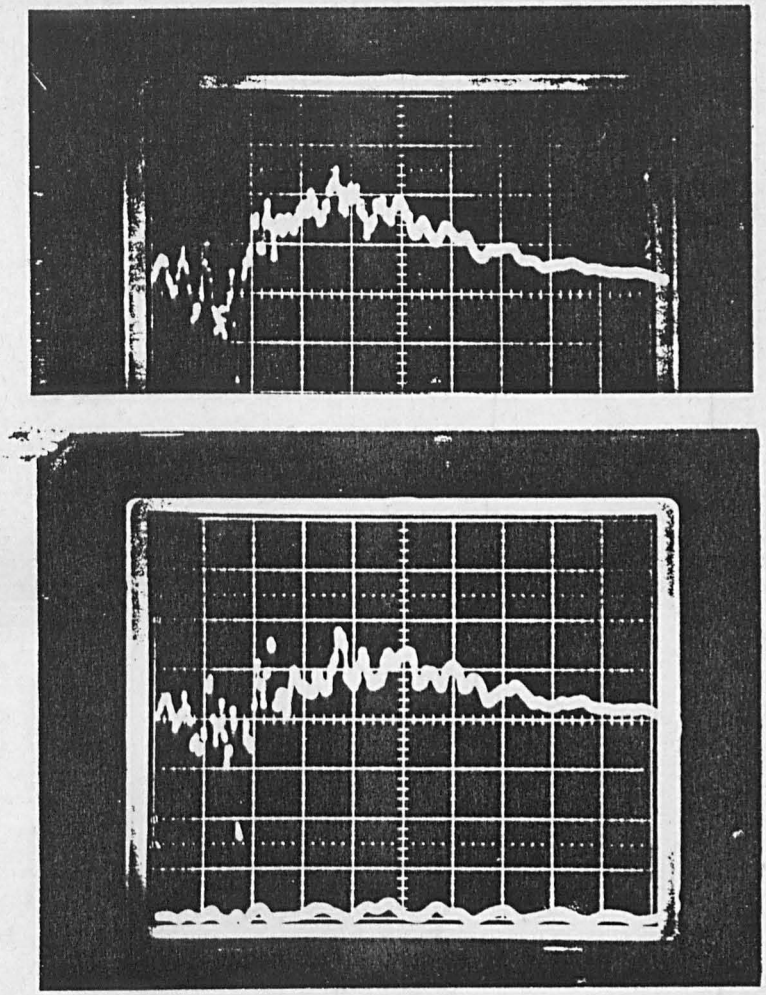

Plate 6.8 (b)

Top: Magnetic field setting = 0.355T, beam current (7.7A/div)

Bottom: Magnetic field setting = 0.419T, beam current (7.7A/div)

Plates 6.8 (a) and 6.8 (b) illustrate the decrease in the beam current trace at increasing magnetic field settings.

All shots had Marx voltage setting of 200kV and the time-base is at 200ns/div.

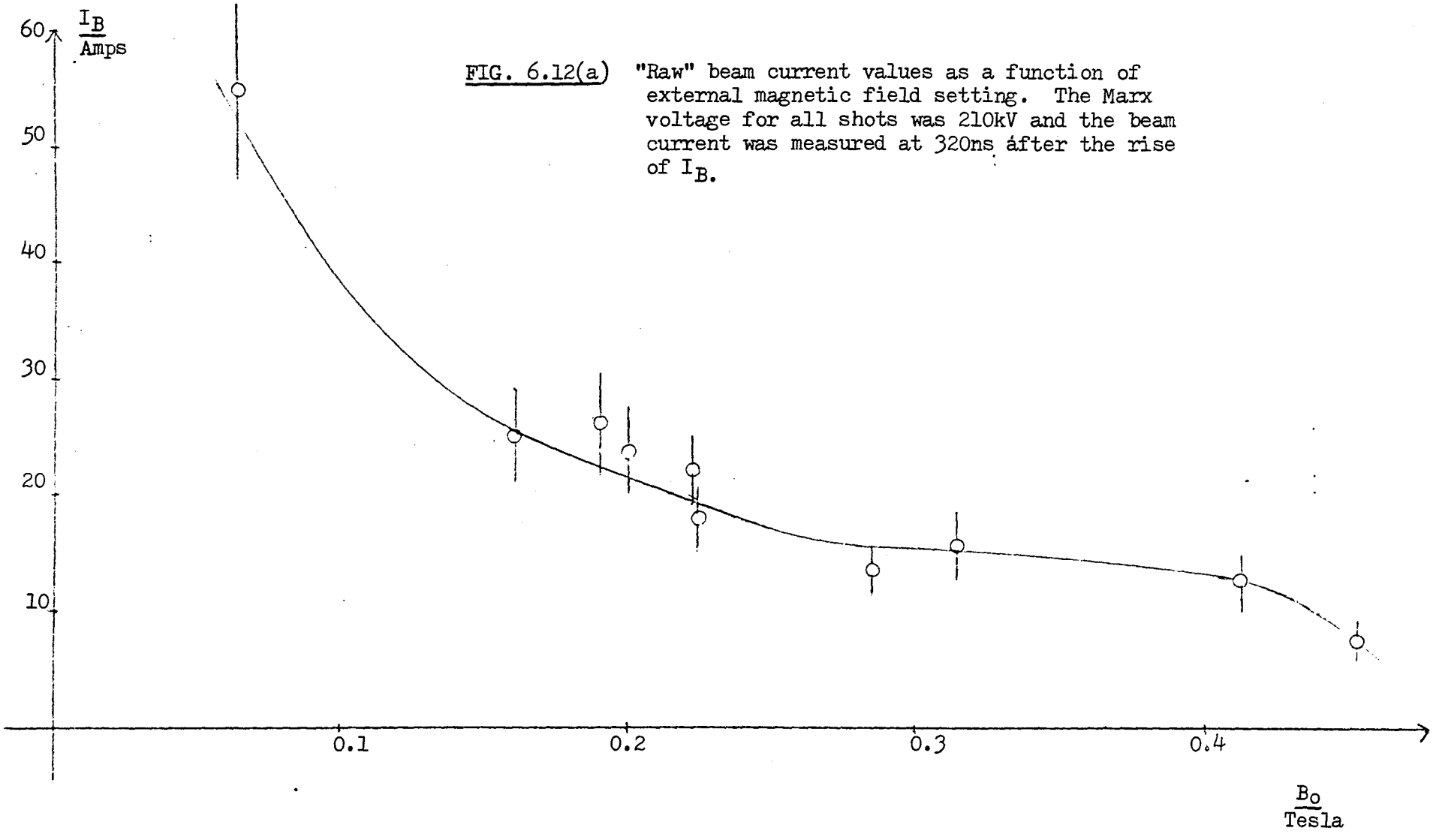

FIG. 6.12(a) "Raw" beam current values as a function of external magnetic field setting. The Marx voltage for all shots was 210kV and the beam current was measured at 320ns after the rise of I_B.

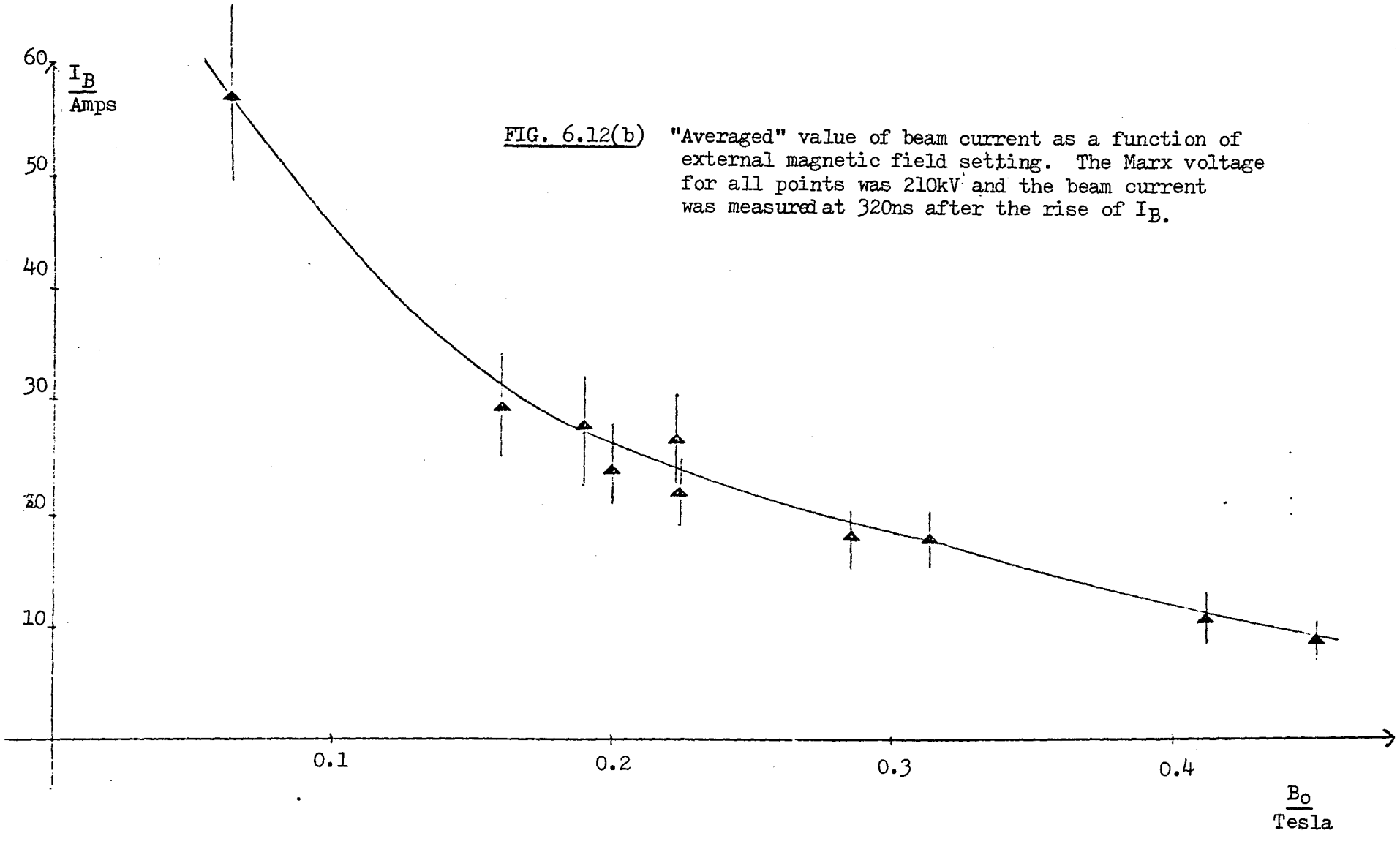

FIG. 6.12(b) "Averaged" value of beam current as a function of external magnetic field setting. The Marx voltage for all points was 210kV and the beam current was measured at 320ns after the rise of I_B.

drawn with the "smoothed out" value of I_B obtained by averaging through the oscillations which ride on top of the main trace.

Fig. (6.12a) shows a monotonically decreasing value of I_B for an increasing B. However, even within experimental error Fig.(6.12b) shows slightly high currents for certain experimental points. If the oscillations can be assumed to be spurious, then the variation of the smoothed current values with B might be explained by the possibility that the electrons are undergoing magnetic mirroring due to the rising axial magnetic field seen by the electrons on entering the drift tube. As discussed in Chapter One, other workers have employed this technique to control the ratio of axial to transverse electron energy.

If the oscillations on the electron beam trace are not spurious but are the result of some real phenomena, for example, some reflexing effect, then the apparent failure of the raw current values to fall off with increasing magnetic field may be due to some error involved in the timing of the measurement.

The initial transverse speed required by an electron on leaving the diode to undergo this mirror effect may be the result of multiple small angle Coulumb collisions in the anode plasma or simply be due to electrons obtaining large radial velocities during acceleration in the REB diode.

The greatest variation in beam current with magnetic field happened at the lower field values, however, there are no experimental points between B = 0 and B = 0.065T as the magnetic field trigger gap would not fire for charging voltages less than 500V.

The different beam current values at different magnetic field settings will have resulted in a different degree of loading of the cavity at each field setting. However, even the largest beam current values were thought to produce little perturbation of the natural modes of the cavity.

6.12 Summary of Chapter Six

The principal results of this chapter illustrate that injection of the REB into the drift tube resulted in the emission of microwave radiation at specific settings of external magnetic field. This radiation, detected at both X-band and Ka-band frequencies, occurred at power levels in excess of those one would expect from magneto-bremsstrahlung. Experiments with the Marx bank voltage set at 350 kV produced peak radiation power levels estimated to be approximately 10^5 W in the X-band region.

This self-excited radiation is thought to be due to an instability between the electron beam cyclotron frequency (or its harmonics) and the eigen frequencies of the cavity in which the REB drifted. An increase in the length of the drift tube resulted in the observation of microwave power at field settings where previously no emission was evident.

CHAPTER SEVEN CONCLUSIONS

7.1 Introduction

The increasing international interest in microwave radiation production from gyro-resonance type devices for applications such as plasma heating[???], plasma diagnostics, communications and high frequency radar applications (for both civil and military purposes) was one of the primary motivations for carrying out the work described in this thesis.

The REB diode, necessary for the production of the high current electron beam from which the r.f. energy was supplied, provided an additional field of study of strong interest to the scientific community, diode physics being of particular interest to the inertial confinement fusion (ICF) industry.

7.2 Summary

Chapter One of this thesis describes the sense in which the phrase "high-current" beam is being used here and describes briefly the historical development of pulsed power beam diodes. The dynamics of beam transport and focussing, important considerations for any REB application, are also discussed. A review of previous research pertinent to the interactions of such beams with external magnetic fields to produce microwave radiation is discussed. Although much is made in Chapter One of the merits of ECM devices at microwave frequencies higher than measured in this work this discussion is felt justified in

view of the initial hopes for the peak obtained values of the externally applied magnetic field.

Chapters Two and Three describe the overall experimental layout. Chapter Two describes the Marx bank arrangement which produced the high diode voltage necessary for the field-emission current. In addition, the anode-cathode geometry is described and the design considerations in producing a high current, hollow profile beam mentioned. The electron beam drift cavity, including transmission element, electron current collector and vacuum system are also described in this chapter.

The trigger circuitry for the Marx bank and the successful arrangement of the desired timing between the Marx and magnetic field banks, allowing the electron beam to be injected into varying values of magnetic field are also discussed in Chapter Two.

Chapter Three describes, in detail, the design considerations and construction of the pulsed magnetic field coil and energising circuitry. The practical limitations for the upper limits to the available magnitude of the magnetic field, over a sufficiently large volume, are explained. The limiting value of the magnetic field and the resulting limit of the observed microwave frequencies would indicate, at least with respect to ECRH heating of fusion plasmas, that this work can be considered to be only a beginning. Equations (3.10a) and (3.10b) were used to generate de Klerk's [75] damping function. To the author's knowledge, equation (3.10b) represents a first reported correction to the Montgomery[54] relation for d>1.

Chapter Four is devoted to the design and construction of the many diagnostics employed in making the measurements presented in Chapters Five and Six.

Chapter Five includes the results of the preliminary investigations of the REB diode behaviour with the transmitted electron current being injected into the evacuated drift tube in the absence of any externally applied magnetic field. For these experiments the fraction of the diode current which propagated through the anode mesh and into the drift tube was collected on a laminar stainless steel disc situated behind the anode, this collector being grounded and providing a return current path which facilitated measurement of the drift tube current. The drift tube current signal direction, obtained from one of the calibrated Rogowski loops discussed in Chapter Four, showed that the signal was indeed due to electron current.

The small percentage ($\leq 5\%$) of diode current converted to drift tube current was believed to have been limited by non-geometrical capture effects by the anode plasma as purely geometrical considerations gave a calculated value of the mesh transmission factor of 0.35 and impingement of electrons on the anode flange was thought to be too small to account for the discrepancy between the calculated and experimentally observed values.

The observed values of drift tube current and diode voltage coupled with equations (5.9) through to (5.11) would indicate that radial space-charge expansion of the hollow beam was

absent, a result borne out by the profile of the slight damage pattern evident on the laminar beam collector.

Firing of the field-emission diode at varying initial A-K gap settings illustrated some of the features familiar from the work of others on pulsed power sources. The collapse of the diode impedance as the cathode flare plasma diffused into the vacuum diode, so reducing the effective anode cathode separation, was apparent from the temporal changes in the diode voltage and diode current. The impedance collapse finally resulted in electrical shorting of the high current diode. The time required for gap closure was seen to be longer with increasing initial A-K gap setting and the values involved indicated a plasma expansion velocity of approximately 3 cm/ μs.

Firing of the Marx at different initial gap settings illustrated the existence of initial gap settings where breakdown was unreliable, for example where the diode failed to breakdown at all, or where breakdown occurred in some undesirable fashion. These observations led to the selection of a suitable operating gap setting for the beam current-magnetic field interaction experiments (Chapter Six), the choice of operating condition being a compromise between reliable diode operation and a suitably long diode voltage pulse width.

A brief attempt at increasing the gap closure time for a given initial gap setting by trying to leak magnetic flux

from the solenoidal coil into the diode region failed, presumably due to the limited magnitude of the magnetic field present in the A-K gap. The presence of the conducting anode flange and the pulsed nature of the solenoidal current source coupled with the limited proximity of the anode flange to the field coil was believed to have limited the magnitude of the magnetic field present in the diode gap.

The A-K gap was finally set for a distance of three centimetres for the experiments on microwave production. This setting appeared to have good shot to shot reproducibility with only fine detail on the diode voltage profiles varying from one shot to the next. During the course of the experiments two alterations regarding the diode condition occurred. The first alteration was a gradual and uncontrollable change in the cathode condition. The stainless steel emitter showed a slight amount of wear over a long period of time due to the high currents originating from its surface, an effect which was apparent from visual inspection of the emitter.

The second alteration was more obvious from the diode voltage diagnostic trace, and was the result of removing the field-grading rings placed between the perspex insulators inserted between the anode and cathode flanges (Chapter Two). The result of this more abrupt change in conditions was to give the voltage pulse a longer rise-time and produced a flatter peak. This interesting change in conditions means the temporal impedance profile during the

microwave radiation production experiments was different from that during the impedance collapse experiments of Chapter Five. The resulting diode voltage profile was still of suitably long duration to be of interest in microwave production experiments and, in fact, was even more reproducible in behaviour than when the field-grading rings were present.

In Chapter Six the work involving the interaction of the electron beam with the pulsed external magnetic field is reported. The initial important result is the presence of resonant values of applied magnetic field for which high levels of output microwave radiation were observed. At specific settings of the external magnetic field the emitted radiation power is seen to be five orders of magnitude above that which would be expected from the calculated value of the incoherent magneto-bremstrahling, this calculation being made possible by a measurement of the total collected e-beam charge on the drift tube cavity. The calculation lends credence to the belief that the emission was due to a coherent process, in fact, a resonant interaction between one of the beam's electron cyclotron modes and some natural resonant frequency of the "cavity" in which the beam drifted. The proposed cavity in this model is thought to be formed by the stainless steel drift tube, the anode mesh and the partially transmitting output window at the end of the evacuated glass tube.

It can be seen from Fig (6.5) that the regions of high output radiation level are not sharp but lie in "windows" of magnetic field setting. The factors contributing to the window width are complicated due to the spatial and temporal variations in both the radial and axial components of the solenoidal field as well as the complicated cavity resonator structure and the time varying diode voltage and hence the time-varying electron energy.

Despite the appearance of some variation in microwave crystal detector output with fixed values of Marx setting and magnetic field setting the values of magnetic field at which the microwave radiation output is below the noise-level were repeatedly seen to be the same for the fixed stainless steel collector length. However, an extension of the collector length resulted in the appearance of a larger signal at the lower edge of one of the window regions where previously no signal had been observed. The extension of the collector length would alter the drift cavity configuration and, of course, change the cavity's natural frequencies. This result was an indication, therefore, that the emission was dependent upon resonant frequencies associated with the drift cavity.

Even with the Marx bank voltage held constant it was found that it was impossible to study the variation in microwave output with only variations in the external magnetic field setting. Simultaneous observations of the

electron beam current along with the microwave radiation output against changing magnetic field setting illustrated that, along with the variation in radiation output with field, the electron beam current was decreasing with increasing magnetic field magnitude. This change of current with magnetic field is particularly evident over the variation in zero-field to relatively small field values ($\lesssim 0.15$T) and the possibility of magnetic mirroring of the electrons was mentioned to account for this phenomena.

A brief investigation of the radiation output was made with a Ka-band crystal detector and the appearance of appreciable amounts of radiation power (although less than that seen in the X-band detector) indicated that interactions at harmonics of the fundamental electron gyro-frequency were present. These observations were strengthened with the appearance of signals well above the noise level at magnetic field values whose electron cyclotron frequencies would lie below the X-band cut-off frequency so indicating that the interaction is with at least the first harmonic of the fundamental gyro-frequency.

After the removal of the field-grading rings the new impedance collapse behaviour of the REB with the gap setting at 3 cm was observed for various values of Marx voltage setting. The increase in Marx voltage setting produced little alteration in diode voltage, however,

this increased Marx voltage setting resulted in the appearance of higher electron currents which allowed a brief investigation of microwave output power at larger input beam powers. These experiments showed a clear increase in radiation power with pulsed beam power.

A simple experiment with microwave polarising plates (X-band) showed that the radiation field appeared to be of equal intensity in two mutually orthogonal directions perpendicular to the microwave propagation direction.

7.3 Suggestions for Future Work

The work reported in this thesis leads to suggestions for alterations in the experimental design in order to attempt to alter particular parameters and to make measurements of parameters hitherto not measured.

The duration of the electron beam current pulse and the extent of the transmission from the diode region to the drift region could be affected by a change of anode design by replacing the mesh insert by a "foilless" type diode. The absence of the conducting anode would presumably allow higher values of magnetic field from the pulsed solenoid to diffuse into the emitter region, thus tying the electrons to the magnetic flux lines earlier so preventing radial diffusion of the electrons which, in turn, would effectively decrease the flare plasma velocity. The increased diode magnetic field would also allow greater control of the diode-cavity

mirror ratio, thus giving the operator greater control of transverse electron energy and hence the "free" energy available for radiation. Clearly, a foilless diode would also reduce the non-geometrical capture effects which have previously limited the anode current transmission factor.

The use of anode grids of differing mesh sizes would also provide differing transmission factors thus altering the overall efficiency of the device.

As stated in 7.2, cyclotron maser emission at the frequencies reported here is of limited interest to the CTR industry. An obviously desirable requirement for more relevant work in this area would be the application of larger magnetic fields for the REB. To achieve this with a pulsed solenoid would require the use of a greater energy storage capacitor bank, or, alternatively, the existing bank with a reduced size drift cavity and solenoid diameter.

As well as employing larger magnetic fields, it would be of interest to have more accurate information on the emitted radiation frequencies and their frequency and power dependence on the external magnetic field.

A means of measuring the output frequency to a higher accuracy than simply the r.f. waveguide band designation could be provided by a reflection grating spectrometer, a technique employed by other workers on devices of a similar nature[74]. The spectral power density of the output radiation could be investigated by the use of pass band filters and microwave diodes for which the calibrations

with frequency are known.

Appendix 1

The following is a list of the resistors and capacitors used as integrators to accompany the Rogowski coils.

The measurements of resistance were made with a digital multimeter. The errors in these measurements are 0.1% plus 1 on the last significant digit.

The corresponding capacitance measurements were made with a digital capacitance meter. The accuracy uncertainty on all ranges employed was 0.5% plus 1 on the last significant digit.

Resistance(R) / kΩ	Capacitance (C) / nF	RC / ms
101.6	105.3	10.70 ± .6%
104.9	105.6	11.08 ± .6%
22.1	4.733	0.1046 ± .8%
23.3	4.693	0.1093 ± .7%
9.19	105.3	0.968 ± .6%

Appendix 2

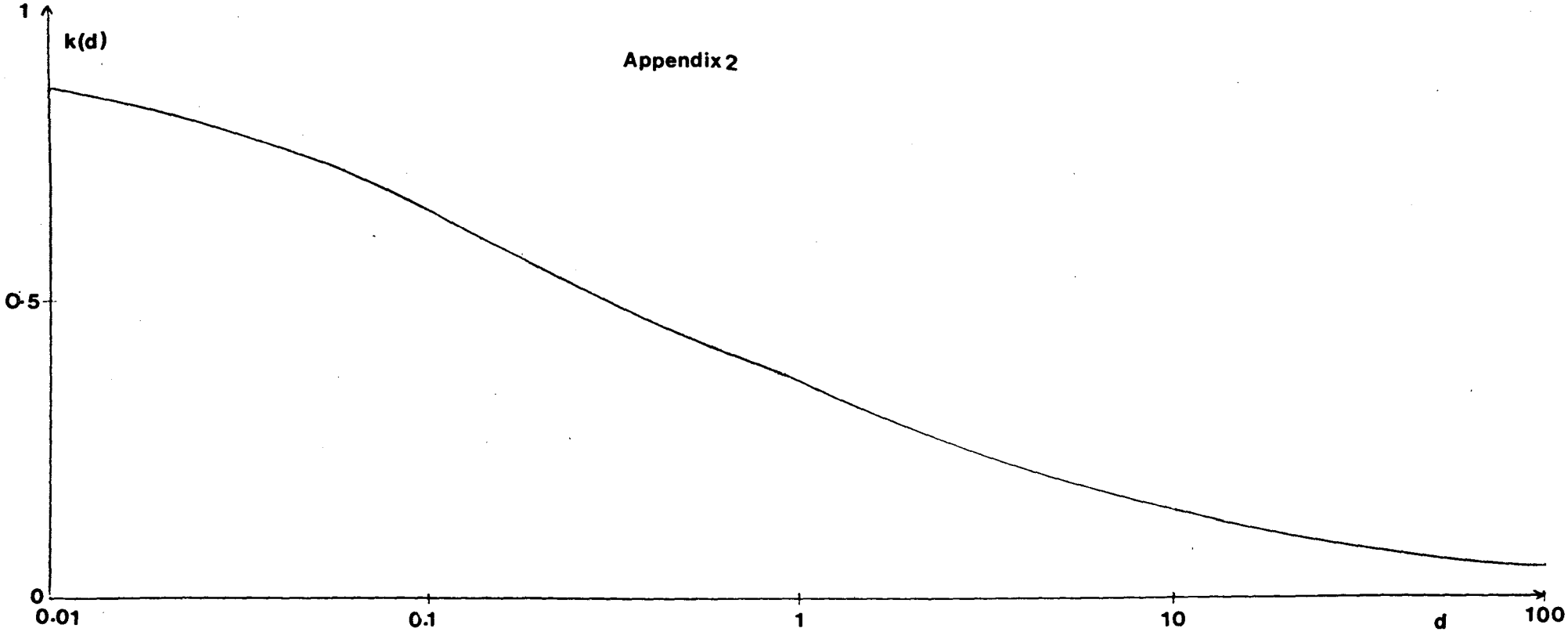

k(d) plotted as a function of d and calculated from Eqn(3·10), after de Klerk[75].

Appendix 3

ENVELOPE EQUATION FOR HOLLOW BEAMS

At the end of section (5.5.2.) it was stated that Lawson's beam envelope equation for solid non-neutral electron streams whose particle density was constant up to the beam radius and zero for greater radii was identical to the relation for hollow beams. This will now be shown. The analysis will be carried out using the same restrictive assumptions employed by Lawson [1, 2, 76]

The postulated beam is assigned the following properties:

(1) All electrons have the same momentum, $\gamma m_0 c$,

(2) The beam is completely non-neutral, i.e. f=o,

(3) The transverse velocity component of any electron is small in comparison with its longitudinal velocity component, (i.e. the motion is assumed to be 'paraxial'),

(4) The beam is cylindrically symmetric and of infinite length,

(5) No collective beam oscillations are present,

(6) The beam particle density, n_e, has the following form;

$$n_e = \begin{cases} 0, & 0 \leq r < a \\ n_e, & a \leq r \leq b \\ 0, & r > b \end{cases} \qquad \text{(A3.1)}$$

Where

$$n_e = \frac{N}{\pi (b^2 - a^2)} \qquad \text{(A3.2)}$$

To calculate the self electric field of the beam we can use Gauss' law.

Hence,

$$\int_S E_r dS = \frac{e}{\varepsilon_o}\int_\tau n_e \, d\tau \qquad \text{(A3.3)}$$

$$\Rightarrow \quad E_r = \frac{en\,(r^2-a^2)}{2\quad r} = \frac{eN\,(r^2-a^2)}{2\quad (b^2-a^2)r} \qquad \text{(A3.4)}$$

Hence the force, due to the electric field, experienced by an electron within the annular beam is given by,

$$F_E = \frac{e^2 N\,(r^2-a^2)}{2\pi\varepsilon_o(b^2-a^2)r} \qquad \text{(A3.5)}$$

To evaluate the self-magnetic field we can employ Ampere's Law. Hence,

$$\oint B_\theta dl = \frac{1}{\varepsilon_o c^2}\int_S j\, dS \qquad \text{(A3.6)}$$

Where j is the beam current density,

$$\therefore \quad B_\theta = \frac{j\,(r^2-a^2)}{2\varepsilon_o c^2 r} \qquad \text{(A3.7)}$$

However,

$$j = \frac{I}{\pi\,(b^2-a^2)} = \frac{Ne\beta\, c}{\pi\,(b^2-a^2)} \qquad \text{(A3.8)}$$

Therefore,

$$B_\theta = \frac{Ne\,\beta\, c\,(r^2-a^2)}{2\pi\varepsilon_o c^2\ (b^2-a^2)r} \qquad \text{(A3.9)}$$

Hence the force, due to the magnetic field, experienced by an electron moving with speed βc is given by

$$F_M = \frac{Ne^2\beta^2\ (r^2-a^2)}{2\pi\varepsilon_o(b^2-a^2)r} \qquad \text{(A3.10)}$$

With due respect to the direction of the magnetic and electric forces the equation of motion of a beam electron is given by

$$\gamma m_o \frac{d^2r}{dt^2} = \frac{Ne^2 (1-\beta^2)(r^2-a^2)}{2\pi\varepsilon_o (b^2-a^2)} \qquad \text{(A3.11)}$$

However, $1 - \beta^2 = \frac{1}{\gamma^2}$ and $\frac{d^2r}{dt^2} = \beta^2 c^2 \frac{d^2r}{dz^2}$

$$\Rightarrow \quad r\frac{d^2r}{dz^2} = \frac{2\nu}{\gamma^3\beta^2} \times \left[\frac{r^2-a^2}{b^2-a^2}\right] \qquad \text{(A3.12)}$$

It can be seen that in the limit of $a \rightarrow o$ this equation is identical with Lawson's.

Evaluating $\left[r \frac{d^2r}{dz^2} \right]_{r=b}$ one can immediately see that

$$\left[r \frac{d^2r}{dz^2} \right]_{r=b} = K = \frac{2\nu}{\gamma^3\beta^2}$$ which is just as

eqn.(1.2)

Appendix 4

The frequencies of the resonant TE^{o}_{lmn} modes of a cylindrical cavity of diameter D and length L are given by

$$\frac{fD}{c} = \left[\left(\frac{x_{l,m}}{\pi}\right)^2 + \left(\frac{nD}{2L}\right)^2\right]^{\frac{1}{2}} \qquad (A4.1)$$

where n is given by the number of half period variations of the radial component of the electric field along the length of the cavity. The values of $x_{l,m}$ are given by the m^{th} zero's of the l^{th} order Bessel function i.e. $J'_l(x_m) = o$. The spatial structure of the TE^{o}_{lmn} modes is revealed by the fact that l represents the number of full period variations of E_r around a co-ordinate phase angle of 2π and m represents the number of half period variations of the azimuthal electric field component across the radius of the cavity.

Table (A4.1) gives a comparison between the electron cyclotron frequencies at which strong microwave emission was observed and the cavity cut-off frequencies given by $f_{co} = \frac{x_{l,m}c}{\pi D}$ for some values of l and m.

Combining equations (6.3) and (6.4) we can see that, for a given TE^{o}_{lmn} mode, a differential change, δl_c, in the cavity length would produce a differential change, $\delta\omega$, in the resonant frequency given by,

$$\delta\omega = \frac{-(nc\pi)^2 \delta l_c}{\omega l_c^3} \qquad (A4.2)$$

indicating that an increase in l_c would produce a decrease in ω. This is in accord with the observation of resonance at a lower electron cyclotron frequency with the extended collector length (section 6.4.1).

TE mode	f_{co}(GHz)	"measured" frequency (GHz)
02	6.91	
61	7.38	
32	7.89	
13	8.40	
71	8.44	
42	9.13	8.7 ± 1
81	9.50	
23	9.81	9.7 ± .5
03	10.02	10.2 ± .5

TABLE (A4.1)

Comparison of TE^{o}_{1m} mode cut-off frequencies (.97 cm diameter cavity) with electron cyclotron frequencies, inferred from measurement of diode voltage and external magnetic field.

It is stressed that the change in collector length will not necessarily equal the change in cavity length as the exact longitudinal extent of the cavity is complicated by the considerations mentioned in chapter six. However, it is reasonable to assume that an increase in the collector length will produce an increase in the length of the cavity.

In addition to altering the natural frequencies of the cavity a change in the axial wave number may alter the frequency at which self-excited emission occurs through the condition, discussed in chapter one, that ECM gain will occur for frequencies just above the Doppler shifted cyclotron frequency or its harmonics.

It is clear from equation (6.5) that for a given electron axial velocity a change in the axial wave number will produce a change in the Doppler snift term.

REFERENCES

(1) J.D. Lawson, J. Electron. Control, Vol. 3, pp 587-94 (1957).

(2) J.D. Lawson, J. Electron. Control, Vol. 5, pp 146-51 (1958).

(3) J.D. Lawson, J. Nucl. Engergy C, Vol. 1, pp 31-35 (1959).

(4) G.J. Budker, Cern Symposium (1956). Reproduced in 'Collective Methods of Acceleration', Ed. N. Rostoker, and M. Reiser (Harwood Acad. Publishers (1979).

(5) E.R. Harrison, J. Electron, Vol. 4, p 193 (1958).

(6) A.J. Toepfer, Laser-Plasma Interactions, Proceedings. 20th S.U.S.S.P., Ed. R.S. Cairns and J.J. Sanderson, pp 607-60 (1979).

(7) G.A. Mesyats, Sov-Phys-Tech. Phys, Vol. 19, pp 948-51 (1975).

(8) R.K. Parker et al, J. Appl Phys, Vol 45, pp 2463-79 (1974).

(9) L.P. Bradley and G.W. Kuswa, Phys Rev Lett., Vol 29, pp 1441-45 (1972).

(10) W.T. Link, I.E.E.E. Trans. Nucl. Sci., Vol. 14, pp 777-81 (1967).

(11) H. Alfvén, Phys. Rev., Vol. 55, pp 425-29 (1939).

(12) H. Alfvén, Ark. Fys., Vol. 20, pp 389-92 (1961).

(13) W.H. Bennett, Phys. Rev., Vol. 45, pp 890-7 (1934).

(14) R.C. Davidson, The Theory of Non-Neutral Plasmas, (W.A. Benjamin, Reading Mass.) (1974).

(15) D.A. Hammer and N. Rostoker, Phys. Fluids, Vol. 13, p 1831 (1970).

(16) P.L. Auer, Phys. Fluids, Vol. 17, pp 148-55 (1974).

(17) G. Benford and D. Book, Adv. Plasma Phys., Vol. 4, p 125 (1971).

(18) Proc. of the 4th International Topical Conference on High Power Electron and Ion Beam Research and Technology, Palaiseau (1981).

(19) J.A. Nation, Appl. Phys. Lett., Vol. 17, pp 491-94 (1970).

(20) M. Friedman and M. Herndon, Phys. Rev. Lett., Vol. 29, pp 55-58 (1972).

(21) Y. Carmel and J.A. Nation, J. Appl. Phys., Vol. 44, pp 5268-74 (1973).

(22) R.M. Phillips, I.E.E.E. Trans Electron Devices, Vol. 7, p 231 (1960).

(23) M. Friedman et al, Phys. Rev. Lett, Vol. 31, pp 752-55 (1973).

(24) M. Friedman and M. Herndon, Phys. Fluids., Vol. 16, pp 1982-95 (1973).

(25) V.L. Granatstein et al, J. Appl. Phys., Vol 46, pp 2021-28 (1975).

(26) V.L. Granatstein et al, J. Appl. Phys., Vol. 46, pp 3800-5 (1975).

(27) V.L. Granatstein et al, I.E.E.E. Trans. Microwave Theory and Tech., Vol. MTT-22, pp 1000-5 (1974).

(28) V.L. Granatstein et al, Plasma Phys., Vol. 17, pp 23-28 (1975).

(29) R.Q. Twiss, Aust. J. Phys., Vol. 11, pp 564-79 (1958).

(30) J. Schneider, Phys. Rev. Letters, Vol. 2, pp 504-5 (1959).

(31) A.V. Gaponov, Izv. VUZ, Radiofizika, Vol. 2, pp 450-462 (1959).

(32) J.L. Seftor et al, I.E.E.E. J. Quantum Electronics, Vol. QE-15, pp 848-53 (1979).

(33) V.A. Flyagin et al, I.E.E.E. Trans Microwave Theory and Tech., Vol. MTT-25, pp 514-21 (1977).

(34) T.J.M. Boyd and J.J. Sanderson, Plasma Dynamics, Nelson (London) (1969).

(35) A.F. Harvey, Microwave Engineering, Academic Press, New York (1963).

(36) P. Sprangle et al, Journal de Physique, Vol. 38 (6), pp 135-52 (1977).

(37) K.K. Chow and R.H. Pantell, Proc. I.E.E.E., Vol. 48, pp 1865-70 (1960).

(38) I.B. Bott, Phys. Letters, Vol. 14, pp 293-4 (1965).

(39) I.B. Bott, Proc. I.E.E.E., Vol. 52, pp 330-2 (1964).

(40) J.L. Hirshfield and J.M. Wachtel, Phys. Rev. Letters, Vol. 12, pp 533-6 (1964).

(41) D.V. Kisel' et al, Radio Eng. Electron Phys., Vol. 19, pp 781-88 (1974).

(42) N.I. Zaytsev et al, Radio Eng. Electron Phys., Vol. 19, pp 103-7 (1974).

(43) V.L. Granatstein et al, Infrared and Millimeter Waves, Vol. 5, pp 267-303, Academic Press (1982).

(44) G. Mourier, 9th European Microwave Conference, Brighton (1979).

(45) V.L. Granatstein et al, 4th International Conference on Infrared and Millimeter Waves and their applications, Miami (1979), pp 122-24 (I.E.E.E. Cat. No. 79 CH 1384-7 MTT).

(46) P. Sprangle and R.A. Smith, J. Appl. Phys. Vol. 51, pp 3001-7, (1980).

(47) J.L. Hirshfield, Infrared and Millimeter Waves, Vol. 1, Ed. K.J. Button, Academic Press (1979).

(48) A.A. Andronov et al, Collection of Papers on the E.C.M. (Gyrotron) Vol. 1, pp 1-21, Ed. S.Y. Ahu, V.L. Granatstein and J.L. Hirshfield, N.R.L. Memorandum Report 3397 (1980).

(49) J.A. Nation, Particle Accelerators, Vol. 10, pp 1-30 (1979).

(50) S.E.R.C. Rutherford Laboratory, Central Laser Facility Report (1979).

(51) R.S. Symons and H.R. Jory et al, Adv. in Electronics and Electron Phys., Vol. 55, pp 2-71, Ed. L. Martin and C. Martin (1981).

(52) G. Bekefi et al, Phys. Rev., Vol 122, pp 1037-42, (1961).

(53) H. Jory et al, Proc. 2nd Joint Grenoble-Varenna Int. Symposium (EUR-7424-EN), pp 269-82 (1980).

(54) D.B. Montgomery, Rep. Prog. Phys., Vol. 26, pp 69-104 (1963).

(55) F.E. Terman, Radio Engineers Handbook, (New York: McGraw-Hill) (1943).

(56) Plasma Diagnostic Techniques, Ed. R.H. Huddlestone and S.L.Leonard, Acad. Press (N.Y.) (1965).

(57) H.E. Frank et al, J. Phys. D: Appl. Phys.,Vol 15, pp 41-49 (1982).

(58) W. Rogowski and W. Steinhaus, Arch Elecktrotech, Vol. 1, p141 (1912).

(59) M.S. Di Capua and D.G. Pellinen, Proc. Int. School of Plasma Physics Course on Diagnostics for Fusion Experiments, Varenna, (1979), (Pergamon, Oxford and N.Y.).

(60) D.G. Pellinen et al, Rev. Sci. Inst., Vol. 51, pp 1535-40 (1980).

(61) D. Pellinen, Rev. Sci. Inst., Vol. 43, pp 1654-58 (1972).

(62) F. O'Neill et al, Proc. Int. Topical Conference on High Power Electron and Ion Beam Technology, Palaiseau (1981) pp 229-36.

(63) M. Friedman and M. Ury, Rev. Sci. Inst., Vol. 43, pp 1659-61, (1972).

(64) Y. Carmel and J. Nation, Phys. Rev. Lett., Vol. 31, pp 286-289 (1973).

(65) D.MacDougall, Final Year Report, Strathclyde University (1982).

(66) L.S. Levine and I.M. Vitkovitsky, I.E.E.E. Trans. Nucl. Sci., Vol. 18, pp 255-64 (1971).

(67) G. Yonas and A.J. Toepfer, Gaseous Electronics, Vol. 1, Ed. M.N. Hirsh and H.J. Oskam, Academic Press ISBN, 0-12-349701-9 (1978).

(68) R.B. Miller, An Introduction to the Physics of Intense Charged Particle Beams, Plenum: N.Y. and London, (1982).

(69) N.S. Ginzburg et al, Sov. Phys. Tech. Phys., Vol. 24, pp 218-22 (1979).

(70) J.A. Nation, Rev. Sci. Inst., Vol. 41, pp 1097-8 (1970).

(71) V.L. Granatstein et al, Proc. Int. Topical Conf. Electron Beam Research and Technology (SAND 76-5-22), pp 401-23 (1975).

(72) V.L. Granatstein et al, Proc. 2nd Int. Topical Conf. on Electron and Ion Beam Research (Cornell Uni), pp 675-689 (1977).

(73) G. Bekefi, Radiation Processes in Plasmas, Wiley, New York (1966).

(74) J.A. Pasour and S.P. Schlesinger, Rev. Sci. Inst., Vol. 48, pp 1355-56 (1977).

(75) D de Klerk, The Generation of High Electromagnetic Fields, Newport Instruments Ltd. (1966).

(76) J.D. Lawson, Particle Accelerators, Vol. 1, pp 41-46 (1970).

(77) A.C. Riviere, Plasma Physics and Nuclear Fusion Research, Ed. R.D. Gill, Acad. Press (London) 1980.

(78) A.D.R. Phelps and T. Garvey, paper submitted to 10th Annual IOP Plasma Physics Conf., Bangor (1983).